AN ABSTRACT OF THE THESIS OF

Hyo-Jin Kim for the degree of Doctor of Philosophy in Chemistry presented on February 20. 1989.

Title: Fundamental Studies of a Gas-jet Enhanced Sputtering System and its Applications

Redacted for Privacy

Abstract approved: _____

Edward H. Piepmeier

The use of gas jets in a sputtering cell makes this direct sampling method practical for atomic absorption and mass spectrometry determinations. With a commercial six-jet sputtering source, the Atomsource (Analyte Corp., Grants Pass, Oregon), that directly atomizes solid samples for conventional atomic absorption spectrophotometers, the sample loss rate for a Cu sample is 400 μg/min with a 0.2 L/min gas flow rate, and 170 μg/min with no gas flow. With a single-jet glow discharge source, the gas jet increases the absorbance by a factor of 40. Studies of the electrical and spectral characteristics of this six-jet Atomsource and a similar single-jet glow discharge source have been made to help determine the mechanisms responsible for the increased absorbance and the increased sampling rate. A scanning electron microscope is used to investigate the effect of experimental parameters such as current density,

sputter time, gas flow rate, and cathode base material on the microstructure of the cathode surface.

The Atomsource is interfaced to the mass spectrometer of a VG PlasmaQuad ICP-MS, replacing the ICP. The pressure, current, anode voltage, sampling distance, and sampling cone hole size are optimized to obtain improved performance for analytical applications. With an optimized source, it is possible to determine elements at low concentrations that would be difficult to determine with ICP-MS.

Three zirconium standards, one zircaloy standard, and one zircaloy sample were analyzed and the presence of 15 elements was determined. The average relative precision of measurement for 10 elements was better than 4 percent. In a multielement analysis the detection limits for 13 elements were lower than 0.5 ppm, while single element determination improved the detection limits by an order of magnitude. Concentrations determined with an internal stsandard were in agreement within 10 % of the certified values for most of the elements in the Zircaloy sample.

FUNDAMENTAL STUDIES OF A GAS-JET ENHANCED SPUTTERING SYSTEM AND ITS APPLICATIONS

by

Hyo-Jin Kim

A THESIS

submitted to

Oregon State University

in partial fulfillment of

the requirements for the

degree of

Doctor of Philosophy

Completed February 20, 1989

Commencement June, 1989

APPROVED:

Redacted for Privacy

Professor of Chemistry in Charge of Major

Redacted for Privacy

Chairman of Department of Chemistry

Redacted for Privacy

Dean of the Graduate School

Date thesis is presented February 20, 1989

Acknowledgments

This thesis is dedicated to my family, MyungHee and Jina, and to my parents, YongPom Kim, and SangNam Lee.

I would like to thank Dr. Piepmeier for his support and gudidance during my studies at OSU.

I would acknowledge the contributions of a variety of individuals and organizations.

TABLE OF CONTENTS

LISTS OF FIGURES

Figures Page

Figures

Figures Page

Figures

Figures

Figures

Page

Figures Page

Figures Page

LIST OF TABLES

FUNDAMENTAL STUDIES OF A GAS-JET ENHANCED SPUTTERING SYSTEM AND ITS APPLICATIONS

I. INTRODUCTION

In recent years, the number of applications for analytical laboratory glow discharge devices have been increasing substantially. This is not to say that the glow discharge device represents a new analytical technology. The first observations of the electroluminescence phenomena in low pressure gases date to the early 19th century, based on the basic studies of J. W. Hittorf (1824-1914), W. Crookes (1832-1919) and H. Geissler (1814-1879) [1]. In the early 20th century, J. S. E. Townsend (1868-1957) and F. Paschen (1865-1947) developed the modern glow discharge for a variety of applications [2].

Even though these scientists are not familiar names to the general public, their work has lead to many improvements currently in use in daily life, for example, the rare-gas filled Geissler-type lamp (including the common neon light) for lighting and advertising [3]. The laser, which has had such a significant impact on modern physics, has largely been the result of applied uses of these types of discharges.

At the start of this century, Paschen [4] established an important milestone in the evolution of low pressure discharges by pioneering in the use of the hollow-cathode discharge, which was further developed by H. Schuler and H. Gollnow [5]. Subsequently, the glow discharge has been extensively developed in an almost countless number of interrelated versions of both flat and hollow-cylinder cathode types.

In 1967, W. Grimm [6] developed a unique glow discharge for solid sample analysis, leading to wide applications of the low-pressure discharge in mineralogy and metallurgy. At the same time the hollow-cathode discharge, based on the original designs, has been developed for a radiation source. Both the glow discharge and the hollow-cathode discharge sources have established an important position in analytical spectroscopy and a variety of other applications.

Recently, a newly developed jet-enhanced sputtering atomizer, called the Atomsource (Analyte Corporation, Grants Pass, Oregon), was introduced and has shown good analytical performance [7,8]. This Atomsource uses six high-velocity gas jets that are introduced at equally spaced intervals around the circumference of the exposed sample. The jets are pointed in directions that cause them to directly impact the surface, not only changing the visual and electrical characteristics of the discharge, but also increasing the amount of material atomized, particularly where the jets impact the surface. The centering action of the jets and the high velocity of the gas flow cause the sputtered atoms to move rapidly into the center of the cell, away from the sample surface and the walls of the

chamber. This reduces the loss of atoms resulting from deposition on the walls of the chamber and redeposition back onto the sample.

The main goal of the research documented in this thesis has been to study this unique jet-enhanced sputtering method and to investigate its fundamental characteristics. This thesis also describes the developments of the instrumentation as well as applications of the jet-enhanced sputtering system to various analytical techniques, including atomic absorption, emission, and mass spectrometry.

II. HISTORICAL

1. Fundamental Glow Discharge Process Studies

A typical glow discharge is generally obtained by applying a DC potential of several hundred volts between two planar electrodes in an inert gas pressurized to around 0.1 to 10.0 torr (13 to 1333 Pa). A few hundred volts applied across the electrodes causes the breakdown of the gas and formation of the ions, electrons, and other species that make the glow discharge useful in analytical chemistry.

When two electrodes are enclosed in a low pressure chamber filled with a rare gas, no current flow can be observed if the applied voltage is too low to induce ionization. When the applied voltage is very slowly raised, sensitive instruments may be used to detect current, initially random current pulses of less than 10^{-16} A. Figure II.1 shows the typical voltage-current relationships within a

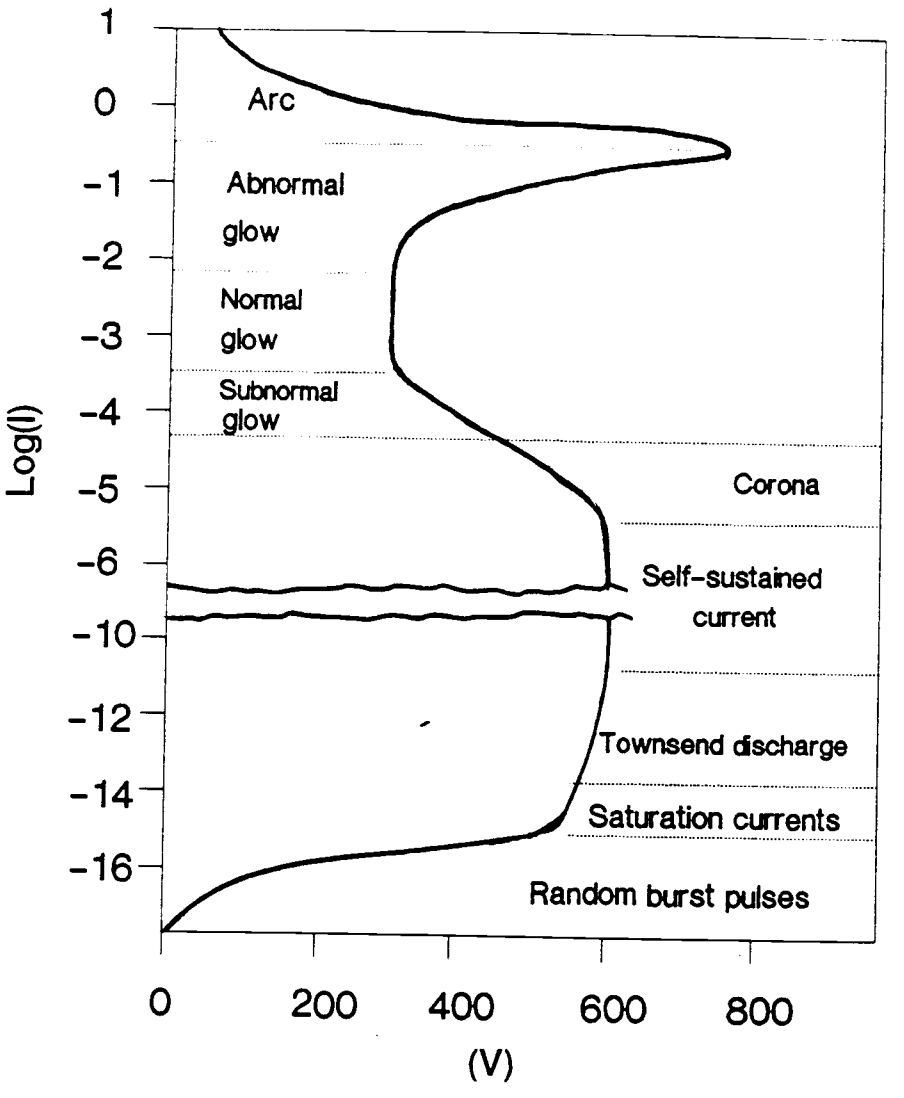

Figure II.1 Typical voltage-current relations within a gaseous gap (ref 9).

gaseous gap [9]. Current increases with voltage until reaching the plateau known as the saturation current, corresponding to "B" of the characteristic curve. Increasing the voltage across the gap will not initially affect the current, but beyond a certain point the current will again begin to increase. The area of increase, called the Townsend discharge, is exponential. The Townsend discharge, nonluminous in nature and characterized by very low current loads, is not a self-sustaining discharge and requires external sources (i.e., X-rays or UV light) to produce electrons. The Townsend discharge has been applied for analytical use in mass spectrometry [10].

Under the conditions described above, further voltage increases lead to a sharp increase in current. This is followed by a collapse of the voltage across the gap, a phenomenon known as "breakdown", which is characterized by an increase in current of several orders of magnitude with almost no increase in voltage. If the current is allowed to increase further, by cutting down the series resistance of the outer circuit, the voltage across the discharge will begin to drop until it reaches a low level identified as the normal glow region. An exponential increase in current, known as the abnormal glow region, follows. It is this region in which most sputtering occurs, and which is the most important source of analytical applications (this region will be discussed in more detail later).

Finally, when the current is again allowed to increase, another transition occurs, resulting in a new form of discharge known as the arc discharge because of its extreme brightness.

The glow discharge is one form of plasma, a partially ionized gas

consisting of approximately equal concentrations of positive and negative charges, plus large numbers of neutral species. The conventional DC glow discharge is characterized by up to eight zones or regions which develop between the electrodes, depending upon the configuration of the discharge.

Figure II.2 [1] indicates the various regions between the cathode, on the left, and the anode, on the right, of a glow discharge. The names given to the dark and bright regions are, from cathode to anode: the Aston dark space; the cathode glow layers or sheaths; the cathode dark space, also called the Crookes (English) or Hittorf (German and Russian) dark space; the negative glow; the Faraday dark space; the positive column; the anode dark space; and the anode glow. The dark spaces, with the exception of the Aston dark space, are not entirely nonluminous, but the intensity of their radiation is much less than that of the bright regions.

The positively ionized atoms of the gas are attracted by the cathode, on which they collide to cause a secondary emission of electrons requiring maintenance of the discharge. The bombarding ion species are believed to be neutralized by a field-emitted electron just prior to impact with the cathode surface. The secondary electron yield for most metals is of the order of 0.1 [11] for incident Ar ions over the range of bombardment energies in the glow discharge (300-500 eV). Adjacent to the cathode surface, where most of the potential drop occurs, secondary electrons form a negative space charge region called the Aston dark space. Further from the cathode surface there is a region referred to as the cathode layer, in which the electric field becomes weaker and where electrons are

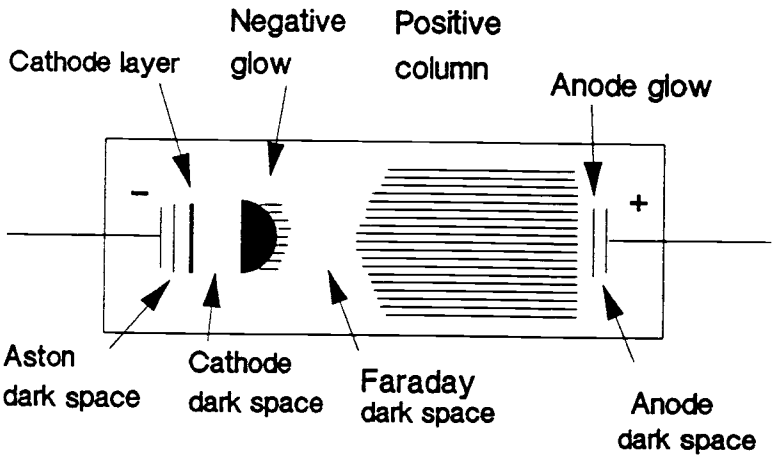

Figure II.2 Various regions between the cathode, on the left, and the anode, on the right, of a glow discharge (ref 1).

more efficient excitation and ionization agents, causing electron multipication and ionization of the discharge gas. In the cathode dark space the electric field becomes even weaker, and only those fast electrons that have not lost energy through inelastic collisions are able to ionize in this region. Ions accelerated across the cathode dark space collide with the cathode with sufficient energy to cause sputtering, or the release from the surface of atoms and clusters. Positive ions that are sputtered are forced back to the cathode surface by the electric field, but electrons that are released are accelerated across the dark space toward the main body of the discharge. There they begin to collide inelastically with gas atoms, producing a large number of positive ions and more electrons. A large net positive space charge is established throughout the cathode dark space, producing a large potential gradient and most of the discharge voltage drop.

Near the end of the cathode dark space, the current is carried by electrons in either of two groups: fast electrons, produced near the cathode surface, which have not suffered inelastic collisions in the cathode dark space; and slow electrons, those created in the cathode dark space which are less energetic due to inelastic collisions. Eventually, a negative glow region is reached in which the most intensely bright discharge occurs, with a color that is characteristic of the discharge gas. As the fast electrons penetrate into the negative glow, both ionization and excitation are produced as their energy is exhausted. Evidence for this exhaustion exists in the presence of the Faraday dark space, in which exciting collisions are minimal. However, electrons accelerated through the

Faraday dark space acquire enough energy to cause excitation and ionization in the next zone, called the positive column. The positive column, like the negative glow, is a glowing region with no net space charge and very little potential drop. It is a luminous region which easily molds itself in the shape of the containing tube. In the glow discharge the anode does not emit any particles and simply collects the electrons. In general, there is a negative space charge region near the anode, and slow electrons emerging from the positive column will enter the anode fall region, in which they are accelerated toward the anode. As these electrons gain sufficient energy to excite and ionize the gas in front of the anode, an anode dark space and an anode glow are formed. In practice, a glow discharge can exist without a positive column, a Faraday dark space, or even a negative glow, but it can never exist without a cathode dark space [12].

The cathode sample is atomized into the discharge by a process called sputtering [13]. Positive ions and fast neutrals collide with the cathode sample, penetrating a few atomic distances before losing their momentum through a three-dimensional billiard cascade of atomic lattice collisions, as illustrated in Figure II.3 [1]. When some of the atoms at the surface acquire sufficient energy through these collisions, most of the cathode sample is ejected as neutral atoms with a small percentage consisting of ions. Positive ions are returned to the surface due to the large electric field of the cathode dark space, but the neutral atoms diffuse into the negative glow region. This large region of sputtered neutral atoms results in the glow discharge so useful to analytical spectrometry. Solid

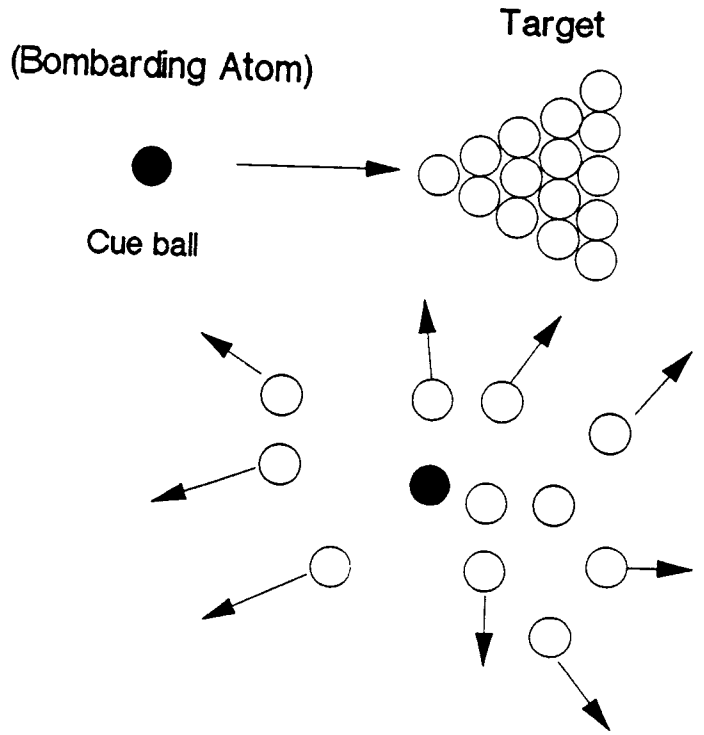

Figure II.3 A three-dimensional billiard cascade of atomic lattice collisions (ref 1).

samples are directly analyzed through excitation and ionization of sputtered atoms.

The first observations of metal deposits sputtered from the cathode of a glow discharge were reported as early as 1852 [14]. At that time, cathodic sputtering was considered an unwanted by-product since it caused erosion of the electrodes, resulting in undesirable deposits which blackened the glass walls and observation windows. However, this attitude has changed considerably as investigators in the fields of electrical engineering, material analysis, physics, and analytical chemistry have become interested in possible applications of glow discharge sputtering.

2. Glow Discharges Applications in Atomic Spectroscopy

2.1 Atomic Absorption Spectrometry

Although sputter atomization is the fundamental process in the glow discharge, the use of this device for atomic absorption spectrometry has not been developed substantially. Most glow discharge applications have used emission rather than absorption to detect the sputtered atoms, which is largely due to the availability of commercial cells and their simultaneous multielement capability advantages. Simultaneous multielement capability has just begun to be of significant importance to commercial atomic absorption spectrometers [15]. Although atomic absorption may not reach the detection limits of some emission methods, atomic absorption has

other advantages. There are fewer spectral interferences in atomic absorption because a darker region of the cell is observed, and the absorption signal responds only to the many atoms in their ground state, rather to the relatively few atoms in their many different excited states. Additionally, atomic absorption spectrophotometers may have better resolution than most emission spectrometers because the spectral resolution of the former is defined by the inherently narrow spectral line widths of the source and cell, while the spectral resolution in emission is limited by the spectral bandpass of the spectrometer. Moreover, spectral stability in atomic absorption is related to the spectral lines of the atoms in the source and cell, while in emission the monochromator or polychromator determines spectral stability.

In 1960, Gatehouse and Walsh [16] reported the use of cathodic sputtering to directly atomize a solid sample for atomic absorption analysis. In 1970, Stiring and Westwood [17] used the atomic absorption technique to detect atoms ejected from an aluminum cathode, measuring the rate of deposition of the sputtered material by using a piezoelectric microbalance capable of measuring deposition rates as small as 9.2×10^{-8} g/min. They reported that some of the sputtered material in the glow discharge exists in the form of molecules. Gandrud and Skogerboe [18] investigated the hollow cathode discharge as a means for vaporizing and atomizing samples for atomic absorption, studying the operational characteristics of the cell and obtaining detection limits between 1 to 10 ng for Ag, As, Ca, Cd, Hg, Pb, Se, and Zn. Stirling and Westwood [19] used atomic absorption spectroscopy to detect atoms sputtered from nickel and

iron cathodes in argon glow discharges. They suggested that some sputtered material is ejected from the cathode as molecules or groups of atoms because the observed spatial distribution of sputtered atoms differs from that predicted by diffusion theory.

In 1972, Walsh [20] reaffirmed that some important metals and alloys can be analyzed directly through cathodic sputtering, applying atomic absorption methods to the precise determination of major constituents and trace impurities. Gough [21] improved direct solid atomic absorption analysis by the use of gas flow rather than a static cell. The gas was introduced into the chamber through a hollow annulus positioned 0.5 mm above the surface. After entering in a direction parallel to the sample surface, the gas turned away from the sample and swept the atoms into the body of the chamber where they could be observed, thereby preventing diffusion losses and increasing absorption signals. Walsh also used a dual-modulation amplifier to obtain automatic compensation for background absorption and for any variation in the intensity of the atomic spectral lamp. McDonald [22] determined the concentrations of iron, chromium, nickel, and copper in a number of different alloys and in powdered metallic and nonmetallic samples by atomic absorption measurements of atomic vapors produced by cathodic sputtering. He compared the ratio of the analyte absorbance to the absorbance of an internal standard element in the sample. In 1982, McDonald [23] followed this study with an investigation of the atomic diffusion of two elements with quite different diffusion coefficients in a glow discharge.

A newly developed jet-enhanced sputtering atomizer, called the Atomsource (Analyte Corporation, Grants Pass, Oregon), uses six

high-velocity gas jets that are introduced at equally spaced intervals around the circumference of the exposed sample [7,8]. The jets are pointed in directions which cause them to directly impact the surface, not only changing the visual and electrical characteristics of the discharge, but also increasing the amount of material atomized, particularly where the jets impact the surface. The centering action of the jets and the high velocity of the gas flow cause the sputtered atoms to move rapidly into the center of the cell, away from the sample surface and the walls of the chamber. This reduces the loss of atoms resulting from deposition on the walls of the chamber and redeposition back on the sample.

2.2 Atomic Emission Spectrometry

The atomic emission analysis of metals and alloys is the most widely applied mode of analytical glow discharge operations. All of the commercially available glow discharge systems use a Grimm-type design and are presented as alternatives to the traditional arc-spark instruments used in metallurgical laboratories. The advantages of this new technique include increased precision, wide dynamic range, and low matrix effects, as well as the ability to obtain both bulk and depth-resolved elemental analysis with the same instrumentation. Bulk solid analysis is the principal application of glow discharge atomic emission spectrometry. In industry, this system is applied to the analysis of highly alloyed metals, including copper, nickel, and cobalt-based alloys, precious metals, and carbon steels [24].

In 1968, Grimm [25] described the first practical glow discharge

lamp for spectrochemical analysis with a flat cathode. A typical Grimm-type glow discharge lamp in which the electrically conducting sample is taken as the cathode, is restricting the discharge to the sample surface. This can be obtained by maintaining the distance between the anode tube on one side and the cathode block and the sample on the other, evacuating the interspace with a supplementary vacuum pump. The sample is atomized by cathodic sputtering and excited in the negative glow of the discharge mainly by electron impact. Emission is measured by end-on observation.

The influences of the sample composition and discharge parameters on the sputtering rate for the Grimm-type glow discharge lamp have been extensively investigated by two different groups [26,27]. Their results indicate that the electrical behavior of the discharge, characterized by its voltage-current parameters, is dependent upon the type of discharge gas and the pressure to which it is subjected, as well as on the composition of the sample, that is, the rate of erosion by cathode sputtering differs with samples of differing compositions and structures, and is further dependent upon the electrical parameters of the discharge gas and the pressure to which it is subjected. In most cases argon is used as the fill gas, as the heavier noble gases are expensive and their ionization energies are lower. The glow discharge may be operated with a typical voltage and current between 300-1000 V and 30-150 mA. A certain preburning time is required before the sputtering and excitation condition becomes stable, and this time may be as short as 20 s in the case of steel samples. When equilibrium conditions are reached, the composition of the sputtered material becomes equal to that of the sample, reducing

matrix interferences and structural effects.

In 1975, Radmacher and Swardt [28] performed analyses of steel and cast-iron by means of the Grimm glow discharge lamp (GDL), comparing these results with spark sources characterized by their high repetition rates (HRR). They reported that the GDL method showed better standard deviations and relative standard deviations than the HRR method for 14 elements, including C, Mn, P, S, Si, Cu, Ni, Cr, Mo, V, Al, Ti, Nb, and B. Bohmer et al. [29] determined the alloy and minor elements in copper-based alloys using a commercial Grimm glow-discharge source (RSV, Federal Republic of Germany). They reported a lack of inter-element effects from the use of this source and the possibility of wide dynamic range determinations through the use of a small number of standards. Accuracy for the major elements, including copper, are generally better than 0.2% relative. Ferreira and Butler [30] also determined the concentrations of certain alloying elements in silver metal, including gold, platinum, palladium and copper, which requires a rapid analytical method. They used an integrated sputtering factor as an internal standard and the concentration of silver was determined with relative standard deviations of less than 0.09%. The precision for gold, palladium, platinum and copper was less than 5% within the analytical ranges determined.

More recently, another group [31,32] investigated the effects of the metallurgical structure and the aluminum content of copper-aluminium alloy (1-12% Al) on the sputtering and intensities of spectral lines in the Grimm glow lamp. In their first investigation they reported that the electrical current and

sputtering yield decreased linearly with increasing aluminum contents; the intensities of the Al(I) lines depended linearly on the amount of aluminum in the sputtering yield at a fixed voltage and argon pressure.

The structure affected the intensities of the Al(I) and Cu(I) lines, but not the intensity ratio (Al(I)/Cu(I)), for about 100 s after the burn began. Working curves for aluminum of different structured samples were very similar.

In their subsequent report, the cathodic sputtering and emission intensities for the white, gray, and malleable cast-irons in the Grimm glow lamp were discussed. Intensities of the Fe 247.98-nm line for samples of the three types were linearly dependent upon electrical power, but the slopes of the plots differed. The intensity of the carbon line at 247.86-nm for malleable cast-iron was weaker than those for the others. It was observed that sputtering is influenced by the form of the graphite, which can lead to distortion of the electrical field. Graphite on malleable cast-iron is sputtered not only as atomic carbon, but also as moieties containing several carbon atoms. The higher the supplied voltage, the shorter the time for the intensities of the Fe(I) and C(I) lines to reach constant values.

The sputter atomization processes in a glow discharge have also been used for depth-resolved analyses. In this application, the response of the analyte signal is related to the sample removal depth. One of the earliest applications of this methodology [33] was the depth-resolved analysis of alloy component diffusion in stainless steels with compositional variations in depth due to mass transfer in

liquid sodium tests for materials studied in the fast breeder reactor program. Integrated exposures of successive layers of attack were spectrographically recorded, and the total weight loss was determined by gravimetric methods. Sequential analyses of metal alloys in depths of 0.1 to 40 μm were obtained.

This technique was applied to an in-depth analysis of a sample of annealed steel sheet, which had an off-luster appearance, to determine whether any significant difference in elemental composition existed between the surface and subsurface layers of the sample [34]. The power supply of the source was operated in either a constant DC mode or a square-wave DC mode, achieving improved repeatability and accuracy with the latter mode.

More recently, Bengtson [35] examined the emission intensity from spectral lines, particularly the variation in intensity of Ar(I) lines in order to exclude the influence of the sample sputtering rate, and intensity variations of several analytical lines for a comparison with the sample sputtering rate. It was concluded that the sample atom number density in the plasma was saturated as discharge voltage was increased. An application of this technique to a surface analysis problem was investigated, and good agreement was obtained when compared to atomic absorption measurements.

Pons-Corbeau [36] studied the fundamental relationship between the intensity of spectral emission of an element and its concentration at the surface of the sample, investigating these factors for different materials, such as metallic alloys, oxidized matrices, and matrices submitted to ionic implantation. Pons-Corbeau et al. [37] subsequently used glow discharge techniques for the

quantitative determination of composition variations in galvanized coatings and for estimations of enrichments on the surface of annealed, extra mild steel sheets. The sputtering rates for this system was reported as 70 and 200 nm/s.

Recently, the analysis of nonconducting powder sample types by the use of an Analyte Atomsource (Grants Pass, OR) had been studied [38]. Samples were prepared by pressing a mixture of an oxide powder with a copper host matrix (1:9). Sample-to-sample precisions were reported on the order of 3-4 % for iron in a geological specimen. Results showed the ability to perform analyses of samples such as ceramics, glasses, and refractory-based catalysts.

Dogan, Laqua and Massmann [39,40] first analyzed nonconducting samples which were ground and mixed with a current conducting material (e.g. copper powder), then formed into pellets. They reported that the precision of the analyses was high when suitable measuring techniques were used, and that the calibration curves were linear in a wide range of concentrations. Matrix and inter-element effects were small and in many cases not detectable. Optimal sample-to-host ratios were generally found to be on the order of 1:3 to 1:5.

In 1983, Caroli et al. [41] investigated the applicability of the hollow cathode emission source for the determination of trace elements in mineral residues from the ashing of biological materials. The samples were diluted with a 1:4 graphite-copper powder mixture and pressed into the form of hollow cylinders with an internal standard spike of Ga. Synthetic specimens containing Ag, Al, B, Cr, Mn, Ni, Pb, Sn, Ti and Zn, and a matrix similar to that of

organic materials after mineralization, were analyzed. Detection limits ranged from 0.1 ppm for chromium to 5 ppm for lead, with elemental calibration curves showing linearity over at least two orders of magnitude. Boosted-output [42] and hollow cathode plumes [43,44], with a variety of host conducting materials, including copper, gold, silver and graphite, were also applied to the analysis of geological samples. Mai and Scholze [45] focused specifically upon the atomic transport phenomena in a glow discharge source during an analysis of powder, resulting in a substantial reduction of matrix effects for both finely dispersed single and polyphase analytical substances. Particular attention was paid to the investigation of atomic transport phenomena in the near surface region of the specimens and from the discharge back onto the surface (redeposition).

A glow discharge device designed for solution analysis has been used in a number of investigations [46-49]. The detection limits obtained with such a device [48] are comparable to those obtained with demountable hollow cathode lamps, but with improved precision reported. In 1983, Brackett and Vickers [49] developed an interesting device which provides continuous sample introduction into a low pressure glow discharge through use of a chain conveyor. The detection limit for Pb in dried solutions was reported as 0.9 ppm, suggesting that the device could be used as an element selective detector for liquid chromatography.

The scanning electron microscope (SEM) has been used to study the microstructures that are produced on the cathode surface during ionic bombardment [50-52]. In 1974, Jager and Brum [50] investigated the

cross-sections produced by a glow discharge with a SEM through burn-spots on brass and gold samples containing lead. They found the lead in the form of inclusions, results which showed that ion bombardment of the lead-rich sample attracted inclusions to a lesser degree than did the matrix and cones formed on the sample surface during sputtering. They concluded that the formation of cones during the sputtering of the sample is caused by the presence of inclusions with high lead concentrations, inclusions which are more resistant than the matrix to sputtering.

In turn, Harrison et al. [51,52] examined the effect of discharge gas, sputter time, current, pressure, and cathode material on the microstructures arising on the cathode surface during sputtering.

There have been any number of fundamental spectroscopic investigations of the glow discharge [53-69]. Debrosavljevic and Marinkovic [53] investigated some of the excitation characteristics of the discharge for a graphite cathode coated with evaporated films of copper, iron, manganese, or titanium, and argon or helium gas. The excitation temperatures for iron, manganese and titanium were determined at 0.4 A discharge current and various fill gas pressures. These temperatures are in the range between 4000 and 4600 K and do not systematically depend on the type of fill gas (Ar or He), nor on the fill gas pressure.

In 1976, Human et al. [54] determined the shapes of the emission lines of calcium and chromium with a pressure-scanning Fabry-Perot interferometer, using various excitation conditions for different concentrations of the metals in standard matrices. It was found that

considerable self-absorption and reversal occur at higher currents and concentrations.

The kinetic gas temperature and electron densities were derived from the line profiles of Ar I 415.8 nm and He 447.1 nm [55]. The maximum Doppler temperature measured in the side-view lamp, as derived from the Cr 428.9 nm line profiles at discharge conditions of 800 V and 60 mA with a copper matrix cathode, was 1513 K, and the temperature in the front-view lamp was 1465 K. The He 447.1 nm line profiles measured in the side-view lamp gave electron densities in excess of 10^{14} cm^{-3}. An investigation of the roles of metastable argon atoms in a low pressure pulsed discharge was performed to find the cause of emission from sputtered metal atoms in the afterglow of an atomic fluorimeter [58]. Results showed that low energy electrons in the afterglow are converted to high energy electrons via the recombination of electrons with argon ions and subsequent collisions of pairs of metastable atoms.

The distribution of metastable argon atoms was determined at different discharge conditions and at distances varying from 0.25 to 6-mm from the cathode by measuring the metastable argon atom absorbance [59].

In general, there are three possible processes for producing excited levels of ionized sample atoms: direct electron impact ionization, Penning ionization, and charge transfer ionization. Harrison [61] investigated the role of metastable atoms in glow discharge ionization processes by using a turnable laser to depopulate metastable atom populations, studying the effects by optical galvanic spectroscopy and mass spectrometry. It was found

that depopulation of the metastables in the neon discharge caused a general reduction in all measured ion signals. Similar studies with argon showed that many species with ionization potentials greater than the metastable energies of argon were not affected by laser depopulation. These results show that Penning ionization plays an important role in a glow discharge. Steers and Fielding [62] studied the charge transfer excitation processes with a copper-argon system in the Grimm lamp. Using this system, it was found that the 224.7-nm Cu II line is exceptionally intense, and it is argued that the upper level concerned is populated by charge-transfer excitation.

Wagatsuma and Hirokawa [63-69] have continuously investigated ion sputtering in a glow discharge plasma by an emission spectroscopic method. In addition, considerable research has been performed on the development of new glow discharge atomic emission sources. Grimm-type discharges reflecting different geometrics and operating powers are being investigated in several research projects [70-78]. In 1970, a high frequency discharge of 2450 MHz was used to excited the spectral lines of elements [70]. To increase the excitation of sample atoms sputtered by the glow discharge, secondary discharge [71] or radio-frequency [72] was used. Laqua et al. [73,74] used a magnetic field glow discharge source (MFGDS) to evaluate an analysis of mild and alloy steels. A boosted glow discharge lamp [75] and an r.f.-boosted, pulsed, hollow cathode lamp [76] were also constructed by other research groups. Ko [77] and Human et al. [78] have constructed new glow discharge lamp designs for the analysis of metals.

2.3 Mass Spectrometry

The glow discharge can also be used as an ion source for mass spectrometry, a feature demonstrated as early as 1886 by Goldstein [79]. Among pioneer efforts in mass spectroscopy, Aston used the glow discharge as an ion source for determination of isotope ratios, and Bainbridge [80] used a glow discharge tube in which zinc was sputtered from the cathode to correctly determine its isotope ratios.

The early gas discharge ion sources [81] were operated at a cathode-anode potential of 10,000 to 50,000 V and a gas pressure of 0.001 to 0.1 torr (0.133 to 13.3 Pa), or at a relatively high potential and low pressure compared to recent glow discharges normally operated at a few hundred volts and 1 to 10 torr pressure. Positive ions were extracted through a 1.0-mm cathode exit hole, producing ion beams up to several milliamperes intensity.

This early version of discharge ion sources fell into disuse as a result of the source disadvantages and the development of more suitable sources for organic materials. The source disadvantages included: (a) requiring a heavy differential pump to the operate the interface of a low pressure mass spectrometer with a relatively high pressure glow discharge; (b) the instability of ion beams due to the need for high operating discharge voltages; and (c) the inability to control the energy of the ionizing electron.

The development of the spark discharge source provided a source suitable for both the vaporization and ionization of inorganic samples. Although this source has excellent sensitivity advantages

for good ionization efficiency and a number of varieties of sample types, it does pose several problems. These problems include a fluctuating ion beam, resulting in poor analytical precision, and a large ion energy spread requiring use of an expensive double focusing mass spectrometer.

The development of secondary ion mass spectrometry (SIMS) [82] provides a brighter area for analysis of inorganic samples. The secondary ions from the sample surface are released by striking the energetic primary ions, and then these secondary ions are extracted and analyzed. This technique provides a good tool for both bulk analysis and depth profile determination. The disadvantages are similar to those of the spark source, such as poor analytical precision, and expensive price.

Recently, the glow discharge source has been applied to optical spectroscopy, including analytical applications, due to its stability, precision, and sensitivity. The hollow cathode discharge lamp has been used as a sharp line source in physics research [83,84] and more widely in atomic absorption spectrometry [85,86]. Glow discharge sources have also been used for analytical emission spectrometry [87-89].

Coburn et al. [90] used glow discharges as ion sources to analyze thin film and bulk samples. Oechsner and Gerhard [91,92] reported on direct solid analysis by using a high frequency plasma source interfaced to a mass spectrometer to sputter and ionize the samples.

In 1974, Harrison and Magee [93] interfaced demountable hollow cathode tubes and a mass spectrometer, finding that the hollow discharge tube provides a good ionization source for both solids and

trace elements in a solution deposited on the surface of the cathode and dried to a residual film. Evans and Colby [94] described a simple hollow cathode ion source for the mass spectrometry of conducting solids, obtaining broad elemental coverage with detection limits in the sub-ppm range by the use of clean argon support gas.

In 1975, Harrison and Daughtrey [95] studied the effects of a number of critical parameters, including pressure, current, and discharge gas, on the hollow cathode ion source. They reported the precision of trace metal determination of 17-22% RSD, and detection limits in the sub-ppm range for solutions and the ppm range for solids.

Evans and co-workers [96] showed the affect of cathode geometry on cathodic ion intensities. They found the cathode bore depth and diameter affect sensitivity dramatically, with the shallowest and largest bores producing the greatest cathodic ion intensity.

Harrison et al. [97-102] combined a glow discharge source with a versatile quadrupole mass filter for trace element determinations in conducting solids or solution residues, examining the predominant ionization mechanisms, believed to be electron impact and Penning modes, in the discharge. Subsequently, the same investigators [101] used a dual-discharge ionization source, obtaining not only enhanced sensitivity, but a reduction in the population of certain molecular species.

In 1981, Coburn and Harrison [102] discussed the advantages that a low pressure glow discharge ion source has over secondary ion mass spectrometry and spark discharges for direct solid sample analysis, elemental composition depth profiles, and condensed solution

samples. The advantages of this techniques are good stability, precision, sensitivity, and lower costs.

In 1983, the first commercial glow discharge mass spectrometer [103] was introduced with the VG9000 (VG Elemental, Great Britain), leading to the direct analysis of electrically conducting and semi-conducting solid materials, nonconducting materials mixed with electrically conducting materials such as graphite, and liquid samples, observed after absorption into a suitable support matrix.

Harrison et al. [104] showed the analytical utility of resonance ionization mass spectrometry for increasing the ionization efficiency, while Stuewer et al. [105,106] constructed two new glow discharge ion sources used with quadrupole mass spectrometers, studying the influences of electrode arrangement, plasma sampling and ion optics. With these optimized sources, they reduced the intensity of interfering molecular ions and increased the abundance of ions of the analyte by several orders of magnitude. They also performed routine elemental analysis of steel. In a multi-elemental analysis of steel, they reported a detection limit of 0.1 μmol/mol and the analytical results for the two test samples with 30 elements were in agreement within 10% of the certified values.

Recently, Harrison and Bentz [107] comprehensively reviewed glow discharge mass spectrometer and noted that this method has the potential of developing into a major analytical method.

III. INSTRUMENTATION

1. Introduction

Various types of single-jet glow discharge sources and a modified six-jet Atomsource were developed and investigated by atomic absorption, emission and mass spectrometry. The instrumentation used for this research originates from a variety of sources including commercial manufacturers and previous research projects. Much of it had to be modified and developed to obtain the desired experimental system.

In this research, the first step was developing a single-jet glow discharge source for fundamental studies using atomic spectroscopy. Figure III.1 shows the overall instrumental configuration for the atomic spectroscopic measurements. The next step was interfacing a commercial six-jet Atomsource with a commercial VG PlasmaQuad ICP-MS, replacing the ICP.

2. Glow Discharge Cell

2.1 Single-jet Glow Discharge Cell

Figure III.2 is a schematic diagram of the first version of the single-jet glow discharge source designed to study the effect of gas flow on sputtering. The body of the cell is made of glass with two

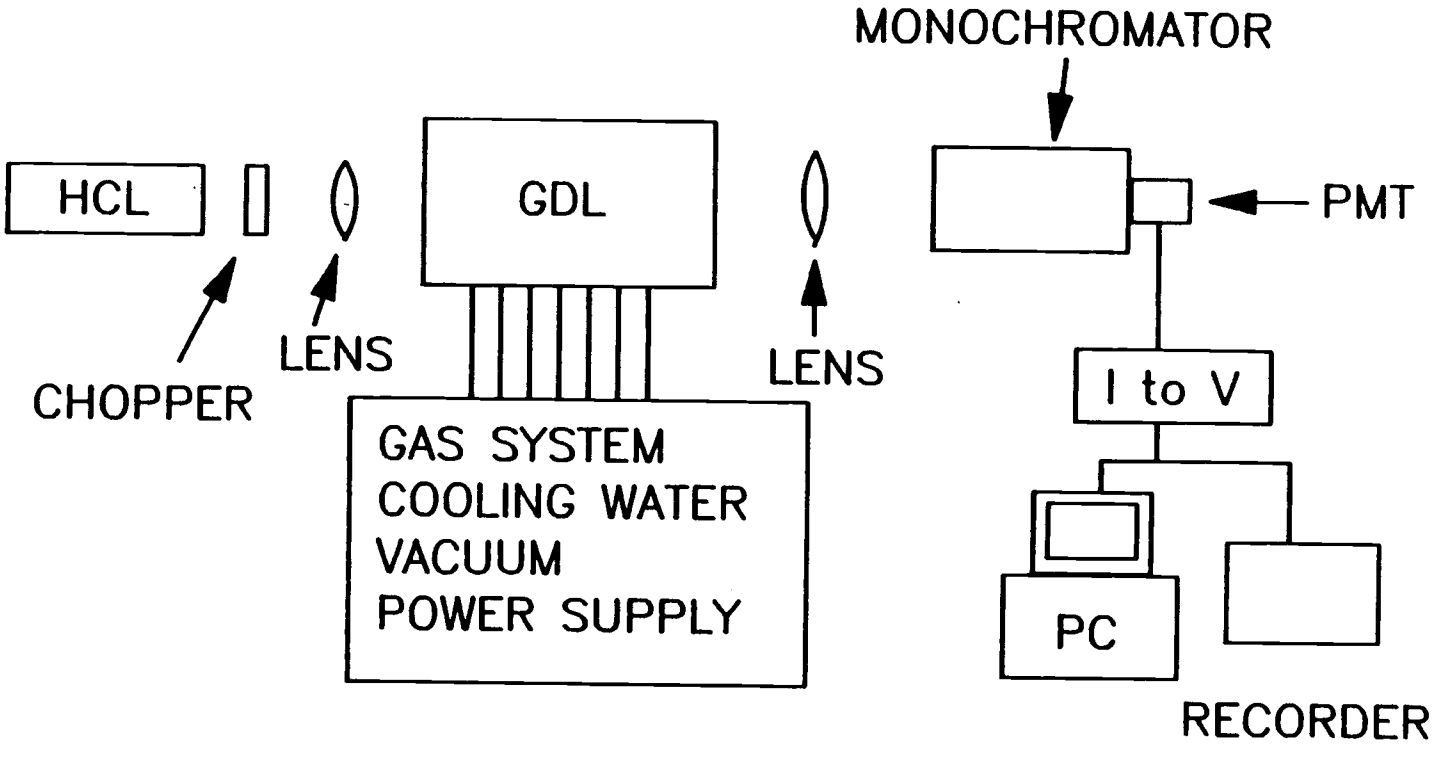

Figure III.1 Overall instrumentation configuration for atomic spectroscopic measurements.

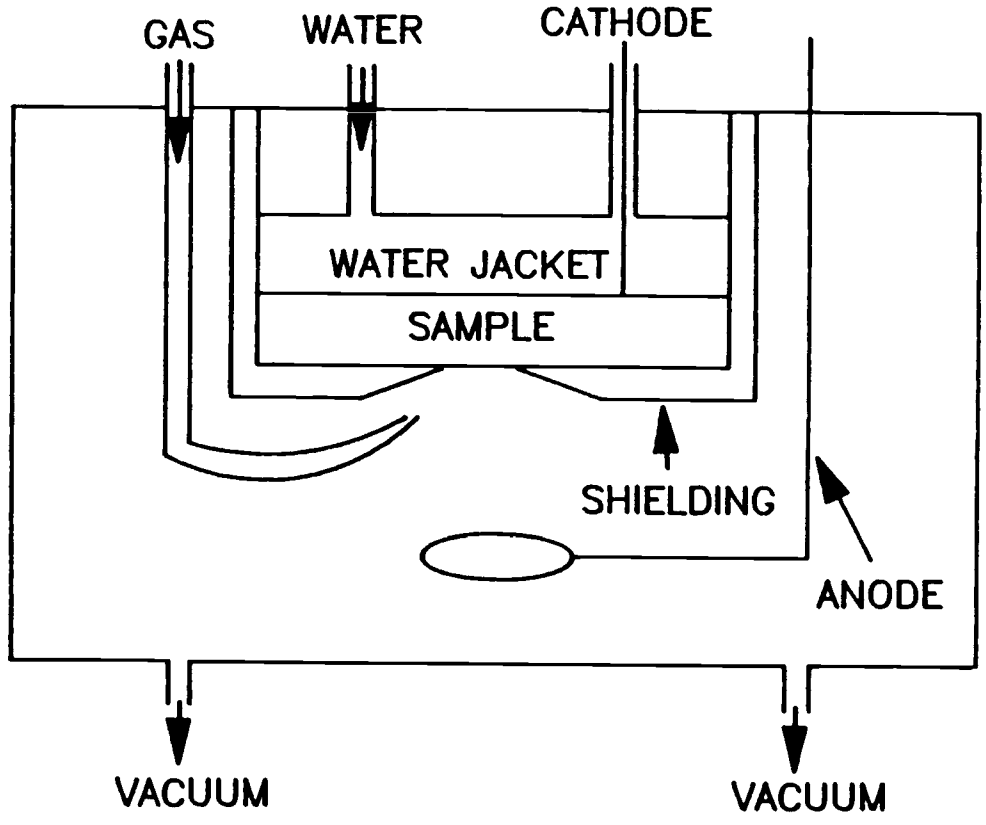

Figure III.2 Schematic diagram of the first version of the single-jet glow discharge source designed to study the flow effect on sputtering.

quartz windows (O.D.=2.5 cm) to provide an optical path for the absorbance measurements. Two exhaust ports, a vacuum pump and a gas flow control valve are used for initial evacuation and to maintain a low pressure (1 to 10 torr). The cathode is a demountable copper plate 1.0-cm in thickness and attached to a water-cooled support. Flat samples with four screw holes can be attached to the cathode support with four plastic screws. Teflon tape is used to insulate and shield the cathode and the support.

The gas inlet port is a glass tube of 0.5-cm O.D. with a jet nozzle of 200-μm I.D. at its end. The jet nozzle size and the angle between the sample surface and the jet nozzle were changed by softening the glass with a flame. The anode located beneath the cathode is a ring of 2-cm diameter and is made from a copper wire of 2-mm O.D. The gas flow rate is monitored accurately by a thermal-mass flowmeter. Later, a new single-jet glow discharge was developed since in the first version it was difficult to replace the sample.

Figure III.3 shows the schematic diagram of the new single-jet glow discharge source designed to easily replace the sample. The body of the cell is made of Delrin with two quartz windows (O.D.= 1.5 cm). The cathode is a demountable copper rod 0.5 cm in diameter and attached to a water-cooled support.

The anode is a brass tube of 0.5-cm O.D. with a detachable single jet nozzle of 200 μm I.D. located above the cathode. This anode is also used for the gas inlet port. The distance between the cathode and anode can be adjusted with a micrometer.

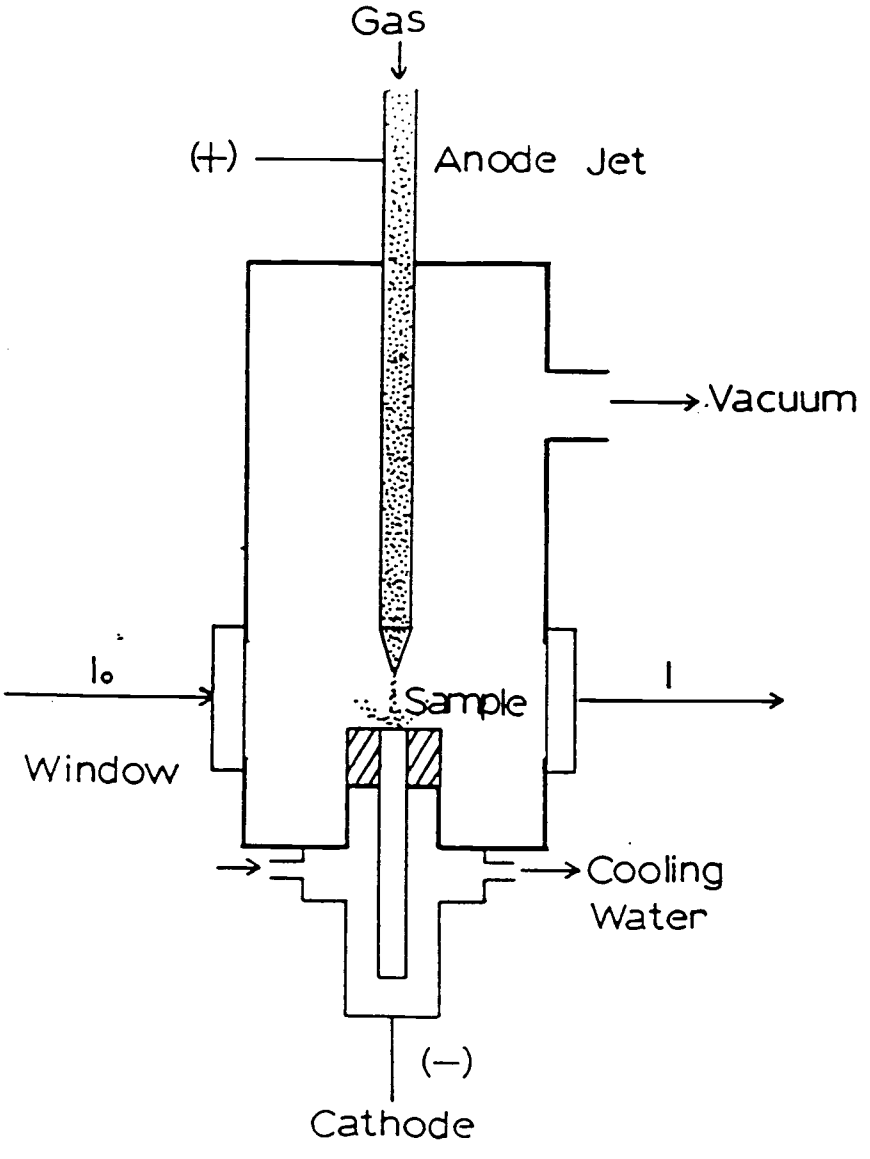

Figure III.3 Schematic diagram of the new single-jet glow discharge source designed to replace the sample easily.

2.2 Six-jet Glow Discharge Cell

Following a suggestion by Walsh et al.[20], Gough [21] improved direct solid atomic absorption analysis by using a flowing gas cell instead of a static cell. The gas enter the chamber with a high velocity through a hollow annulus located 0.5 mm above the surface. After entering in a direction parallel to the sample surface, the gas turned away from the sample towards the body of the chamber. The sputtered atoms that had diffused from the sample surface into the path of the gas were swept into the body of the chamber where they were observed. A newly developed atomizer uses six high-velocity gas jets that are pointed at and impinge upon the sample surface. (This is in contrast to Gough [21] where the gas enters parallel to and 0.5 mm above the surface.)

The six-jet glow discharge cell was originally developed by the Analyte Corporation (Grants Pass, Oregon) and they provide the research funds for the fundamental studies and some applications. The six-jet Atomsource consists of three separate components, a solid sample atomizer, an operator input/output box, and a control unit. The solid sample atomizer shown schematically in Figure III.4 consists of a Delrin chamber that is internally 17.2 cm long and 3.8 cm in diameter with demountable quartz windows at each end. A water cooled copper cathode plate on the side of the chamber helps to stabilize the sample temperature during the analysis. The flat sample is sealed over a 0.8-cm diameter hole in the cathode plate with an o-ring. Any piece of metal or alloy with a 1" (2.5-cm) minimum diameter flat surface may be analyzed directly. The six jet

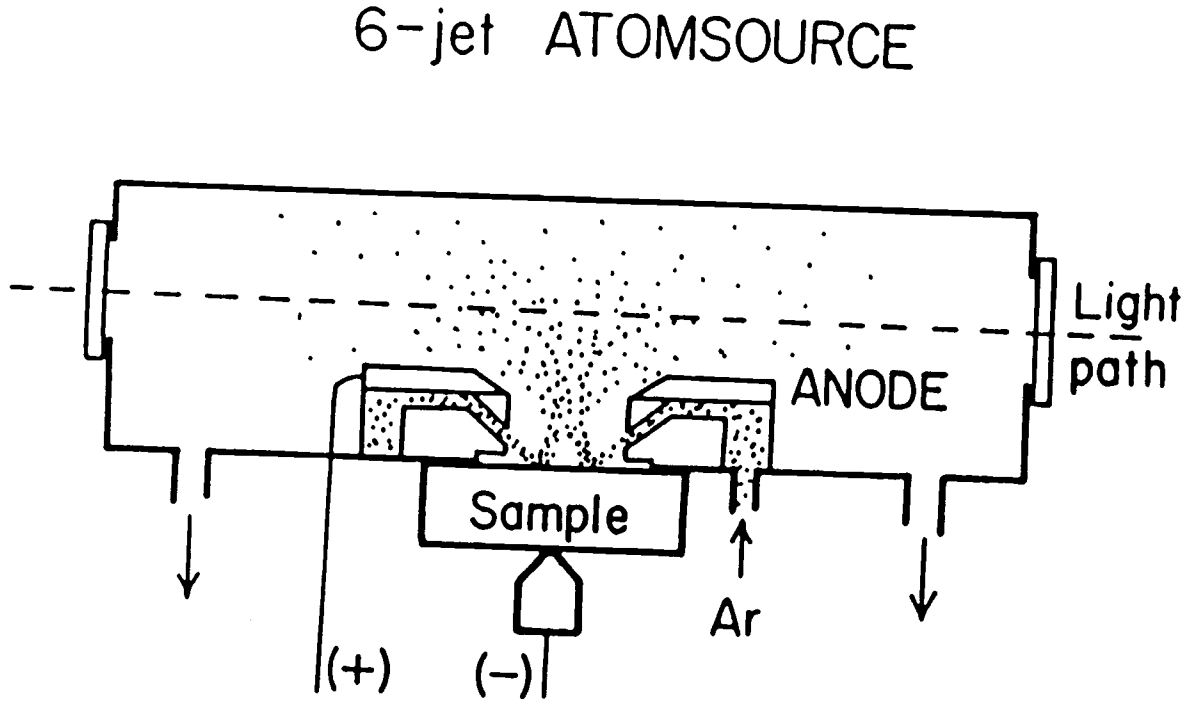

Figure III.4 Schematic diagram of the six-jet Atomsource

nozzles are located 1 mm from the front of the sample and are pointed so that high velocity jets of gas are directed towards the center and at an angle against the sample surface. The Atomsource system can be installed on any conventional atomic absorption spectrophotometer in place of a flame atomizer.

The operator input/output box is controlled by a keyboard which provides for data entry and start-stop functions. An LCD display and audio signal give the operator system feedback.

The system program is stored in Erasable Programmable Read-Only Memory (EPROM). All operator programmable variables used to control the atomization parameters are stored in non-volatile memory while other program variables are stored in Random Access Memory (RAM). An RS-232 port has been provided to allow for interfacing to a modem, printer, or communication with another system. The CPU monitors and controls the atomization process utilizing signals from sensors, including positive pressure, partial pressure, emission intensity, cathode plate temperature, control unit temperature, atomizer supply current and voltage, low voltage supplies and line voltage.

3. Glow Discharge Mount and Pressure Control System

3.1 Optical Table Configuration and Glow Discharge Mount

The hollow cathode lamp, vacuum measurement, assorted optics, glow discharge cell and its stage are mounted on a 4 x 10 foot optical table (Newport Research Corporation, Fountain Valley, CA) tapped with ¼-20 screw holes on 1-inch centers. Figure III.5 shows

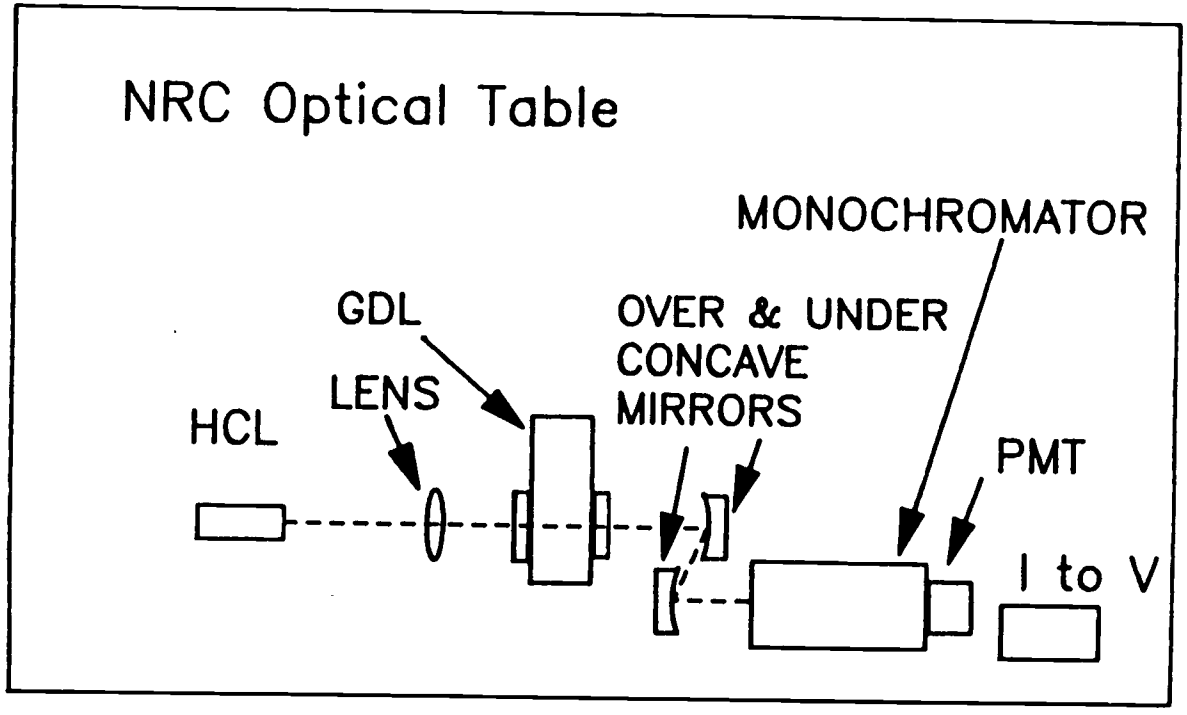

Figure III.5 Configuration of the components mounted on the optical table.

the configuration of the components mounted on the table.

Both the single-jet and six-jet Atomsource were mounted on a vertically and transversely adjustable stage. This stage has two 360° manual dials to set the position. Each turn is equivalent to 1.0 mm of movement. This stage was used for the spatially resolved atomic absorption and/or emission measurements.

3.2 Glow Discharge Pressure and Gas Flow Rate Control System

In the six-jet Atomsource, a closed loop servo is used to control pressure in the atomizer. A pressure sensor provides feedback to the servo amplifier which then adjusts a motor-controlled valve in the flowing gas system to maintain constant atomizer pressure. Between runs the atomizer is maintained at a positive pressure. The measured calibration between gas flow rate and pressure is listed in Table III.1. A mass flowmeter (Sierra Instrument, Carmel Valley, California) with a micrometer valve was added to the gas inlet so that pressure and flow rate could be set independently.

In the single-jet glow discharge cell, the pressure control system is composed of an assembly of pipes, valves, a gas inlet port, a vacuum pump and a pressure transducer as shown in Figure III.6. This manual pressure control system is used for evacuating the sample chamber and filling it to a desired pressure with a specific gas or gas mixture. All components, except for the vacuum pump and glow discharge cell, are made of stainless steel or glass.

The primary component of this system is the pressure transducer which is used to provide exact pressure information on the glow

Table III.1 Calibration between the gas flow rate and pressure in a six-jet Atomsource.

Gas Flow Rate (L/min)	Pressure (Torr)
0.040	1.05
0.105	2.08
0.182	3.08
0.272	4.05
0.422	5.40
0.492	6.08
0.600	7.08
0.700	8.14
0.800	9.10
0.900	10.0
1.00	11.1
1.09	12.2
1.18	13.0
1.31	14.0
1.43	15.4
1.65	18.0
1.75	19.0

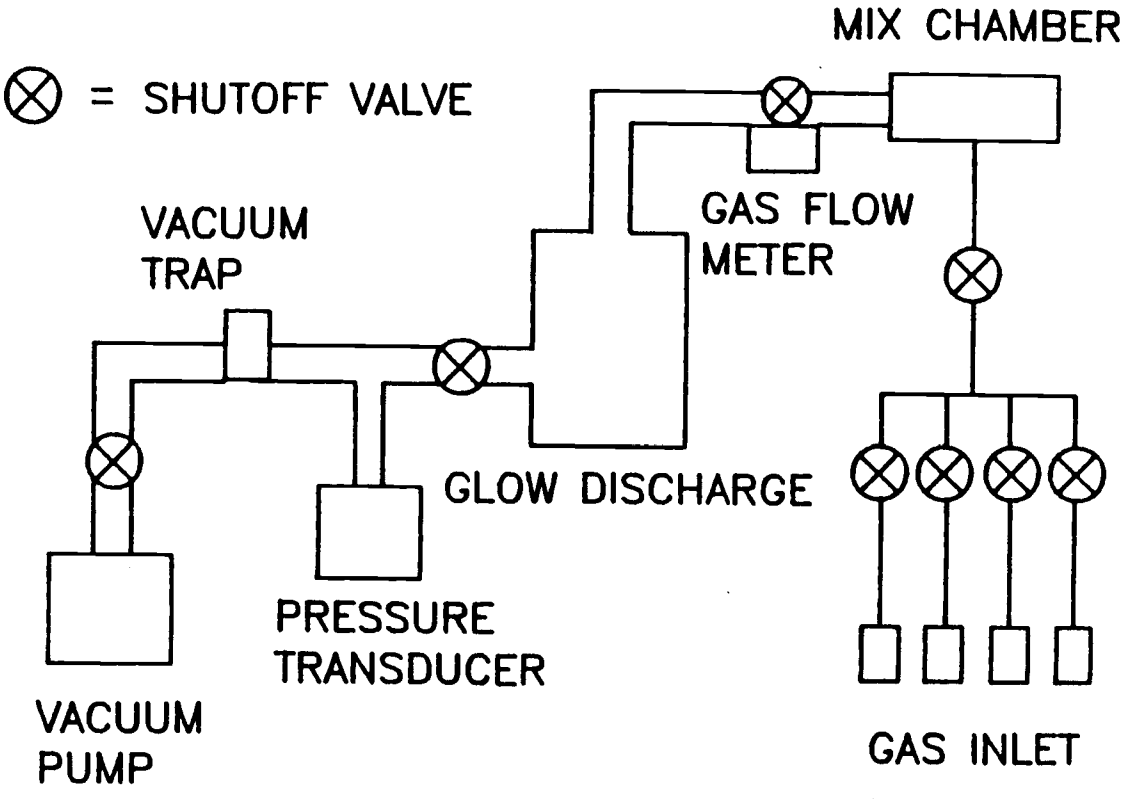

Figure III.6 Pressure control system in a single-jet glow discharge cell.

discharge cell. A variable reluctance transducer (Validyne # AP10) is used with a carrier demodulator (Validyne # CD15) to provide a d.c. voltage proportional to the glow discharge pressure. The transducer gives pressure readings which are independent of the type of gas in which the pressure is being measured. Following a suggestion by Beenen [108], the calibration of the transducer is performed first at room pressure and then at vacuum. The room pressure calibration is done with the glow discharge cell exposed to the room without gas flow. The "span" control on the transducer demodulator is then adjusted until its output voltage is proportional (10 mV/torr) to the room pressure read off a mercury barometer kept in the laboratory. The vacuum calibration is performed by evacuating the glow discharge cell with a vacuum rotary pump for a minimum of 2 hours without gas flow. The chamber pressure at this time is monitored with another high vacuum pressure gauge (Phillips, series 275) and is less than 0.01 torr, corresponding to the smallest transducer output voltage measurable with a standard DVM (0.1 mV). After 2 hours of pumping, the demodulator "zero" control is adjusted for an output voltage of 0.0 mV.

This system normally runs with flow-through experiments where one or more gases are continuously passed through the chamber while maintaining a constant pressure in the chamber. A mass flowmeter (Sierra Instrument, Carmel Valley, California) used to control the gas flow was added to the gas inlet so that pressure and flow rate could be set independently. The calibration of the gas flow rate was performed with another gas flowmeter which had been calibrated with a bubble meter in our laboratory. The calibration between gas flow

rate and output voltage monitored by the Digital Volts Meter (DVM) is listed in Table III.2.

The other components of the pressure control system are an ordered assembly of various valves and pipes. As shown in Figure III.6, up to four gases can be input into the system via four gas flowmeters (model #601, 602, Matheson Gas Products, Secaucus, NJ) from standard gas cylinders.

3.3 System Leaks

To check for system leakage, the vacuum chamber and other parts of the vacuum system were evacuated over a two-day period. All valves were then closed for the two-day period to isolate each section of the vacuum system. Under this configuration, the pressure transducer monitors the pressure in only the sample chamber. The chamber pressure which did not vary by more than 0.16 torr over the observation time period indicated the system was tight. This corresponds to a maximum leakage rate of 0.003 torr/hour for the sample chamber. When leakage occurred, a low pressure leakage detector (He leakage detector, Dupon) was used to find the position of the leak.

Table III.2 Calibration between the gas flow rate and output voltage monitored by DVM.

Output Voltage (mV)	Gas Flow Rate (L/min)
100	0.020
200	0.041
300	0.060
400	0.080
500	0.10
600	0.12
700	0.14
800	0.16
900	0.18
1000	0.20

4. Optical Instrumentation and Transfer Hardware

4.1 Introduction

The optical system includes one convex lens used to focus the hollow cathode lamp emission onto the discharge cell, and two parabolic mirrors used to focus the discharge cell onto the monochromator entrance slit. The monochromator is used to spectrally and spatially isolate emission radiation. Each of these components will be discussed in detail in this section.

All optical components are secured to a 5' x 8' x 1/2" steel optical table. Mirrors are mounted on in-house designed mirror mounts which provide for vertical and horizontal angular positioning. All mirror mounts, except those used to direct the hollow cathode lamp, are secured to 1.500" diameter steel rods of various heights. The mirror mounts can be secured at any height on these rods. Each rod has a base platform which may be bolted anywhere on the optical table. For this purpose, tapped holes have been placed on 1.00-inch centers throughout the table top. The entire optical system was designed by Hosch [109] and is more thoroughly discussed by Lewis [110].

4.2 Focusing Lens and Radiation Transfer Mirrors

The emission of the hollow cathode lamp is focused into the glow discharge cell with a 25-mm diameter symmetrical convex spherical

silica lens. The nominal focal length of this f/6.0 lens is 150 mm.

Emission from the discharge cell and hollow cathode lamp is transferred to the monochromator with two 51-mm diameter parabolic, uv-enhanced aluminum first-surface, 350-mm focal length mirrors in an over-and-under configuration. These mirrors also serve to cancel the astigmatism generated by the use of a similar pair of mirrors in the emission monochromator.

4.3 Emission Monochromator

A Heath EUW-700 0.35-m Czerny-Turner grating monochromator (Heath Instruments, Benton Harbor, MI) is used as the emission monochromator. The f/6.8, 35-cm monochromator employs a 48-mm square plane grating (blazed for 200 nm) with 1180 lines/mm, giving it a reciprocal linear dispersion of 2 nm/mm in the first order. The monochromator slitwidth is manually controlled and adjustable from 0 to 1500 μm. The wavelength drive mechanism can be slewed in either direction or scanned in the increasing wavelength direction. A manufacturer supplied scanning control unit allows for one of nine programmed scan rates between 0.05 Å/s and 20 Å/s.

The slitwidth control dial on the monochromator was calibrated using a mercury hollow cathode lamp (HCL). The monochromator was tuned to the mercury line at 546.074 nm. The HCL intensity at the monochromator exit slit was detected with a photomultiplier tube biased at -1000 V. The output of the PMT was fed into a current to voltage converter operational amplifier circuit with a 100-MΩ feedback resistor and a 0.001-s RC time constant in the feedback

loop. The voltage is converted to a digital form with a DASH-16 analog to digital input/output expansion board (Metrabyte, Taunton, MA) and stored in an IBM-PC computer.

The output signal was shown to be linearly related to the slitwidth dial reading as expected for a spectral line source. Extrapolation of this line to zero signal (slits closed) gives a dial setting of 34 μm.

The wavelength dial on the monochromator was also calibrated using the same experimental setup. Twelve mercury lines between 574 and 254 nm were chosen for this calibration. The slitwidth was maintained at 100 μm and the PMT bias potential was adjusted to give an output voltage of approximately 7.5 V (half scale on 15 V ADC readout). The monochromator was scanned through each line twice, with the wavelength dial reading at the signal maximum recorded on the second trial. The recorded wavelength dial settings are compared to literature values [111] for these transitions in Table III.3. As shown, the monochromator wavelength dial typically reads 34 Å below the true wavelength. Later in this research, 34 Å was used for a constant offset of the monochromator wavelength.

4.4 Photomultiplier Tube

A RCA C31034 end-on photomultiplier tube (PMT) was used as the optical transducer. It employs a gallium-arsenide photocathode giving it an approximate spectral range of 200 to 930 nm. The photocathode sensitivity varies from 90 mA/W at 300 nm to 110 mA/W at 860 nm. An 11-stage dynode chain is used for photoelectron

Table III.3 Calibration of Heath monochromator wavelength dial using mercury light source.

Hg Line Wavelength (Å)	Monochromator Dial Setting	Difference
5790.65	5783.3	7.35
5769.59	5762.5	7.09
5460.74	5453.5	7.24
4358.35	4351.3	7.05
4077.81	4070.5	7.41
4046.56	4040.0	6.56
3654.83	3647.5	7.33
3341.48	3334.5	6.98
3125.66	3118.2	7.46
3021.50	3014.5	7.00
2752.78	2745.4	7.38
2536.52	2530.0	6.52
	AVG. of differences =	7.11
	STD. of differences =	0.31

amplification giving the PMT a current amplification of 8000 when biased at -1000 V. The relative gain of the PMT was investigated as a function of bias potential between -800 and -1100 V at the mercury 302.14-nm transition as listed in Table III.4.

5. Optical Radiation Source and Signal Measurements

In the absorption experiments, commercial (Westinghouse) hollow cathode lamps (HCL) were used for the spectral line source. A Heath EUW-15 DC power supply with a series of 5 KΩ resistor was used for the HCL power supply. A 5-mA lamp current measured with a Knight DC milliamperes meter was used for in this study. A mechanical chopper was used in front of the lamp to help in rejecting the background emission signal. Figure III.7 shows the circuit schematic for the background emission signal rejection, while the components are listed in Table III.5. The current signal generated by the PMT is converted to a voltage by a current to voltage converter operational amplifier circuit A. The AC component (HCL) of the total emission signal (HCL plus background emission, Point 1 in Figure III.7) is isolated by a high pass filter circuit R2C2. Then the AC signal at point 2 is amplified by the voltage inverter circuit of amplifier C and converted to a rectified AC signal by the circuit of amplifier D. The rectified AC signal at point 3 is smoothed by a low pass filter circuit R5C4. In some experiments, a pulsed HCL synchronized with a computer was used to compensate for the background emission.

Table III.4 Relative gain of RCA C31034 PMT as a function of bias potential.

PMT Bias Voltage (-V)	Relative Gain
800	1.0
820	1.1
840	1.2
860	1.4
880	1.6
900	1.8
920	2.1
940	2.4
960	2.7
980	3.2
1000	3.7
1020	4.4
1040	5.2
1060	6.4
1080	7.9
1100	9.1

Table III.5 List of electronic components used in rejecting the background emission signal

Designation	Description	Other Comments	# Used
	RESISTORS		
R1	100 MΩ		1
R2	100 KΩ		2
R3	1 MΩ		1
R4	10 KΩ		2
R5	120 Ω		1
	CAPACITORS		
C1	0.1 μF	Electrolytic	1
C2	0.047 μF	Electrolytic	1
C3	330 μF	Electrolytic	1
C4	1 μF	Electrolytic	1
	DIODES		
D1	Rectifier	Type IN4733	2
	OPERATIONAL AMPLIFIERS		
A	LF356H		1
B	TL081		1
C	CA3140		1
D	TL081		1

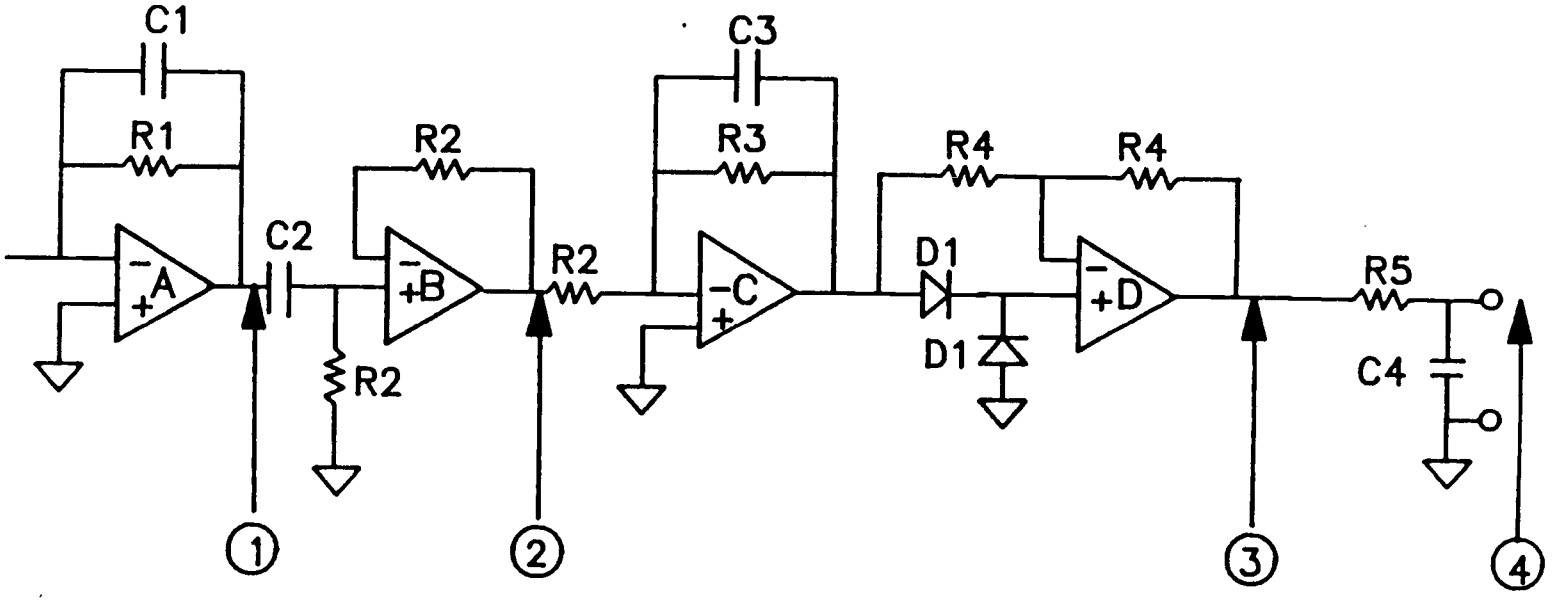

Figure III.7 Circuit diagram for background emission rejection.

6. Computer Hardware and Control Software

6.1 Introduction

The microcomputer has become an important component of most analytical instrumentation. As the complexity of an instrument increases, the demands for automation, synchronization control, and acquisition functions also increase. The microcomputer is ideally suited to meeting these demands. In addition, the microcomputer is also a powerful tool for the rapid and efficient analysis and presentation of experimental data. Both the hardware and software that were developed to accomplish this control are outlined in the following sections.

Electronic circuits are used as a part of the instrumentation to process electrical signals generated by optical transducers, and generate timing pulses and delays to insure precise sequencing of experimental events. Many of these circuits provide for computer access and control of critical signals. Thus, although the instrument is capable of functioning in the absence of a control computer, its operation can be conveniently monitored and modified by use of a digital computer.

6.2 Computer Hardware

6.2.1 Computer

The computer that was used in this research is an IBM PC which operates at the PC standard 4.77-MHz clock speed. This computer has

512 kilobytes (kb) of motherboard memory, one serial communication port (COM1), and one parallel printer port (LPT1). A commercial Everex Magic Card (Everex Systems, Inc.) was installed which has 6 rows for 64 kb address-seclectable random access memory (RAM) chips which give up to 384 kb RAM expansion, 1 parallel printer port (LPT2), and 1 serial asynchronous port (COM2). In addition, there are two 360 kb floppy disk drives for program and data storage. A Hercules graphics card is also installed to display graphics.

6.2.2 MetraByte DASH-16 Data Acquisition and Control Board

A MetraByte Corporation DASH-16 data acquisition and control board was used as the main interface between the microcomputer and pulse generator synchronization and data detection systems. This board includes a 12-bit successive-approximation analog-to-digital convertor (ADC) with a 12-μs conversion time, giving a maximum throughput rate of 60 KHz in direct memory access (DMA) mode. A three-channel 8254 programmable interval timer provides trigger pulses for the analog to digital converter (ADC) at any rates from 250 KHz to 1 pulse/hr. Two channels are operated in a fixed divider configuration from an internal 1-MHz crystal clock. The third channel provides a gated 16-bit binary counter that can be used for event or pulse counting or delayed triggering, and in conjuction with the other channels for frequency and period measurements. In addition, the board includes 4 digital output lines, and 3 digital input lines. The various DASH-16 functions are controlled by writing to and reading from several control and status registers. These registers are all located relative to a base address which is set

through DIP switches on the DASH-16 board. The base address used in this research was 816 (330H).

6.2.3 Analog-to-Digital Converter

The signal that is to be converted by the ADC is selected by an on-board 8-to-1 channel multiplexer (MPX) whose output channel is sent to a sample and hold (S/H) circuit. The S/H holds the signal locked so that the ADC can perform its successive approximation conversion on a constant signal. In the current configuration, channel 0 is connected to the analog output of a current-to-voltage converter circuit. During the conversion, bit 7 of the DASH-16 status register, also called the end-of-conversion (EOC) flag, is held high. When the conversion is finished the EOC flag drops low indicating that data is available at the two ADC registers called offset 0 (Low byte), and offset 1 (High byte).

6.2.4 Programmable Interval Timer and Data Acquisition

Both the pulsed HCL and data acquisition circuits required an external pulse to initiate the signal of interest. In the former case, a 1-ms pulse is needed to fire the pulsed HCL, while in the latter a 0.1-ms pulse is used to trigger the DASH-16 ADC. In order to provide the most versatile pulses, a DASH-16 8254 Programmable Interval Timer (PIT) and electronic circuits are used as shown in Figure III.8.

The Intel 8254 programmable interval timer used in the DASH-16 consists of three independent 16-bit pre-settable down counters. Each counter can be programmed to divide by any interger in the range

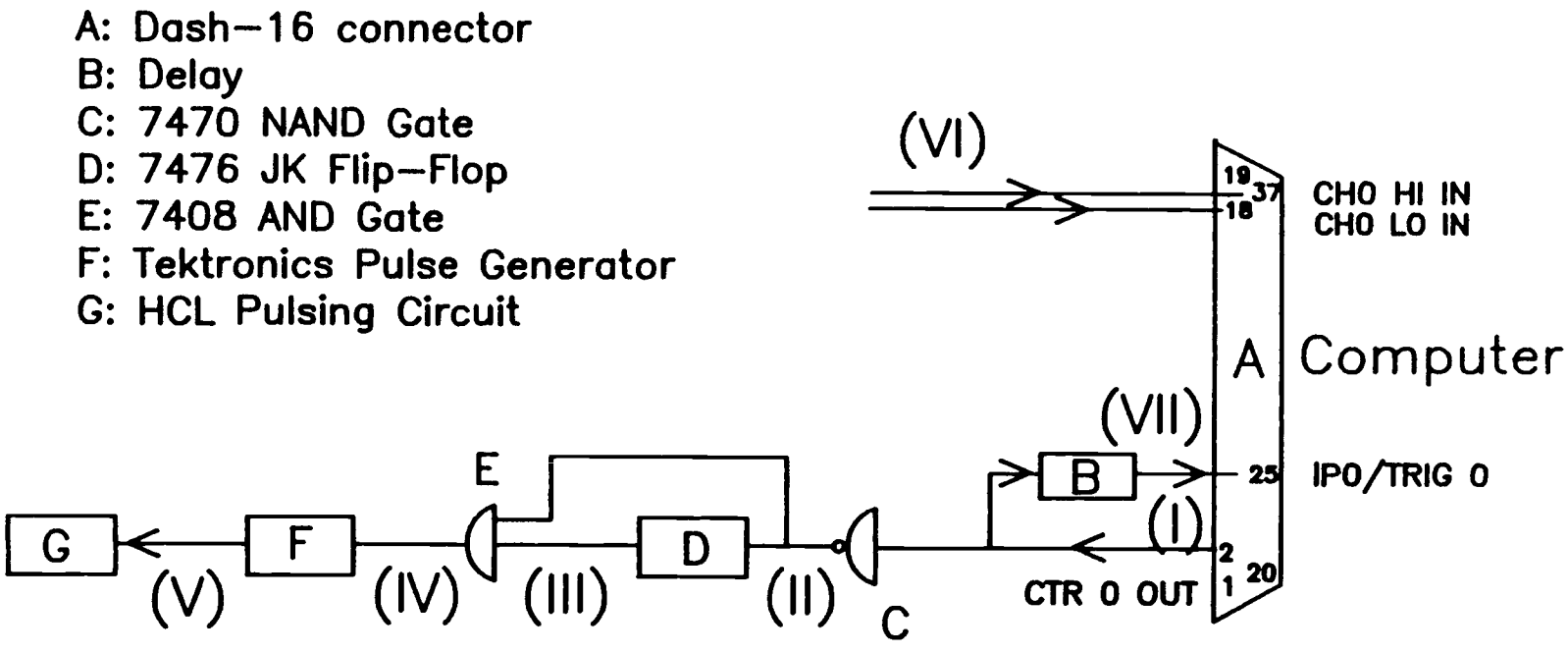

Figure III.8 Circuit diagram for the pulse generator that times the HCL pulses and data acquisition. Roman numerals refer to pulses shown in Figure III.9.

2 - 65,535. Counters 1 & 2 are cascaded and the input of counter 1 is connected to a 10-MHz crystal oscillator. The output of counter 1 is connected to the input of counter 2. Counter 0 is uncommitted and its input, output and gate control are available on the 37-pin "D" connector at COUNTER 0 IN (pin 21), COUNTER 0 OUT (pin 2) and IP2 (pin 24). The output of counter 0 is also connected to the input of IP0/Trig 0 (pin 25) which enables to trigger the DASH-16 ADC for data acquisition. Data from a current to voltage converter circuit are acquired by a channel #0 analog high input (pin 37) and a channel #0 analog low input (pin 18). By placing the 8254 PIT in mode 10 and mode 11, counter 0 is selected for a operation. This gives an output pulse with a width as short as 30 ns, which easily meets the requirements of this research. In this study, counter 0 is used to generate a 0.1-mS pulse width.

Figure III.9 is a timing diagram which illustrates the temporal relationship of the synchronization signals. A BASIC program controls counter 0 to produce an output pulse at pin 2 of the "D" connector. This pulse (I in Figure III.8) is first inverted by a 7470 NAND gate (C). The inverted pulse (II) is then fed into a 7476 J.K. Flip-Flop (D) and a 7408 AND gate (E), to produce a square wave (III). Pulse (III) is AND'ed with pulse (II) to produce a pulse (IV) that triggers a pulse generator (F, Tektronix type 114, Beaverton, OR) that drives the hollow cathode lamp high-voltage pulsing circuit (G). The counter 0 output pulse (I) is also fed into a delay (B) to trigger the ADC for data acquisition (VII) that begins on the rising edge of these pulses. For background emission correction, data are alternately acquired when the HCL is turned on and turned off.

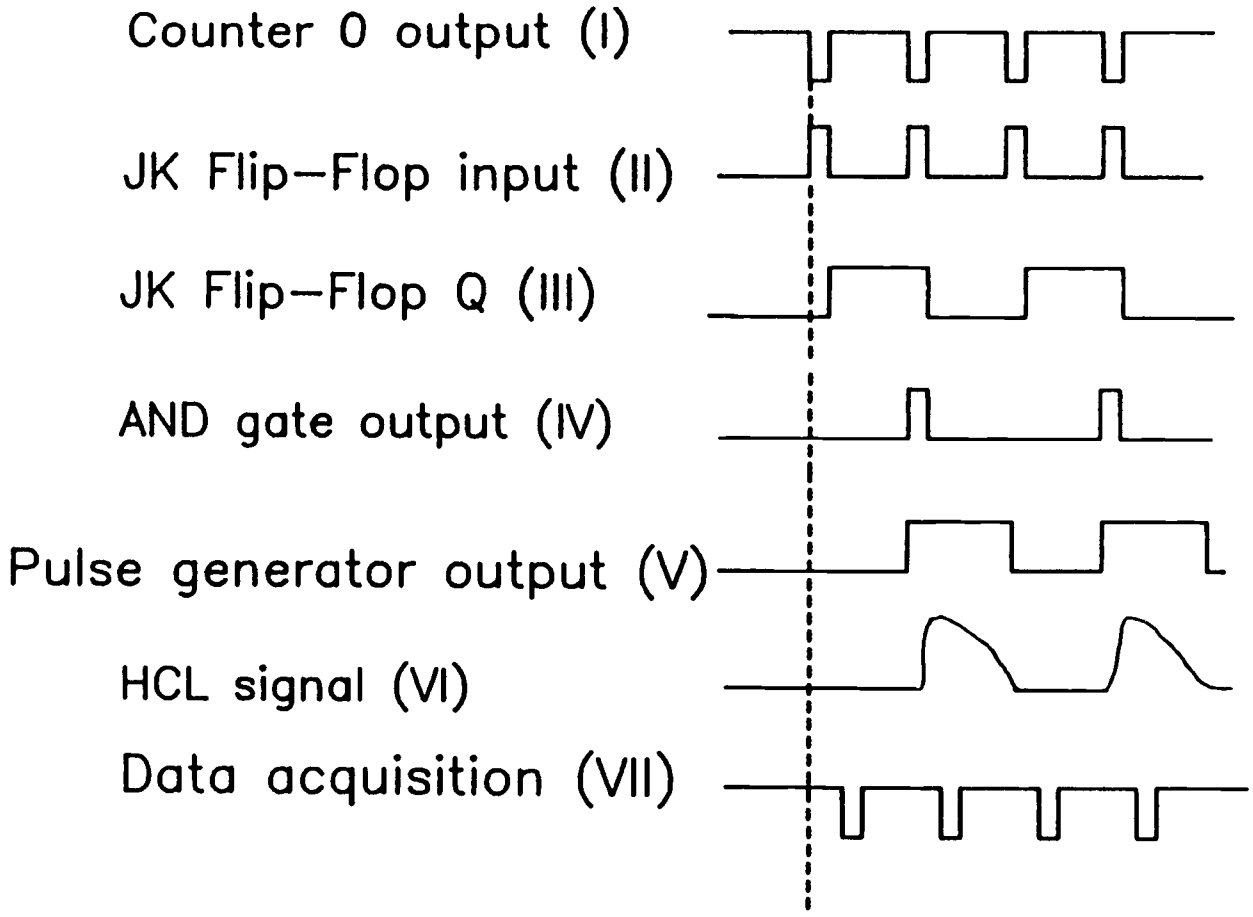

Figure III.9 Timing diagram for the HCL pulses and data acquisition.

7. Interface between an Atomsource and VG PlasmaQuad Mass Spectrometry

7.1 Ion Source

Figure III.10 shows a schematic of the gas-jet enhanced sputtering ion source (Atomsource) and its interface with the VG PlasmaQuad mass spectrometer. A quartz tube (12-mm I.D.) was used to guide the ions into the mass spectrometer. A mechanical pump that is ordinarily used to maintain a low pressure inside the ion source was not used for this study because the plasma was unstable due to competition between the ion source and mass spectrometer vacuum pumps. The vacuum in the expansion stage of the mass spectrometer was sufficient to maintain the required low pressure in the Atomsource. The operating pressure of the ion source was maintained by controlling the Ar gas flow rate into the source with a mass flow controller (Sierra Instrument, Carmel Valley, California).

A series of up to three variable 400-V, 100-mA Heath power supplies (Heath Instruments, Benton Harbor, MI) was used as an external power supply for the sputtering current (for reasons which will be discussed later in this section).

The sampling cone was connected to ground potential. In order to bias the anode positively against the sampling cone, an additional power supply (Heath Instruments, Benton Harbor, MI) was used.

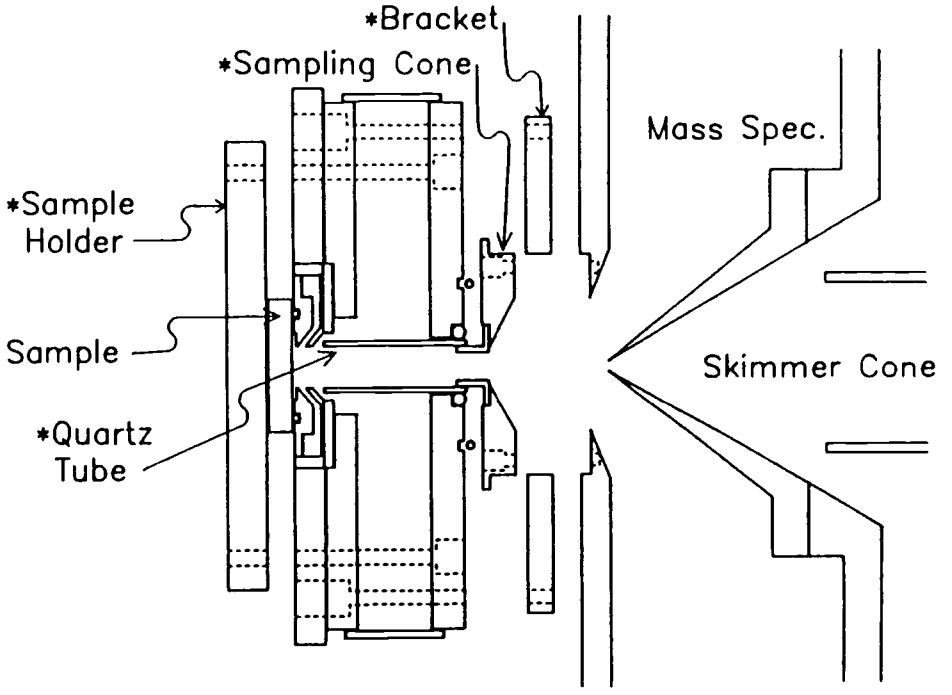

Figure III.10 Schematic diagram of the gas-jet enhanced sputtering ion source and its interface with the VG PlasmaQuad mass spectrometry.

7.2 Power Supply

After constructing a mount and an interface between the six-jet Atomsource and the mass spectrometer, the spectrum of a Zirconium standard (X-866) was obtained. The highest peak is Ar (40) and the Zr (90) peak is barely visible on this scale. Unexpectedly strong Ni (58) and Ni (60) peaks were obtained, which were attributed to sputtering of the original Ni sampling cone ordinary used with the ICP. Various types of sampling cones and interfaces were constructed to avoid such etching of the sampling cone. However, geometric modification failed to completely solve this problem because both the sample and the sampling cone were connected to the ground potential and the Ar ions attacked both. This problem was solved by using a different power supply configuration in which the anode was connected to the ground potential and the cathode (sample) was connected to a negative potential. In the case of the original Atomsource power supply, the anode is connected to the positive potential and the cathode is connected to the ground potential. The resulting mass spectra showed an increase in Zr peaks by a factor of 10000 and no Ni peaks from the cone material, indicating that this problem was solved.

7.3 Sampling Zone Distance and Sampling Cone Hole Size

The sampling distance between the cathode surface and the sampling cone exit aperture is an important variable. Jakubowski et

al. [105] investigated the dependence of ion intensities on the sampling distance. The intensities of the molecular ions show a rapid decrease with decreasing sampling distance, whereas the intensities of the analyte ions show an exponential increase. They also noted that further decreases in the sampling distance appears to be advantageous, but subsequently leads to depression of the extracted ion current as deposition of the sputtered material begins to clog the exit aperture. Therefore, to generate strong ion signals, but also reduce the possibility of clogging the exit aperture, it was necessary to compromise the sampling distance. To decrease the sampling distance, a flat plate with a 5-mm I.D. aperture was designed to replace the ordinary sampling cone. This also reduced the sampling distance as far as possible without redesigning the main housing of the Atomsource.

The sampling cone hole size affected the pressure gradient between the Atomsource and the inside of the mass spectrometer, and affected the efficiency of the extraction of analyte ions into the mass spectrometer.

7.4 Mass Spectrometer

A VG PlasmaQuad mass spectrometer (VG Elemental, Great Britain) was used for this study and a schematic of its main components is shown in Figure III.11. Different parts of the spectrometer are held at different pressures to assure correct operation of the plasma sampling interface and the quadrupole mass spectrometer. In order to

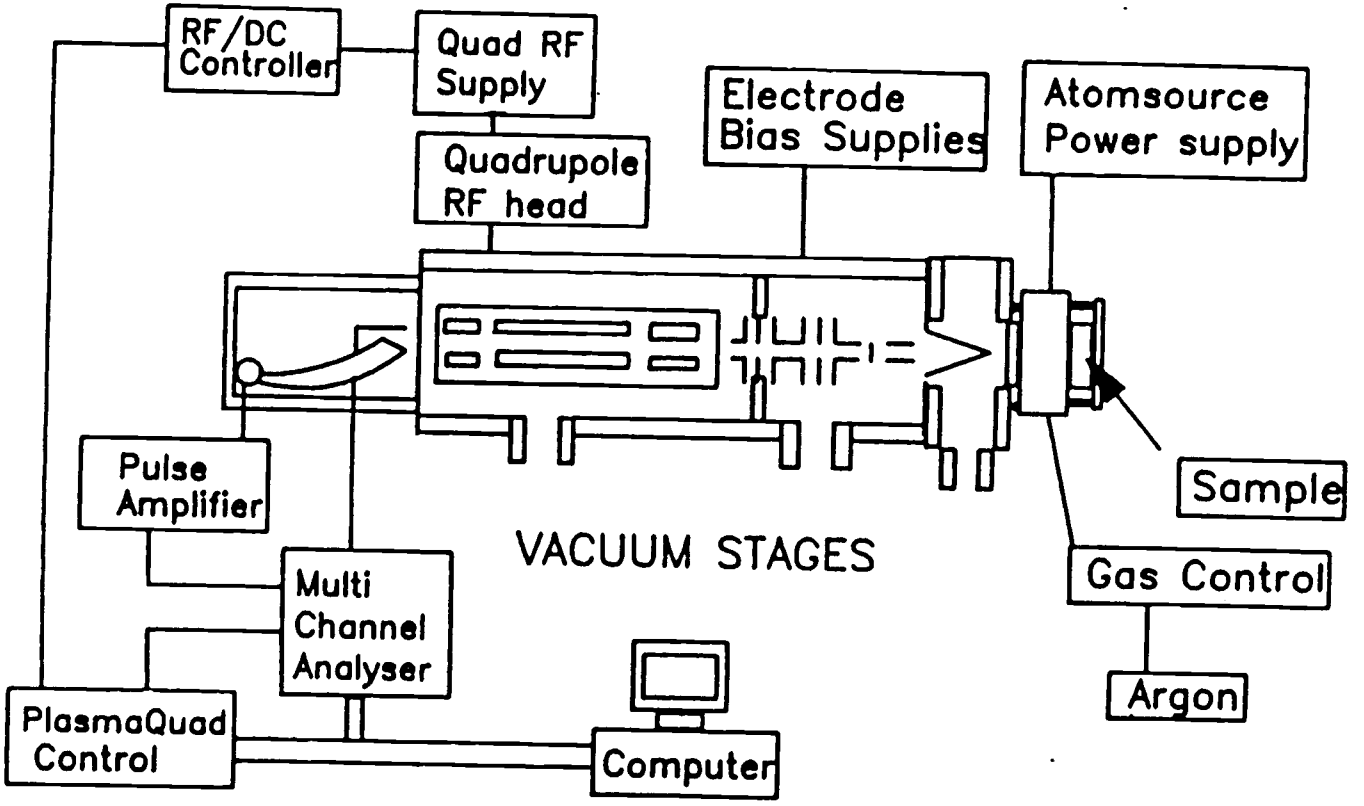

Figure III.11 Schematic diagram of the VG PlasmaQuad mass spectrometer (VG Elemental, Great Britain).

maintain these pressures, a combination of rotary and diffusion pumps are used.

The interface between the gas-jet enhanced ion source and the mass spectrometer was composed of two cones: a special sampling cone and the original skimmer cone.

This sophisticated commercial quadrupole mass spectrometry transmits ions of the selected charge to mass ratio. This is followed by an ion detection system, consisting of a channel electron multiplier (CEM) operated in an ion counting mode and followed by a suitable amplifier and discriminator, which measures the number of ions arriving and displays this data in a number of ways. Pulses from the detection system are fed to a microprocessor-controlled data acquisition unit (a multichannel scaler), which also controls most of the other aspects of the instrument through an IEEE-488 interface.

8. Experimental

8.1 Samples

Three zirconium standards (x-863, x-865, and x-866), one zircaloy standard (x-868), and one zircaloy sample, provided by Wah Chang Albany (Albany, OR), were used in this study. Their compositions were determined by ICP-MS and other suitable methods.

The samples were machined and polished on one side to obtain a flat surface. These samples were then surface cleaned by rinses in ethanol, dilute HNO_3, and deionized-distilled water. A preburning

time provided a clean sample surface and a condition of equilibrium.

8.2 Analytical Procedure

In the ICP-MS experiment, 0.25 g of zircaloy sample were dissolved in 25 ml of acid (2:1:40, $HF:HNO_3:H_2O$) and a calibration standard solution containing several 0.1 μg/ml mono-isotopic elements (^{27}Al, ^{45}Sc, ^{55}Mn, ^{59}Co, ^{89}Y, ^{103}Rh, ^{139}La, ^{141}Pr, ^{169}Tm, ^{209}Bi) was also prepared for mass discrimination correction. The 1 percent sample solution, the calibration solution, and the blank solution were mixed with 0.5 μg/ml ^{233}U to establish an internal standard. Each of the solutions was then mixed with 9 ml of deionized-distilled water, reaching a total dilution factor of 1,000.

IV. FUNDAMENTAL STUDIES OF A GAS-JET ENHANCED SPUTTERING SYSTEM FOR ATOMIC SPECTROSCOPY

by

Hyo J. Kim and Edward H. Piepmeier

Department of Chemistry

Oregon State University

Corvallis, OR 97331

For submission to Analytical Chemistry.

Brief

The use of a gas jet increases the sampling rate in a glow discharge source. The reasons for this increase are elucidated by studies of the electrical characteristics of the discharge, by spatially resolved atomic absorption and emission observations and by electron microscopic studies.

1. Abstract

The use of gas jets in a sputtering cell makes this direct sampling method practical for atomic absorption spectrophotometry determinations. With a single-jet glow discharge source, the gas jet increases absorbance by a factor of 40. An additional increase in absorbance by a factor of 5 is obtained with time resolved observations when the jet flow is suddenly turned on. With a commercial six-jet sampling cell that directly atomizes solid samples for conventional atomic absorption spectrophotometers, the sample loss rate for a Cu sample is 400 μg/min with a 0.2-L/min gas flow rate and 170 μg/min with no gas flow. The absorbance for a Cu sample is 1.56 with a 0.2-L/min gas flow rate and 0.14 with no gas flow. Studies of the electrical and spectral characteristics of this six-jet Atomsource and a similar single-jet glow discharge source have been made to help determine the mechanism of the increased sampling rate. A scanning electron microscope is used to investigate the effect of experimental parameters such as current density, sputter time, gas flow rate and cathode base material on the microstructure of the cathode surface.

2. Introduction

Atomic spectrometric methods of chemical analysis are often

limited by the necessity to dissolve solid samples before atomization. The technique of cathodic sputtering in a glow discharge has previously been used in the analysis of samples by absorption [112-122], emission [123-141], fluorescence [142-147] and mass spectrometry [148-153]. Cathodic sputtering has also been used in more fundamental spectroscopic investigations [154-167]. A scanning electron microscope has been used to study the microstructure arising on the cathode surface with various experimental conditions during ionic bombardment [168-170].

The basic idea of the direct analysis of solids with sputtering in a glow discharge is to expose a conductive solid to sputtering by ion bombardment and observe the resulting sputtered atoms spectroscopically. Thus, a simple sputtering chamber can be attached to a conventional atomic absorption spectrophotometer in the place of a flame atomizer. For atomic absorption measurements, it is desirable to design a sputtering chamber to have the maximum number of ground-state atoms in the optical path and to minimize emission. Therefore cells are usually designed to observe the atom cloud some distance away from the glowing discharge region near the cathode.

Following a suggestion by Russell and Walsh [112], Gatehouse and Walsh [113] in 1960 reported the use of cathodic sputtering to directly atomize a solid sample for atomic absorption analysis. Gough [116] improved direct solid atomic absorption analysis by using a flowing gas cell instead of a static cell, and compensated for background absorption, which possibly was caused by the aggregation of the sputtered atoms or particles, with a dual-modulation amplifier. The gas entered the chamber with a high velocity through

a hollow annulus located 0.5 mm above the surface. After entering in a direction parallel to the sample surface, the gas turned away from the sample towards the body of the chamber. The sputtered atoms that had diffused from the sample surface into the path of the gas were swept into the body of the chamber where they were observed. In this way diffusion losses to the chamber walls were reduced, transport of atoms to the observation region improved, and the absorption signal increased.

A newly developed atomizer called the Atomsource (Analyte Corporation, Grants Pass, Oregon) uses six high-velocity gas jets [171] that are pointed at and impinge upon the sample surface. (This is in contrast to Gough [119] where the gas enters parallel to and 0.5 mm above the surface.) The high velocity gas jets not only change the visual and electrical characteristics of the discharge, but also increase the amount of material atomized, as is apparent from the craters that are produced in the sample where the jets strike the surface. The high velocity gas flow produced by the jets follows a path that rapidly moves the sputtered atoms into the center of the cell, away from the sample surface and the walls of the chamber. This helps to minimize the loss of atoms that would occur by deposition onto the walls of the chamber and redeposition back onto the sample. The gas flow then moves the sputtered atoms quickly into the long observation path.

This paper reports the increasing sample loss rate and absorbance produced by the use of gas jets, and investigates possible reasons for the increases with the help of data from the Atomsource

and a modified single jet glow discharge source, and scanning electron micrographs of the sputtered surfaces.

3. Experimental Section

3.1 Design of a Six-jet Glow Discharge Source

The six-jet atom source consists of three separate components, a solid sample atomizer, an operator input/output box, and a control unit. The solid sample atomizer shown schematically in Figure IV.1 consists of a Delrin chamber that is internally 17.2 cm long and 3.8 cm in diameter with demountable quartz windows at each end. A water cooled copper cathode plate on the side of the chamber helps to stabilize the sample temperature during the analysis. The flat sample is sealed over a 0.8-cm diameter hole in the cathode plate with an o-ring Any piece of metal or alloy with a 1" (2.5-cm) minimum flat surface may be analyzed directly. The six jet nozzles are located 1 mm from the front of the sample and pointed so that high velocity jets of gas are directed towards the center and at an angle against the sample surface.

The operator input/output box is controlled by a keyboard which provides for data entry and start-stop functions. An LCD display and audio signal give the operator system feedback.

The system program is stored in Erasable Programmable Read-Only Memory (EPROM). All operator programmable variables used to control the atomization parameters are stored in non-volatile memory while

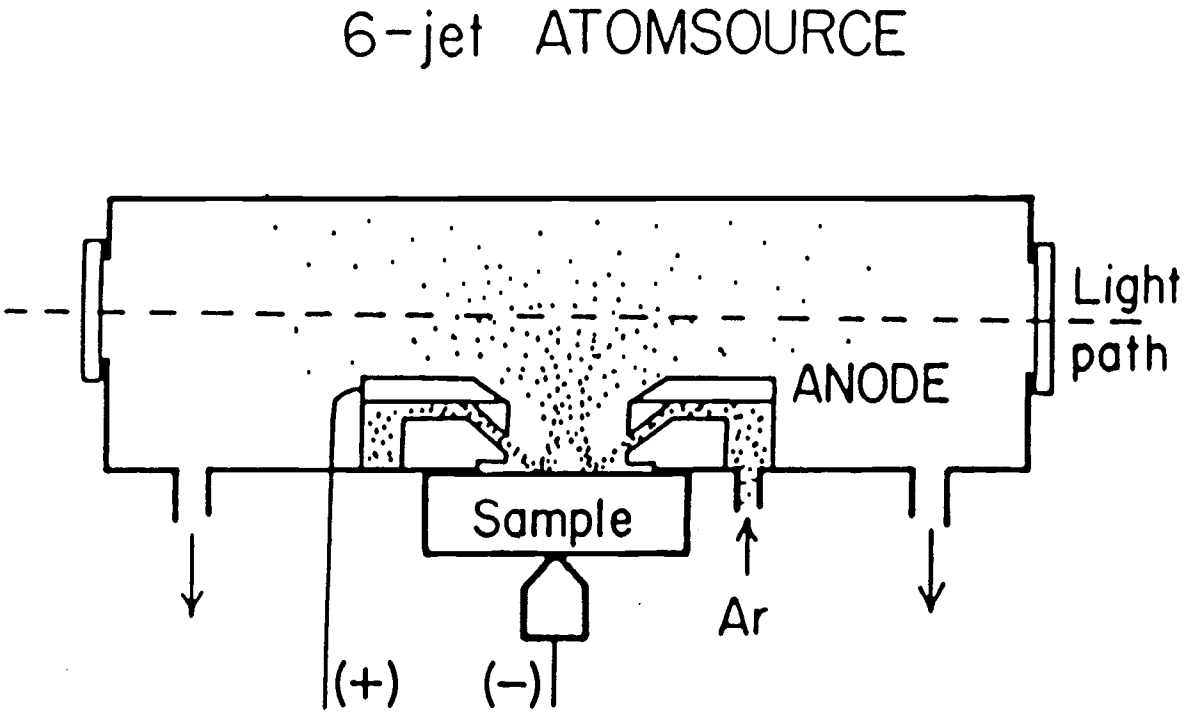

Figure IV.1 Side view schematic of six-jet Atomsource sputtering atomizer.

other program variables are stored in Random Access Memory (RAM). An RS-232 port has been provided to allow for interfacing to a modem, printer, or communication with another system. The CPU monitors and controls the atomization process utilizing signals from sensors, including positive pressure, partial pressure, emission intensity, cathode plate temperature, control unit temperature, atomizer supply current and voltage, low voltage supplies and line voltage. A closed loop servo is used to control pressure in the atomizer. A pressure sensor provides feedback to the servo amplifier which then adjusts a motor-controlled valve in the flowing gas system to maintain constant atomizer pressure. Between runs the atomizer is maintained at a positive pressure. A mass flowmeter (Sierra Instrument, Carmel Valley, California) with a micrometer valve was added to the gas inlet so that pressure and flow rate could be set independently.

The Atomsource system can be installed on any conventional atomic absorption spectrophotometer in place of a flame atomizer. All parameters affecting the sputter discharge such as discharge current, discharge voltage, pressure, and sputter times are controlled by a microprocessor. All operator-programmable variables, including sputter times, regulation modes, gas pressures, and voltage or current levels, are stored in nonvolatile memory.

3.2 Single-jet Glow Discharge Source

Figure IV.2 is a schematic diagram of the single-jet glow discharge source designed to study the flow effect on sputtering.

The body of the cell is made of Delrin with two quartz windows

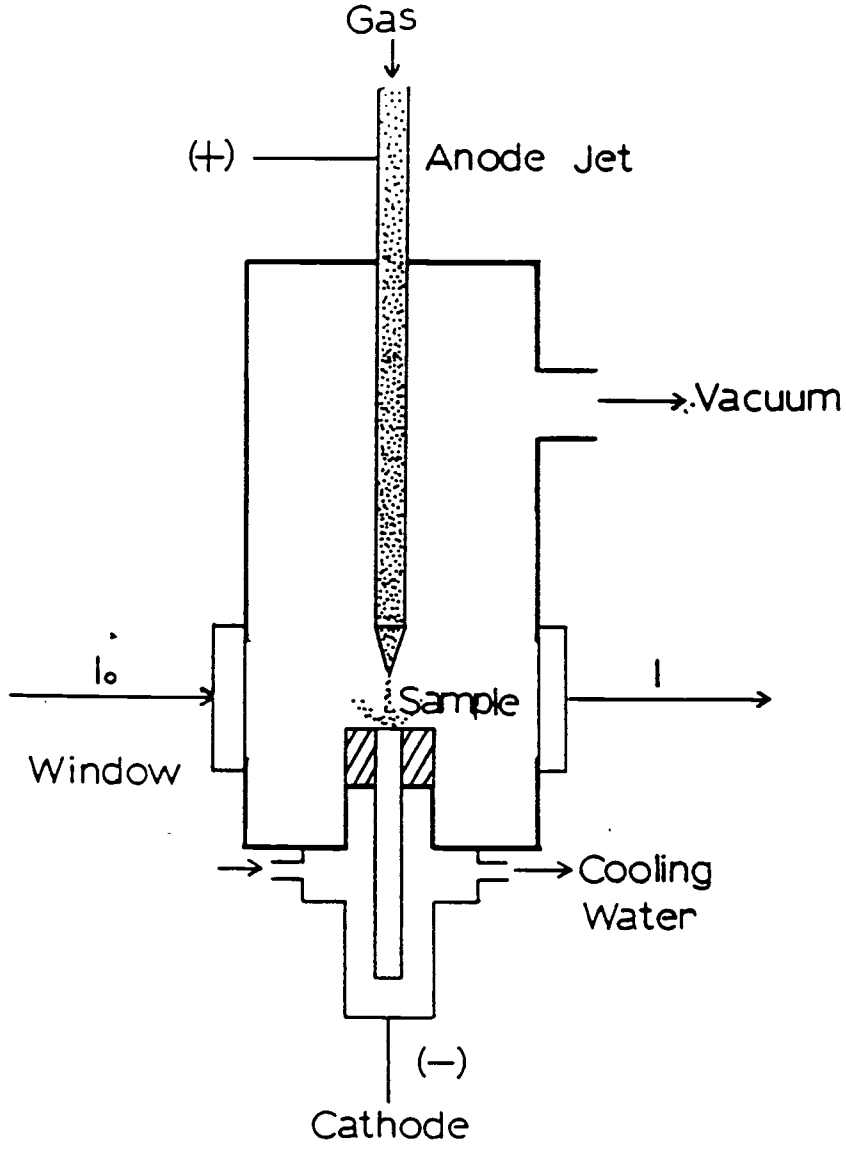

Figure IV.2 Schematic of single-jet glow discharge source. Sample diameter is 0.5 cm.

(O.D.=1.5 cm) to provide an optical path for the absorbance measurements. An exhaust port to a vacuum pump and a control valve are used for initial evacuation and to maintain a low pressure (1 to 10 torr). The cathode is a demountable copper rod 0.5 cm in diameter and attached to a water-cooled support. Teflon tape is used to insulate and shield the cathode and support.

The anode is a brass tube of 0.5 cm O.D. with a detachable single jet nozzle of 200 μm I.D. located above the cathode. The distance between the cathode and anode can be adjusted with a micrometer. The gas flow rate is monitored accurately by a thermal-mass flowmeter.

3.3 Optical System

Both the single-jet and six-jet Atomsource were mounted on a vertically and transversely adjustable stage in the sample beam path between the hollow cathode lamp and a Heath EUW-700 0.35-m Cerny-Turner grating monochromator (Heath Instruments, Benton Harbor, MI). The f/6.8, 35-cm monochromator employs a 48-mm square plane grating (blazed for 200 nm) with 1180 lines/mm, giving it a reciprocal linear dispersion of 2 nm/mm in the first order. A RCA C31034 end-on photomultiplier tube was used as the optical transducer.

A copper hollow cathode lamp (Westinghouse, No. WL23042) with a 5-mA lamp current was used for the atomic absorption spectral line source. A mechanical chopper was used in front of the lamp for rejecting the background emission.

The emission from the hollow cathode lamp is focused onto the

discharge cell with a 25-mm diameter symmetric convex spherical silica lens. The nominal focal length of this f/6.0 lens is 150 mm. Emission from the discharge cell and hollow cathode lamp is transferred to the monochromator with two 51-mm diameter parabolic, uv-enhanced aluminum first-surface, 350-mm focal length mirrors in an over-and-under configuration.

The current from the photomultiplier tube is converted to a voltage by a current to voltage converter operational amplifier circuit with a 0.001-s RC time constant in the feedback loop. The voltage is converted to a digital form with a DASH-16 analog to digital input/output expansion board (Metrabyte, Taunton, MA) and stored in an IBM-PC computer.

3.4 Sample Loss Rate

Thin oxygen-free copper sheets, 25 x 25 mm in area and 0.25 mm thick, were sputtered and the amount lost was determined by weighing on an analytical balance. The sputtering time was chosen to ensure a sufficient loss in mass to minimize the weighing error. Various combinations of current density, voltage, gas flow rate, and sputter time were used. The net exposed area for the six-jet Atomsource was circular and 0.8 cm in diameter, and the area that is directly influenced by the six gas jets is approximately 0.2 cm^2.

3.5 Atomic Absorption and Emission

A sputtering chamber mounting stage was constructed for

positioning the stage horizontally and vertically relative to the fixed light path between the hollow cathode spectral line source and the monochromator. The plane cathode surface was vertical and parallel with the monochromator slit when spatially resolved absorbance was measured. The monochromator slit width was 100 μm and the slit height was 1.0 cm. The distance from the cathode could be varied by moving the sputtering chamber across the fixed light path. The closest approach to the cathode surface was limited to 1 cm by the construction of the six-jet Atomsource.

3.6 Scanning Electron Microscope

A model S-570 scanning electron microscope (Hitachi, Tokyo, Japan) was used for examination of the cathode surface. The SEM was operated in the secondary electron mode with a 20-kV accelerating voltage for the electron beam and 30° for the tilt angle of examination. The copper specimens were cleaned with acetone to remove surface contamination before examination.

4. Results and Discussion

4.1 Voltage-Current Density Characteristics

Voltage-current density characteristics curves for copper at 5-torr pressure in a single jet glow discharge source are shown in Figure IV.3 for no gas flow and 0.2 L/min gas flow. The gas flow

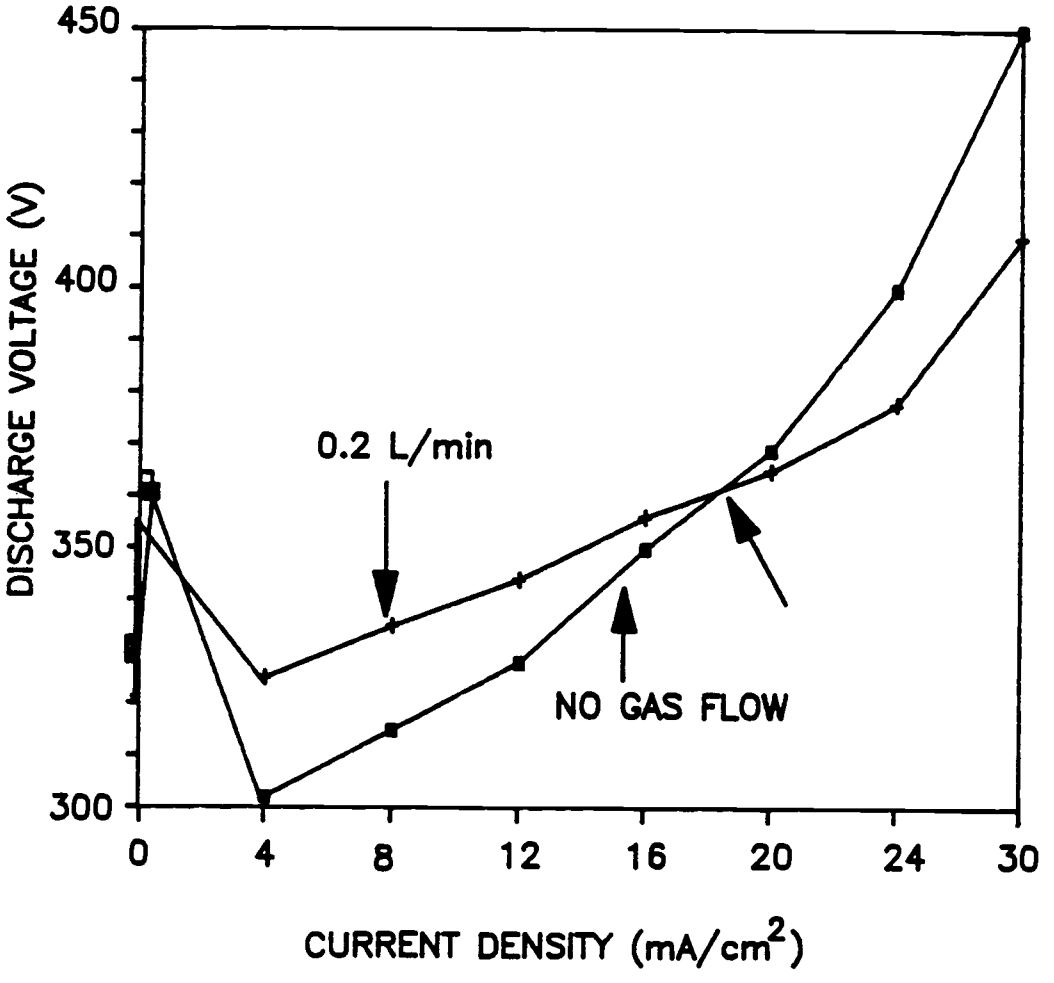

Figure IV.3 Voltage-current density characteristic curves for copper at 5-torr pressure in a single-jet glow discharge source: (■) no gas flow; (+) 0.2 L/min.

rate at a given pressure was adjusted by changing both the pumping speed and the mass flowmeter control. The voltage-current density characteristic curve can be divided up into three different regions. The first is the ignition voltage, the second is a region where the sample surface may not yet be totally covered by the discharge (this is uncertain because this normal glow condition was difficult to judge), and the last stage is the region where the surface is clearly fully covered by the discharge. The sputtering rate is most significant in the latter region (abnormal glow region).

The ignition voltage decreases with increased gas flow rate. This is not expected since the jet creates a local high pressure region and in static systems the ignition voltage increases with increasing pressure. It may be that the gas jets help to clean the cathode surface so that the ignition transition from a Townsend discharge to a normal glow discharge occurs at a lower potential. Or it may be that the gas flow produces a variation of the electrical field pattern and/or enhances the chain reaction mechanisms that occur during ignition.

Figure IV.3 shows a crossover point between the curves for the gas flow and the static state. At lower current densities, a higher voltage is needed to keep the same current density with the gas jets on, possibly because the gas jets blow the plasma around the sample surface and make it more difficult to sustain the current than in the static state, or the jet is not part of the plasma core and therefore tends to quench the plasma. After the crossover point, a lower voltage is needed to keep the same current density with the gas jet turned on. It may be that an increase in pressure requires a

decrease in potential to maintain the same current density because a gas jet provides a locally high pressure column between cathode and anode; higher pressures require lower cell voltage. Other reasons may be that the gas flow produces a variation of the electrical field pattern, or a gas environment that is freer of impurities.

4.2 Visual Observations

When the jet nozzle is the anode, a column of bright glow extends from the anode to the cathode and a relatively deep 0.5-mm diameter crater forms in the surface of the sample. However, when a separate anode located one cm off to one side is used, this brightly glowing column is not observed and the crater is wider (3 mm) and shallower. These results indicate that the sputtering ions are concentrated at the point of impact of the gas jet, especially when the jet is in the main part of the discharge. Clearly the gas jet influences the electrical characteristics of the discharge.

To further investigate the effect of a gas jet on sputtering, a thin copper sheet of 0.25-mm thickness was located on top of a bulk copper cathode in the single-jet atom source. The nozzle was the anode. During the early part of the discharge, the shape of the bright part of the plasma column became narrower towards the cathode sample surface. Upon continued sputtering a hole was sputtered through the metal sheet. The bright part of the plasma column near the cathode then became diffuse.

If the bright part of the jet indicates a high current density, then most of the current, or a large fraction of current, flows at

the point of contact of the jet with the sample surface. When the hole goes through the sample, the point of contact disappears and the current must contact the surface over a more diffuse area. This seems to be additional evidence that the jet causes the current to concentrate at the point where the jet strikes the surface of the sample.

The fact that the bright part of the jet becomes more pointed during the first part of the discharge may be the result of a distortion in the electric field around the edge of the crater that forms. Or it may be caused by a change in the gas flow pattern that occurs near the surface as the crater forms.

4.3 Sample Loss Rate

Figure IV.4 shows the Cu sample surface before (Figure 4a) and after the following experiments. At 60 mA/cm^2, 8 torr and no gas flow rate (Figure 4b), the Cu sample surface shows a round sputtered area where it is exposed to the discharge. However, at 60 mA/cm^2, 8 torr and 0.8 L/min gas flow rate (Figure 4c), the Cu sample surface shows six craters when gas jets are directed onto the sample surface. Gas jets clearly increase the sample loss rate and cause deeper, more representative sampling of the bulk material.

In a static system, von Hippel [172] calculated for a glow discharge at 0.1 Torr that 90% of the sputtered material diffused back to the cathode. In the gas jet system, the gas flow entrains the atoms and transports them away from the cathode more rapidly than

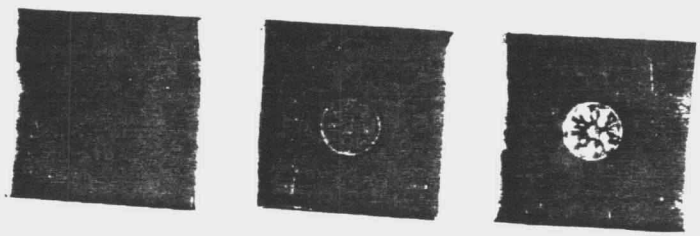

(a) (b) (c)

Figure IV.4 Photographs of Cu sample surfaces: a) unsputtered; b) at 60 mA/cm^2, 8 torr and no gas flow; c) at 60 mA/cm^2, 8 torr and 0.8 L/min.

they can diffuse back to the cathode, resulting in an increase in sampling.

More information about the jets and atom transport was obtained by using a brass sample that had a 4-mm diameter nonconducting lava rod pressed into a hole in the center of the brass. The surface was machined flat and sputtered. Where the gas jets struck the lava with high velocity, no brass was deposited. However, some of the brass material sputtered from the six craters was transported and deposited onto the lava along the edges of the jets where the gas velocity was low. This is additional evidence that the high velocity jet stream carries many atoms away from the surface before they have a chance to diffuse back and deposit onto the surface.

The sample loss was determined for 12 time intervals up to 40 min for 60 mA/cm^2 average current density, 8 torr pressure and 0.8 L/min gas flow rate. Current density is calculated by dividing the current by the circular area exposed to the discharge. An approximately linear relationship between the weight loss and the sputtering time was obtained. As an indication of precision, the relative standard deviation of the weight loss measurements for the 30-min sputtering time for 10 replicates was 7%.

Figure IV.5 shows the sample loss rate as a function of sputtering time calculated from the data. The sample loss rate significantly increases during the initial 3 min sputtering time and increases only slightly after 10 min sputtering time.

The average sample loss rate over 30 minutes as a function of current density was studied for three pressures. At 5 torr, the amount of sputtered material rapidly increases from 0.03 mg/min at 20

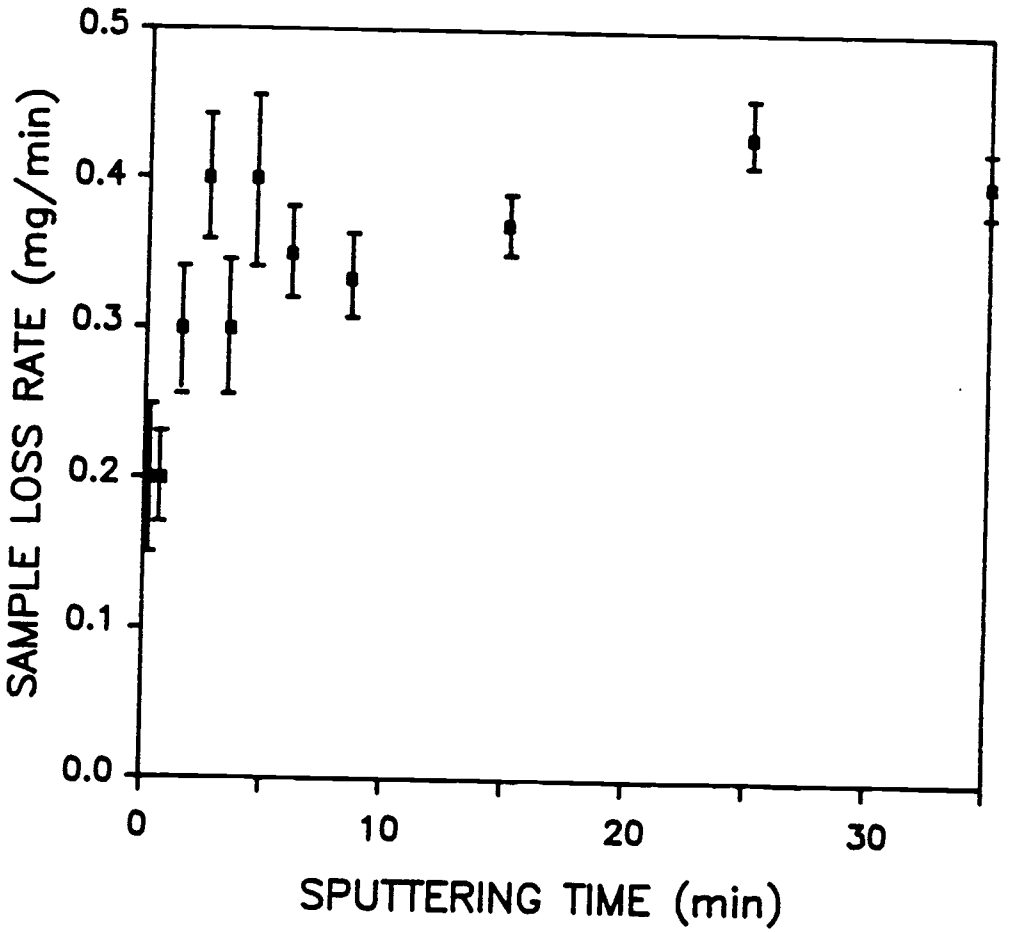

Figure IV.5 Sample loss rate vs. sputtering time for 60 mA/cm^2, 8 torr and 0.8 L/min.

mA/cm^2 to 0.90 mg/min at 60 mA/cm^2. Above 60 mA/cm^2, the sample loss rate cannot be obtained due to instrumental limitations. At 6 torr the average sample loss rate rapidly increases to 1.3 mg/min at 100 mA/cm^2, then dips to 0.90 mg/min at 120 mA/cm^2, and increases again to 1.3 mg/min at 140 mA/cm^2. A similar shape, including the dip at 120 mA/cm^2, is observed at 8 torr.

The cell voltage for 6 torr increases from 330 to 450 V as the current density increases from 20 to 80 mA/cm^2, but then increases only 20 V from 80 mA/cm^2 to 140 mA/cm^2. (There is no voltage dip at 120 mA/cm^2.) The cell voltage for 8 torr has a similar shape, concave down towards the current-density axis, beginning at 300 V at 20 mA/cm^2 and reaching 410 V at 140mA/cm^2.

The dip in the amount of material sputtered at 120mA/cm^2 may be explained as follows. As total current is increased, the jet regions eventually reach a current density saturation condition where it is necessary to significantly increase the voltage to increase the current density. However, when this occurs, instead of the voltage increasing as expected, the additional current may go to the jet-free regions. Then the same increment in voltage would produce a proportionally greater increase in current, as well as a decrease in sample loss rate. Additional evidence for this is the visual observation that the sputtered surface seems to be confined to the six craters below 60 mA/cm^2, while above 70 mA/cm^2, surface etching is obvious both within the six craters and in other areas.

Figure IV.6 shows the average sample loss rate for a 60-min sputtering time as a function of gas flow for three current densities. The number at each point is the cell voltage. The cell

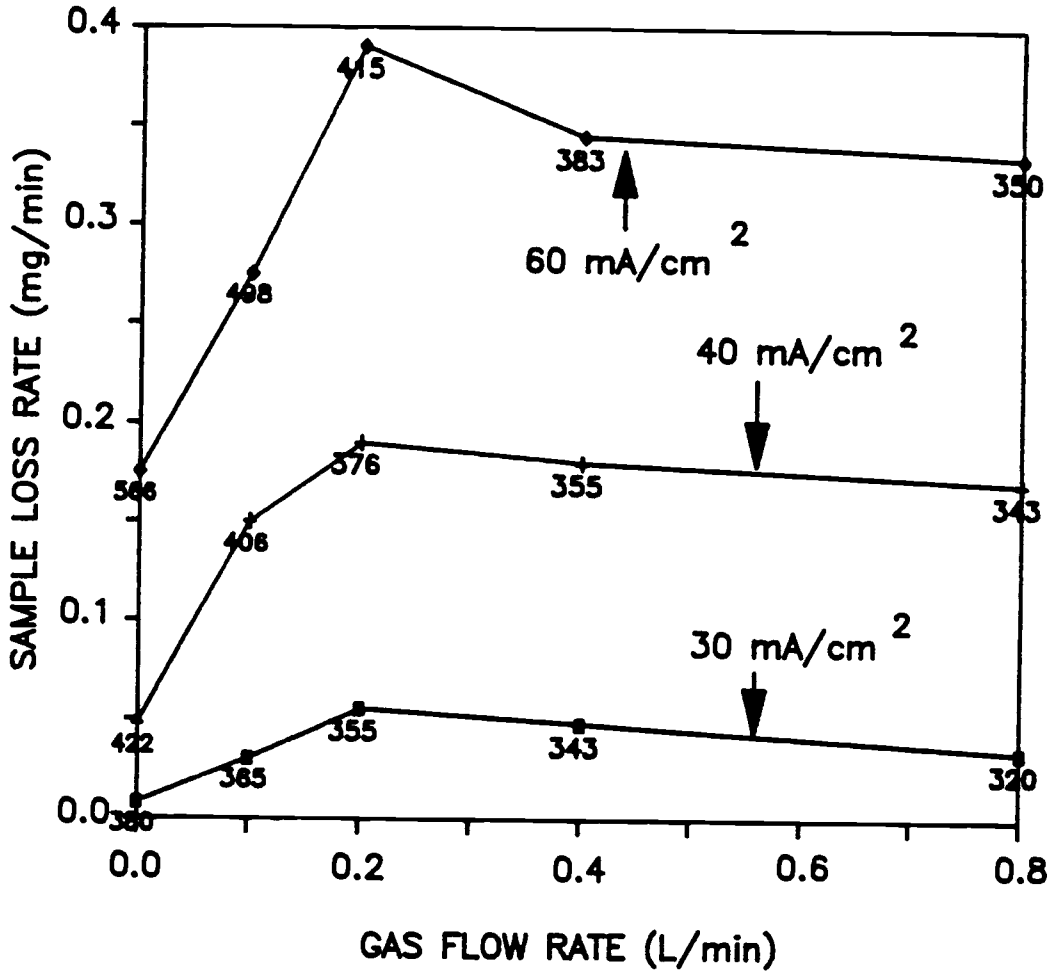

Figure IV.6 Average sample loss rate for 60 min sputter time vs. gas flow rate for three current densities. Numbers below each point are the cell voltage: (■) 30 mA/cm^2; (+) 40 mA/cm^2; (◆) 60 mA/cm^2.

voltages decrease with increased gas flow rate. As we hypothesized with the single-jet cell, this decrease may be caused by a higher local gas density, a cleaner gas environment, and/or by a change in electrical field patterns.

The sample loss rate initially increases and then decreases for all three current densities. As gas density increases, the sputtering rate ordinarily would decrease due to both a decreased mean free path near the cathode surface during which the sputtering ions gain energy, and a lower discharge voltage that provides the ions with energy. The initial increase in sample loss rate is in spite of the decreasing discharge voltage and increasing local gas density. If one of the main reasons for the increased sample loss rate were sweeping away of the sputtered material before it had a chance to redeposit on the sample surface, then the maxima in the curves at 0.2 L/min could be attributed to the sputtered atoms being swept away as fast as they are formed. A further increase in flow rate would produce no additional loss. As the voltage continues to drop and local gas density increases, the sputtering ions produce fewer atoms per ion and the sample loss rate drops.

Other causes for the shapes of the curves cannot be ruled out. The single-jet experiments showed how the gas jet can distort the plasma. If the gas flow increases the sputtering rate by increasing the electric field near the cathode, the initial rise in sample loss rate would be expected. Then the maximum might be explained by the jet flow pattern becoming broader or turbulent at the higher flow rates, diluting its influence. More information is needed to clarify the reasons for the shapes of these curves.

4.4 Atomic Absorption and Emission

Figure IV.7 shows the absorbance as a function of current with various gas flow rates in a single-jet glow discharge source. The current density at 30 mA total current is estimated to be 90 mA/cm^2. The absorbance increases with increasing current at all gas flow rates. The absorbance increases by a factor of 40 at 30 mA when the jet is on with a gas flow rate of 0.06 L/min.

Figure IV.8 shows a signal equal to the hollow cathode lamp emission plus emission from the cell as a function of data collection time when the gas flow is suddenly turned on in the single-jet glow discharge source. The total hollow cathode lamp emission is modulated by using a mechanical chopper to allow the hollow cathode emission to be distinguished from cell emission. The peak to peak magnitude of the square wave represents the hollow cathode emission signal intensity. The amplitude of the square wave would remain constant if there were no cell absorption. The gas flow is first turned off, the cell is pumped down to below 0.1 torr with the discharge on and then the gas flow is turned on. The pressure reaches a final value of 6 torr in about 20 s. The decrease in amplitude of the square wave shows that the absorbance increases to a peak value of 1.0 before settling to a steady value of 0.2. Therefore a further increase in the analytical signal by a factor of 5 is obtained by using this type of pulsing with time resolved observations.

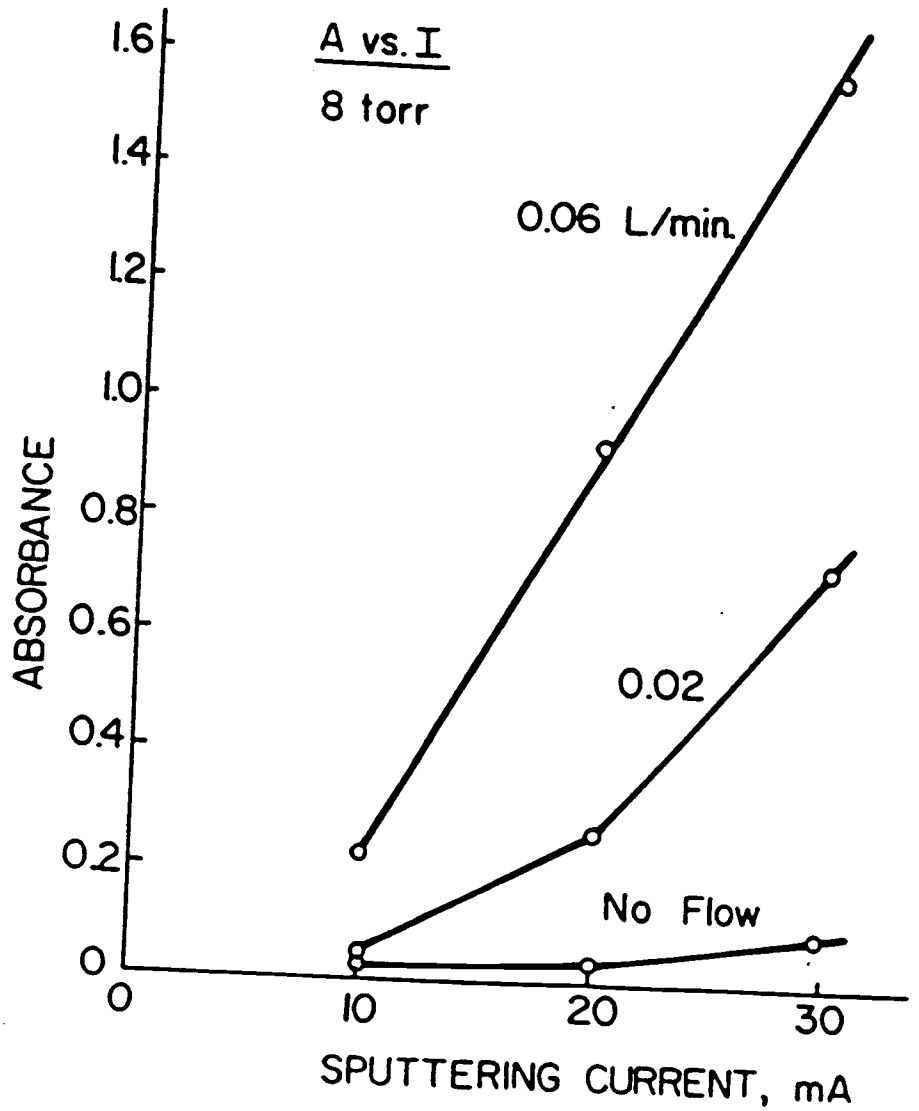

Figure IV.7 Absorbance vs. current with various gas flow rates in a single-jet glow discharge source.

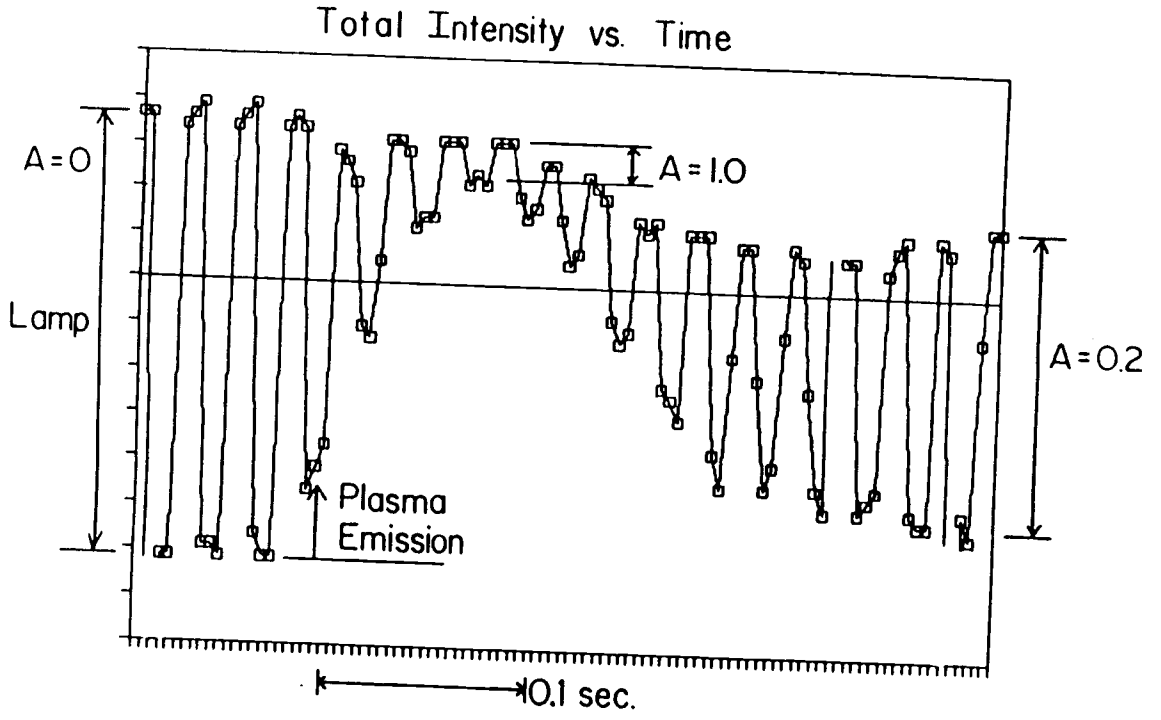

Figure IV.8 Total intensity of atom source plus transmitted modulated hollow cathode lamp intensity vs. data collection time for single-jet glow discharge source where the cell is pumped down and then the gas flow is suddenly turned on.

Figure IV.9 shows the steady state absorbance of Cu as a function of distance from the sample with various gas flow rates in a six-jet Atomsource. At lower gas flow rates, the absorbance decreases rapidly with distance as the flow rate decreases. At high enough flow rates the maximum absorbance is obtained in the center of the sputtering chamber (away from the sample) probably because the flow of the gas stream balances the rate of atom introduction into the observation zone with the losses to the walls of the sputtering chamber. Consequently, at the higher gas flow rates (0.8 L/min, 0.4 L/min, and 0.2 L/min), the absorbance does not change much with flow rate or as the distance from the sample increases. This would seem to be a good region for stable operation for highly precise measurements.

Figure IV.10 shows the relative emission intensity vs. distance from the sample for five gas flow rates. These observations are made outside the discharge region that occurs between the anode and cathode, and no further excitation of the sputtered atoms is expected to occur in this observation region. Compared to the absorption, the rapid decrease in emission intensity with increasing distance from the sample shows that the relative life time of the excited atom population is shorter than that of the ground state atom population. (The apparent emission intensity increase at 2.2 cm for 0.8 L/min gas flow rate may not be statistically significant since the RSD is 5 %.)

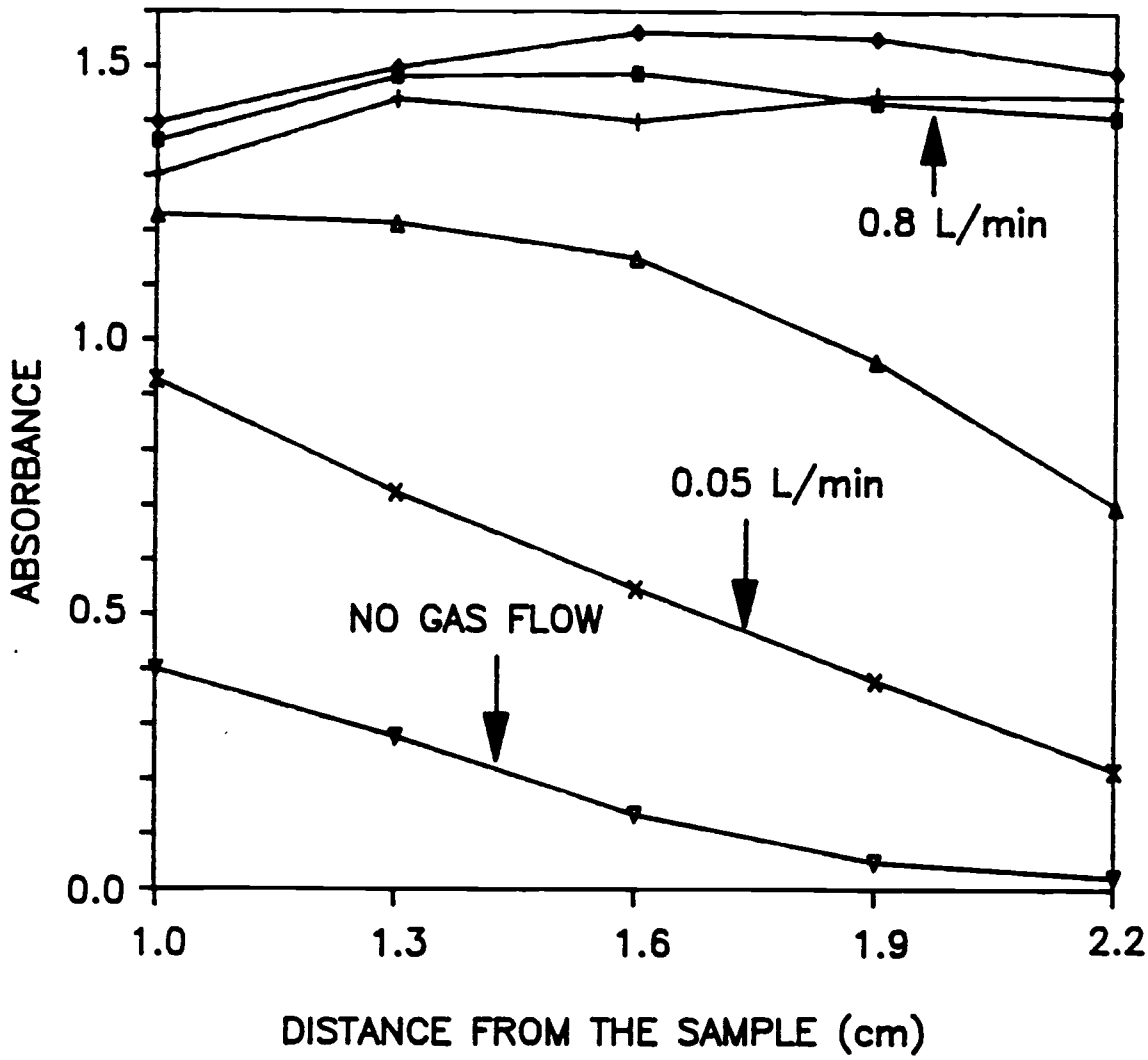

Figure IV.9 Absorbance vs. distance from the sample with various gas flow rates in a six-jet Atomsource: (■) 0.8 L/min; (+) 0.4 L/min; (◆) 0.2 L/min; (Δ) 0.1 L/min; (x) 0.05 L/min; (∇) no gas flow.

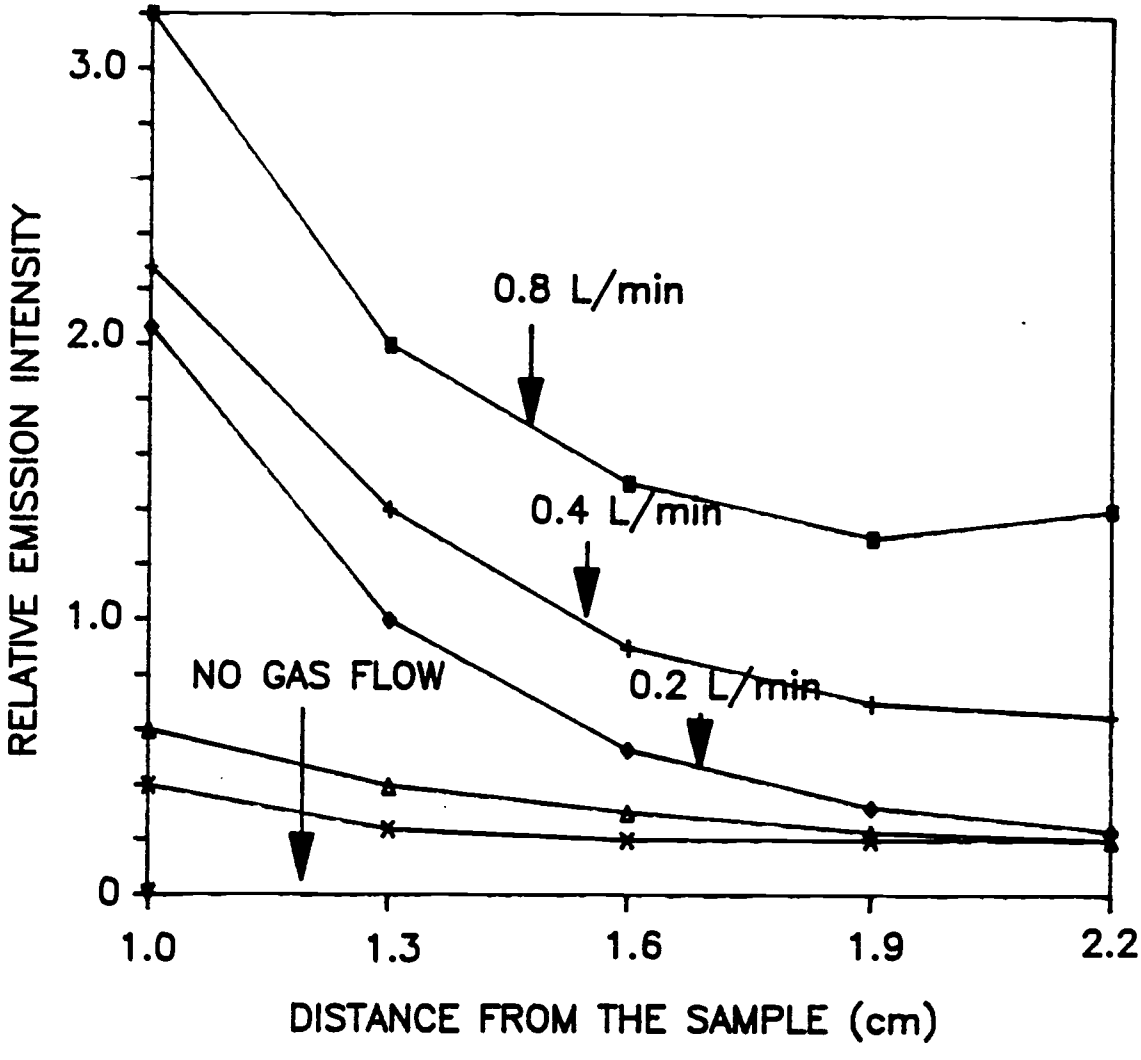

Figure IV.10 Relative emission intensity vs. distance from the sample with various gas flow rates in a six-jet Atomsource: (■) 0.8 L/min; (+) 0.4 L/min; (◆) 0.2 L/min; (Δ) 0.1 L/min; (x) 0.05 L/min; (▽) no gas flow.

4.5 Scanning Electron Microscope Observations

Various types of surface structure are formed as a result of different experimental sputtering conditions. Therefore an examination of the resulting surface features is important to a fundamental investigation of sputtering. More than 40 years ago, cone-like formations were reported [173] and with the subsequent availability of the scanning electron microscope (SEM), more investigators have examined the surface effects of ion sputtering [168-170,174-178]. The factors that affect the surface features include fill gas, cathode material, sputtered time, discharge current density, discharge voltage, gas pressure, and, in this study, gas flow rate.

4.5.1 Effect of Gas Flow Rate

As we saw earlier, the sample loss rate increases with increasing gas flow rate. To investigate the gas flow effect on the surface features, copper sheet was sputtered at 60 mA/cm^2 and 8 torr for 30 min with no flow and with a 0.8 L/min gas flow rate.

Figure IV.11 shows the sample surface observed at 490 and 200 magnifications with the SEM after sputtering without gas flow. The surface in Figure 11a shows crowded cone-like structures that are randomly distributed on the cathode material. Jager and Blum [168] speculated that these structures have lower sputtering yield than the rest of the cathode surface, thus acting to protect the underlying

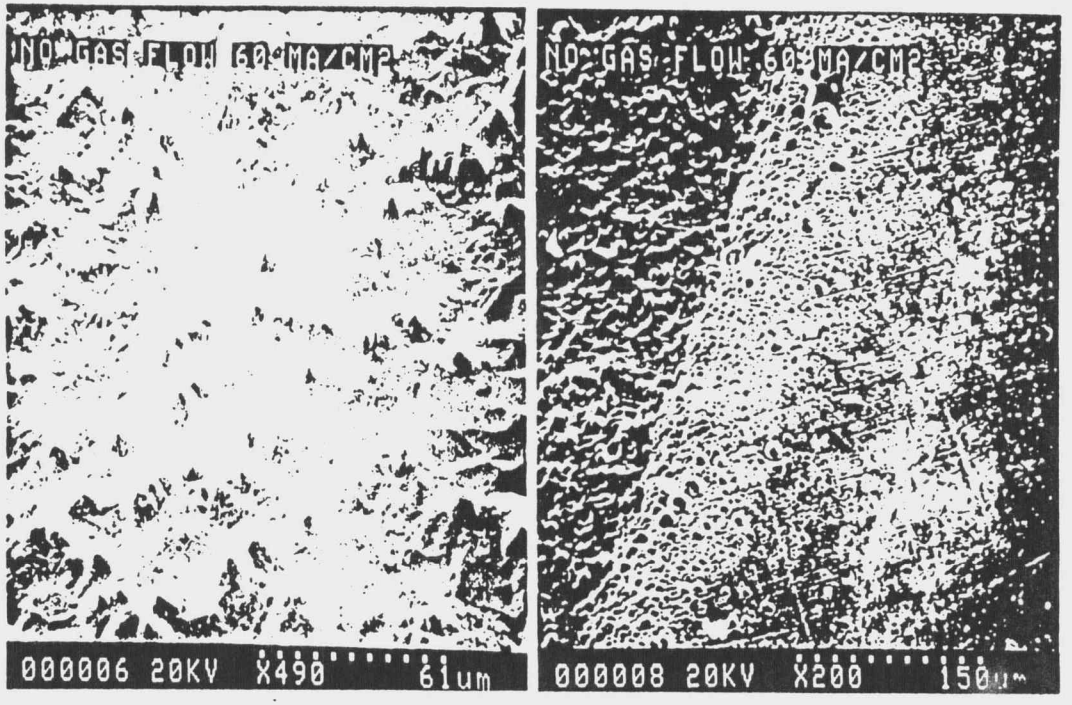

Figure IV.11 Effect of discharge for the Cu cathode with 60 mA/cm^2, 8 torr, 30 min sputter time and no gas flow: (a) inside of the discharge area, 500X; (b) border region between the inside of the discharge (left part) and outside of the discharge (right part), 200X.

material. The base of the cone will become lower and lower as long as the material of the inclusion remains on top of it; however, the cone will gradually be reduced in size after the removal of the inclusion because the bombardment is then no longer obstructed. Figure 11b shows the border area between the area which is exposed to the discharge, and the area which is shielded from the direct discharge by the cantilever lip shown in Figure 11a. Crowded cone shaped structures are present in the region exposed to the discharge and large flat areas are observed in the protected region.

Figure IV.12 shows the sample surface with 0.8 L/min gas flow rate. The region inside of the crater where the gas jets are directed onto the sample, Figure 12a, shows a flatter surface with hillocks but no pyramids like those that appear in Figure 12b outside of the crater. Therefore gas jets associated with high current density seem to prevent the formation of pyramids, or cause their erosion as we will see in the time resolved studies in the next section. For example, the jets cause a velocity component for sputtering ions that is parallel to the sample surface. Attacking the pyramids from the side may cause faster destruction if the tops of the pyramids contain protective impurities or structure. Jet sampling is therefore more uniform than ordinary glow discharge sputtering because the inclusions are not preferentially retained on the surface.

4.5.2 Effect of Discharge Current Density

The effect of increasing the current density on the sample loss rate is significant both because of the increase in the number of

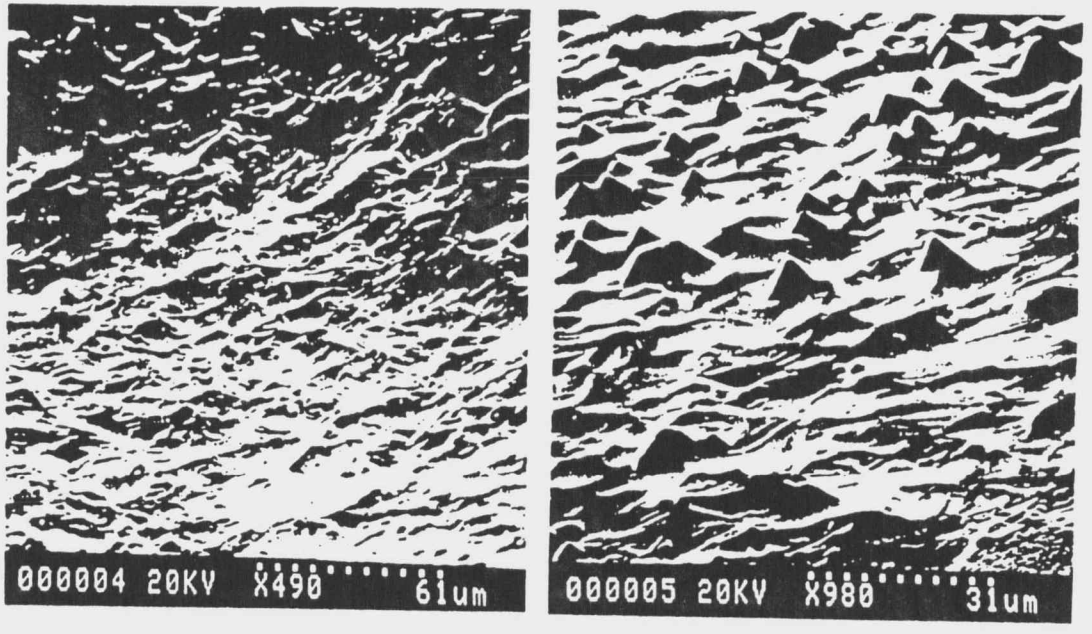

Figure IV.12 Effect of argon gas jets for a Cu cathode with 60 mA/cm^2, 8 torr, 0.8 L/min and 30 min, 500X: (a) inside of the crater; (b) outside of the crater.

ions bombarding the surface and the increase in the higher average accelerating potentials for the Ar ions caused by the concomitant increase in cell voltage. To investigate the effect of the discharge current on the surface structure, the discharge was run at 20 mA/cm^2, 60 mA/cm^2, 100 mA/cm^2, and 140 mA/cm^2 with 0.8 L/min gas flow rate and 10 min sputtering time.

The electron micrographs showed a surface with a number of scales without cones and hillocks at 20 mA/cm^2. The sputtering pattern might be different from others because at 20 mA/cm^2 the discharge may be in the normal glow region where the sample surface is not fully covered by current. At 60 mA/cm^2, the sample surface is relatively flat with hillocks, but without cones, where the gas flow directly strikes the surface. From 60 mA/cm^2 to 140 mA/cm^2, the sample surface shows no significant changes.

4.5.3 Net Sputter Time Effect

The sample loss rate significantly increases during the initial sputtering time and stabilizes after 3 min as we saw in Figure IV.5. Thus it is useful to investigate the surface generated for different sputtering times. Figure IV.13 shows the surface after various sputtered times with an argon gas flow rate of 0.8 L/min and 60 mA/cm^2 average discharge current density. After 5 s (Figure IV.13a) there are small holes and irregularities in the cathode surface where sputtering has occurred along grain boundaries or crystal dislocations. Many of the original surface scratches can also be seen. At 30 s (Figure IV.13b) the holes and irregularities become more numerous and small cones begin to appear. At 3 min

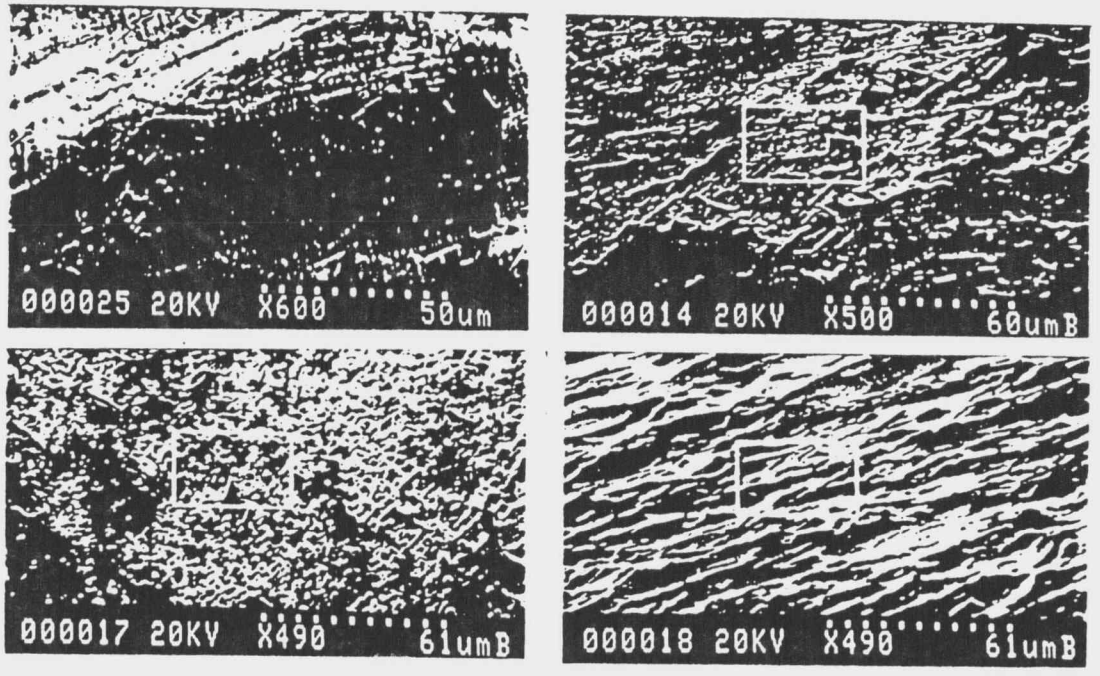

Figure IV.13 Effect of net argon sputter time, 500X, 60 mA/cm^2, 8 torr and 0.8 L/min: (a) 5 s; (b) 30 s; (c) 3 min; (d) 5 min.

(Figure IV.13c) the surface is crowded with small cones or pyramids. At 5 min (Figure IV.13d) the shapes of the cones disappear and hillocks are obvious. At 10 min (not shown) the hillocks are smaller and the surface is flatter. There is no significant change after 10 min. Therefore, comparing these results with the sample loss rates in Figure 5, it appears that a relatively steady-state sample loss rate is obtained after the removal of the grains or inclusions [171] which have lower sputtering yield than the rest of the surface. These results also indicate that the formation of the pyramids and cones is the result of surface imperfections that are not present in the bulk of the sample, since these structures are not present once the sputtering has proceeded into the bulk of the sample.

5. Conclusion

These studies show the way in which the sample loss rate for a glow discharge significantly increases when gas jets impinge directly on the surface of the sample. The scanning electron micrographs show that the gas jets cause a more uniform surface texture than is formed during sputtering when no gas flows. Therefore gas-jet enhanced sputtering should decrease preferential sputtering and matrix effects, and present a highly representative fraction of the sample to the spectrometer for analysis.

6. Acknowledgement

The authors thank Analyte Corp. for a grant and loan of the Atomsource, and John Arthur for the use of the SEM.

V. JET-ENHANCED SPUTTERING AS AN ION SOURCE FOR MASS SPECTROMETRY

by

Hyo J. Kim and Edward H. Piepmeier

Department of Chemistry

Oregon State University

Corvallis, OR 97331

for submission to Analytical Chemistry.

1. Brief

A jet-enhanced sputtering cell is interfaced to the mass spectrometer of a VG PlasmaQuad ICP-MS, replacing the ICP, and the influences of pressure, current, anode voltage, sampling distance, and sampling cone hole size are studied to improve analytical performance.

2. Abstract

A jet-enhanced sputtering cell, the Atomsource from Analyte Corporation, is interfaced to the mass spectrometer of a VG PlasmaQuad ICP-MS, replacing the ICP. The sputtering cell allows for the direct analysis of flat metal samples by clamping them over a round opening, surrounded by an O-ring, in one side of the cell. Six streams of argon, accelerated to high speed by passage through small nozzles and ionized by the current, strike the sample in a hexagonal pattern, sputtering out atoms and rapidly eroding the sample surface. Ions produced by the electrical discharge enter the mass spectrometer through a modified sampling cone. The influences of pressure, current, anode-to-sampling cone voltage, sampling distance, and sampling cone hole size are optimized to obtain improved performance for analytical applications. Because air and water are not present during sample atomization (except as surface contaminants), there are reduced interferences from ArO, ArC and ArN. Detection limits are generally comparable to those obtained with the ICP-MS. Differences in interferences improve the detection limits in some cases, such as B and some transition elements in Zircaloy.

In recent years, glow discharge mass spectrometer applications in the analytical laboratory have increased substantially. The possibilities of the gas glow discharge as an ion source were discovered by Goldstein [179] as early as 1886. Among the pioneering

developments, Aston [179] used the glow discharge as an ion source for the determination of isotope ratios, and Bainbridge [180] used a glow discharge tube in which Zn was sputtered from the cathode for a similar application.

A spark discharge source [181,182] is suitable for both the vaporization and the ionization of inorganic samples. Although this source has excellent sensitivity, offers good ionization efficiency, and allows use of a variety of sample types, its use poses several problems, including ion beam fluctuations resulting in poor analytical precision and a large ion energy spread requiring the use of an expensive double focusing mass spectrometer.

The development of the secondary ion mass spectrometer (SIMS) [183] helped to improved the mass spectrometer analysis of inorganic samples. Secondary ions from the sample surface are released when the surface is struck by the energetic primary ions, following which the secondary ions are extracted and analyzed. This technique is good for both bulk analysis and depth profile determinations. Its disadvantages are similar to those of the spark source, including poor analytical precision and expensive instrumentation.

Recently, glow discharge sources have been developed for a number of optical spectroscopy and analytical applications because of their stability, precision, and sensitivity. Coburn et al. [184] used glow discharges as ion sources for the analysis of thin film and bulk samples. Oechsner and Gerhard [185] reported direct solid analysis with the use of a high frequency plasma source interfaced to a mass spectrometer for sputtering and ionization of samples. In 1978, Harrison et al. [186] first applied a direct current (dc) glow

discharge ion source in combination with a quadrupole mass filter. They obtained successful analytical results. Since then they have extensively investigated the uses of glow discharges for elemental determinations [187-189]. The commercial glow discharge mass spectrometer, the VG 9000 (VG Isotopes, Ltd., Cheshire, Great Britain), uses a reverse Nier-Johnson geometry double-focusing mass spectrometer to obtain high resolution. A 27-cm radius magnetic sector is coupled to a 38-cm radius electrostatic analyzer, achieving up to 6000-8000 resolving power. This device has been used in a variety of direct analysis applications, including electrically conducting and semi-conducting solid materials, nonconducting materials mixed with electrical conducting materials, and liquid samples absorbed on a suitable support matrix [190,191]. However, this commercial system has not gain widespread use, probably due to its high cost.

Several attempts have been made to reduce costs by the use of quadrupole mass filters [192-194]. In particular, Jakubowski, Stuewer and Toelg [195,196] constructed two new glow discharge ion sources with improved designs for use with quadrupole mass spectrometers. Use of these types of sources has made it possible to improve performance for analytical applications.

For the current study, the newly developed Atomsource (Analyte Corporation, Grants Pass, Oregon) was tested to determine its possible applications [197]. A flat sample can be conveniently mounted on the outside of the cell. The Atomsource is a glow discharge similar to the Grimm discharge, but has six strategically located gas jets that improve the analytical performance. The six argon jets strike the

sample surface causing the atoms to be removed from the sample at a much faster rate than ordinary glow discharges. The surface is quickly removed and the main bulk of the sample reached in a matter of seconds. The jets also quickly sweep the sample ions toward the observation region, into the mass spectrometer, thereby increasing the ion current. For this study, the Atomsource was interfaced with the mass spectrometer of a VG PlasmaQuad ICP-MS, without major changes. With the proper computer command the ICP automatically moves out of the way, leaving room to mount the Atomsource.

3. Experimental Section

3.1 Ion Source

Figure V.1 shows a schematic of the gas-jet enhanced sputtering ion source and its interface with the VG PlasmaQuad mass spectrometry (a more detailed description of the gas-jet enhanced sputtering system may be found in [197,198]). Asterisks indicate added or modified parts. The sampling cone of the mass spectrometer was replaced with a sampling cone that allows inserts with different diameter holes to be used as discussed later. A quartz tube (12-mm I.D.) is used to guide the ions from the region near the anode to the sampling cone hole. A mechanical pump that is ordinarily used to maintain a low pressure inside the ion source was not used for this study because the plasma was unstable due to competition between the ion source and mass spectrometer vacuum pumps. The vacuum in the expansion stage of the

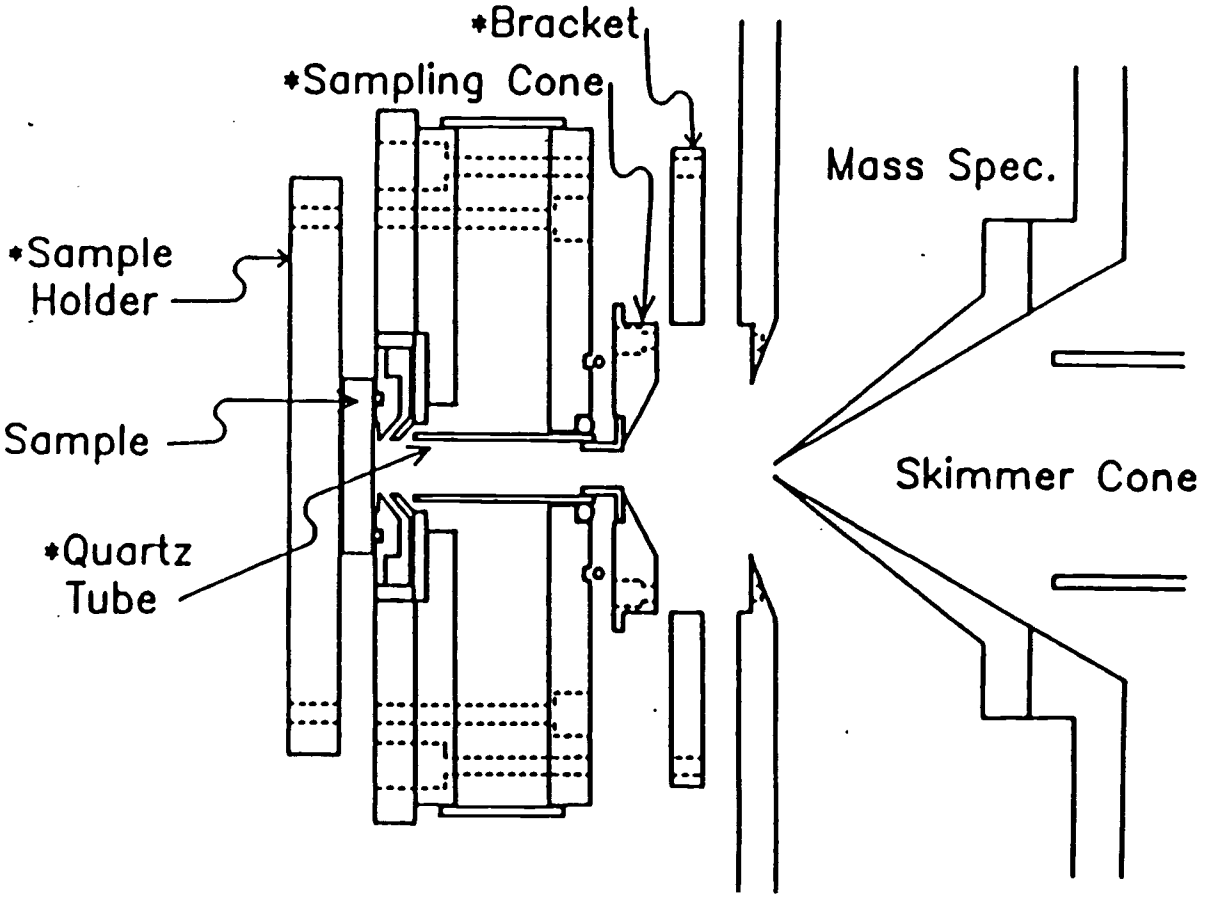

Figure V.1 Schematic of a gas-jet enhanced sputtering ion source and its interface with a VG PlasmaQuad mass spectrometer. Added or modified components are indicated with an asterisk. Dashed lines indicate bolt holes.

mass spectrometer is sufficient to maintain the required low pressure in the Atomsource. The operating pressure of the ion source is maintained by controlling the Ar gas flow rate into the source with a mass flow controller (Sierra Instrument, Carmel Valley, California). The pressure is measured by a variable reluctance transducer (Validyne #AP10, Northridge, CA) with a carrier demodulator (Validyne #CD15) pressure gauge attached to a "T" connector at the gas entrance to the Atomsource.

The sampling cone is connected to ground potential. In order to bias the anode positively against the sampling cone, an additional variable 60-V power supply (Model EUW-17, Heath Instruments, Benton Harbor, MI) is used. A series of up to three variable 400-V, 100-mA Heath power supplies (Model EUW-15, Heath Instruments, Benton Harbor, MI) is used as an external power supply for the sputtering current (for reasons which will be discussed later).

3.2 Mass Spectrometer

A VG PlasmaQuad mass spectrometer (VG Elemental, Great Britain) was used for this study and a schematic of its main components is shown in Figure V.2. Different parts of the spectrometer are held at different pressures to assure correct operation of the plasma sampling interface and the quadrupole mass spectrometer. In order to maintain these pressures, a combination of rotary and diffusion pumps is used. The use of the Atomsource required no change in the pumping system of the mass spectrometer.

The interface between the gas-jet enhanced ion source and the

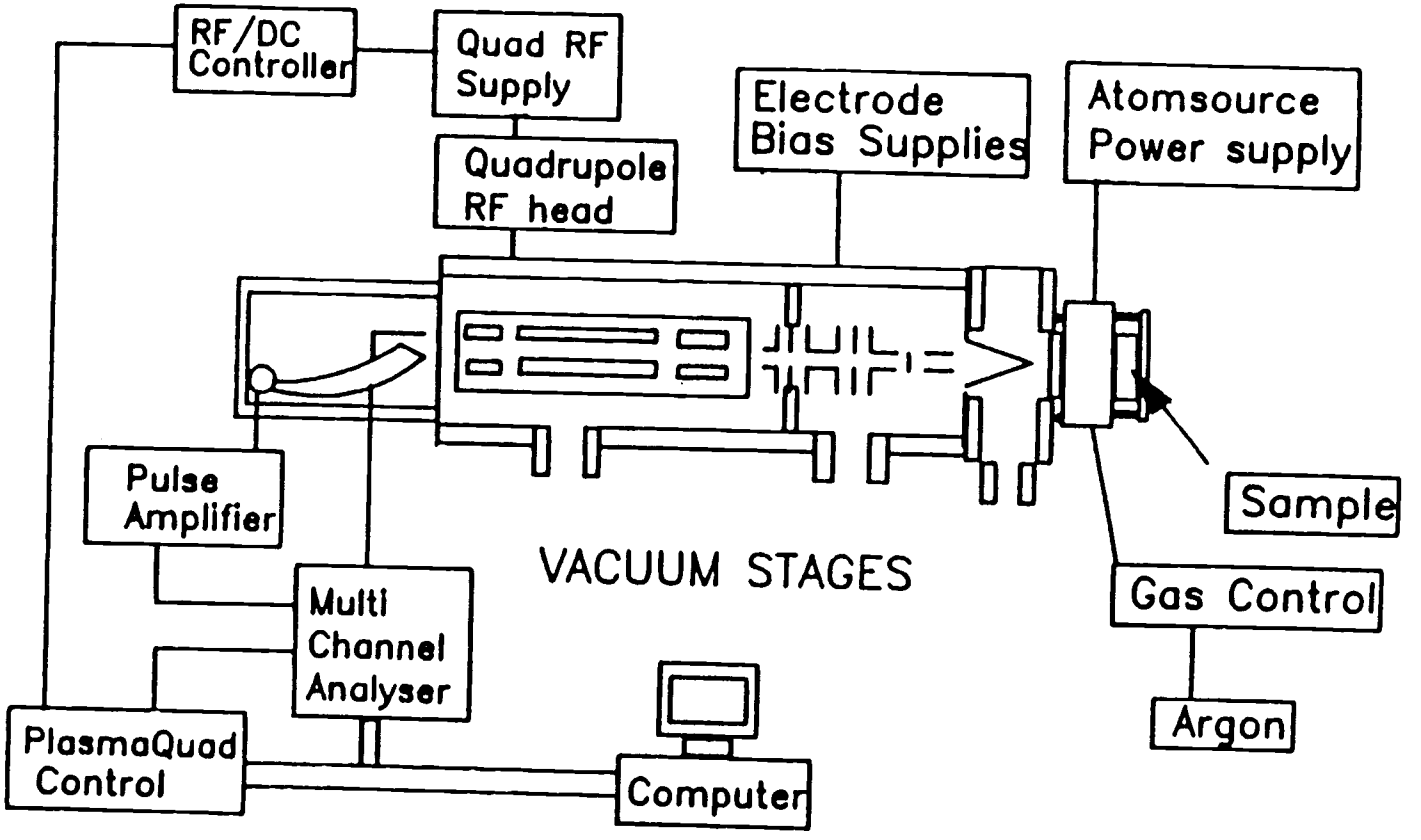

Figure V.2 Schematic of VG PlasmaQuad ICP-MS and Atomsource.

mass spectrometer is composed of two cones: a special sampling cone and the original skimmer cone. Various types of sampling cones were constructed and are discussed in more detail later.

3.3 Sample Preparation

One zirconium standard (X-866), one Zircaloy standard (X-868), and one Zircaloy sample are used for this study. Samples were analyzed directly without major preparation. The samples were polished and then surface cleaned by rinses in ethanol, dilute HNO_3, and deionized-distilled water.

4. Results and Discussion

4.1 Power Supply

After constructing a mount and an interface between the six-jet Atomsource and the mass spectrometer, a spectrum of a zirconium standard (X-866) was obtained, as shown in Figure V.3. The highest peak is ^{40}Ar and the ^{90}Zr peak is barely visible on this scale. Unexpectedly strong ^{58}Ni and ^{60}Ni peaks were obtained, which were attributed to sputtering of the original Ni sampling cone ordinarily used with the ICP. Various types of sampling cones and interfaces were constructed in an attempt to avoid etching of the sampling cone. However, geometric modification failed to completely solve this problem because both the sample and the sampling cone were connected

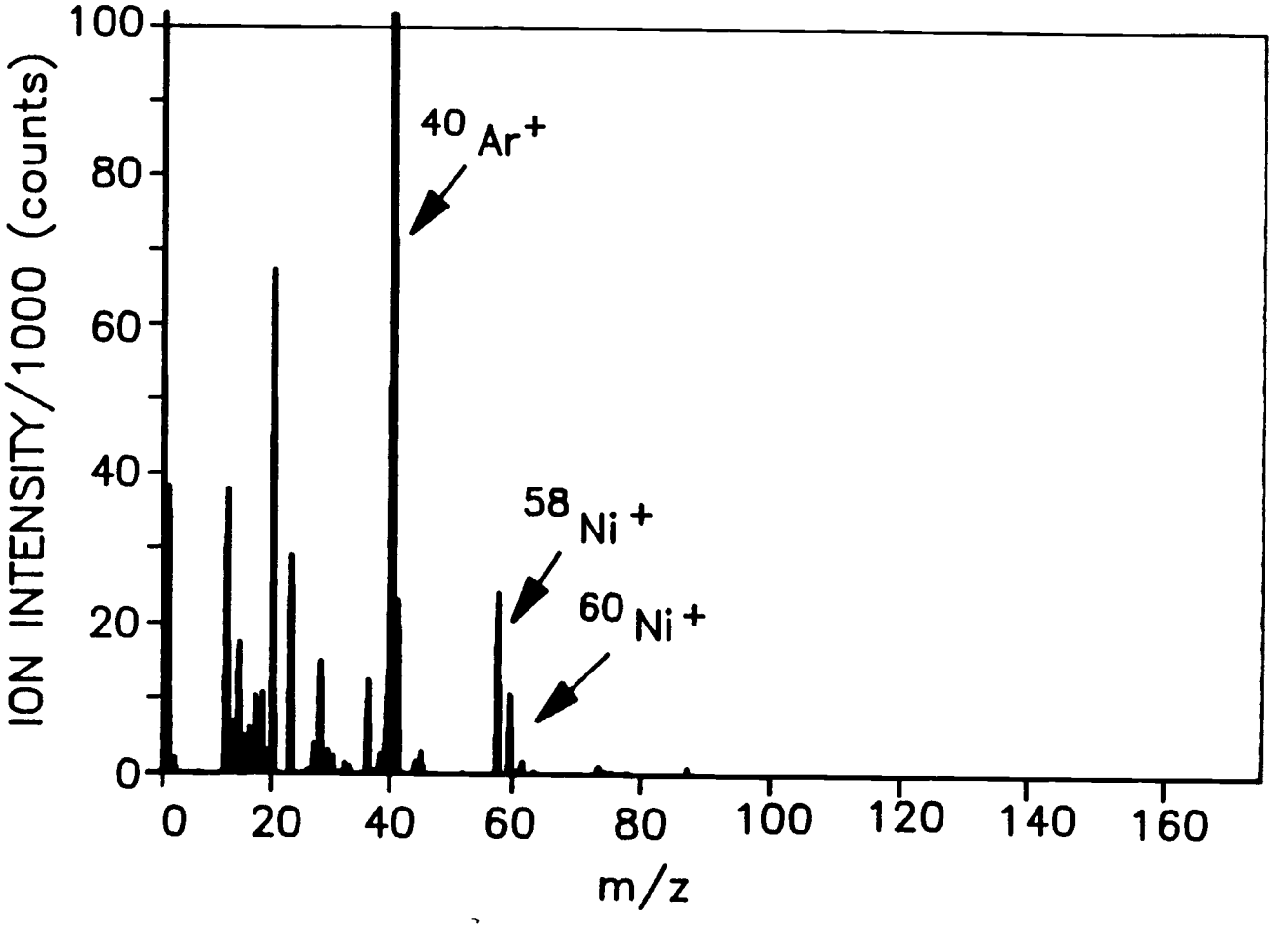

Figure V.3 Spectrum of zirconium standard (X-866) obtained with a original Atomsource power supply.

to ground potential and the Ar ions attacked both. This problem was solved by using a different power supply configuration in which the anode was connected to ground potential and the cathode (sample) was connected to a negative potential. In the original Atomsource power supply, the anode is at a positive potential and the cathode is connected to ground potential. The resulting mass spectra (Figure V.4) showed an increase in Zr peaks by a factor of 10,000 and no Ni peaks from the cone material, indicating that this problem was solved. Further improvements in ion signal were obtained with an additional adjustable power supply that kept the anode 40 to 50 volts positive with respect to the grounded sampling cone.

4.2 Sampling Zone Distance and Sampling Cone Hole Size

The sampling distance between the cathode surface and the sampling cone exit aperture is an important variable. Jakubowski et al. [195] investigated the dependence of ion intensities on the sampling distance for a glow discharge. The intensities of the molecular ions show a rapid decrease with decreasing sampling distance, whereas the intensities of the analyte ions show an exponential increase. They also noted that further decreases in the sampling distance appears to be advantageous, but subsequently leads to depression of the extracted ion current as deposition of the sputtered material begins to clog the exit aperture.

Therefore, to generate strong ion signals, but also reduce the possibility of clogging the exit aperture, it was necessary to choose a compromise value for the sampling distance. To decrease the

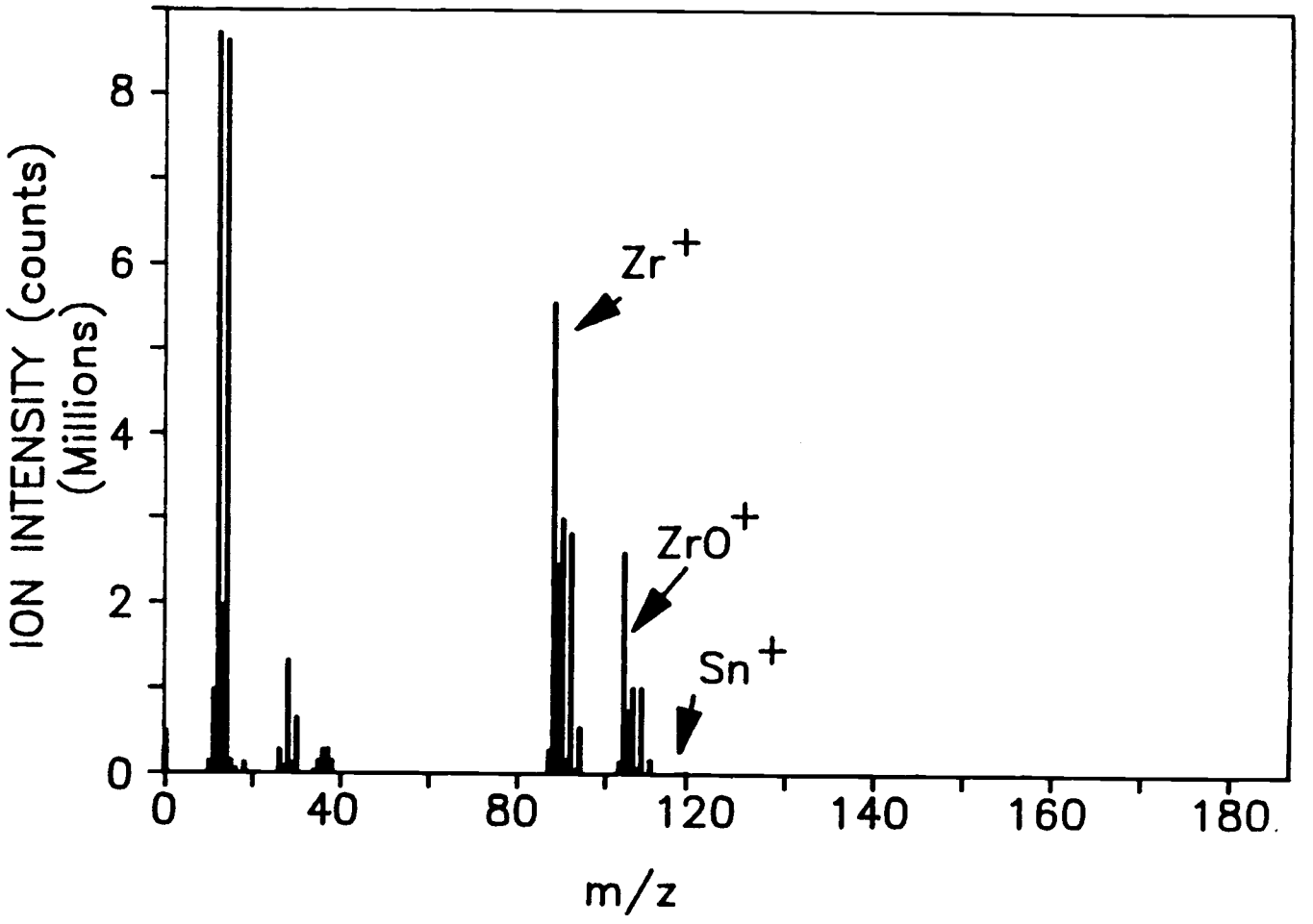

Figure V.4 Spectrum of zirconium standard (X-866) with modified power supply.

sampling distance, a flat sampling cone with a 5-mm I.D. aperture (Figure V.1) was designed to replace the ordinary sampling cone. This also reduced the sampling distance as far as possible without redesigning the main housing of the Atomsource.

The sampling cone hole size affected the pressure gradient between the Atomsource and the inside of the mass spectrometer, and thereby probably affected the efficiency of extraction of the analyte ions into the mass spectrometer. Figure V.5 shows the effect of sampling cone hole size on ion intensities. The ion intensities increase with increases in the sampling cone hole size, but progressive increases of the sampling cone hole size lead to deposition of the sputtered material, and eventually to clogging the skimmer cone aperture. Therefore a 0.3-cm I.D. sampling cone hole, 1.0-cm long was used.

4.3 Optimization of Operating Parameters

Gas pressure is a critical parameter in glow discharge sputtering processes. It is known that a decrease in pressure increases the sputtering rate due to an increase in the voltage required to maintain the same current, and an increase in the mean free path of the argon ions, which gain more energy before striking the surface. Lower pressure can also reduce redeposition near the cathode surface because the sputtered atoms escape into the vacuum more freely. However, Figure V.6 shows that ion intensity for ^{56}Fe initially increases with increases in pressure, a likely result of several effects. The increase in ion intensity with increased pressure may result from the

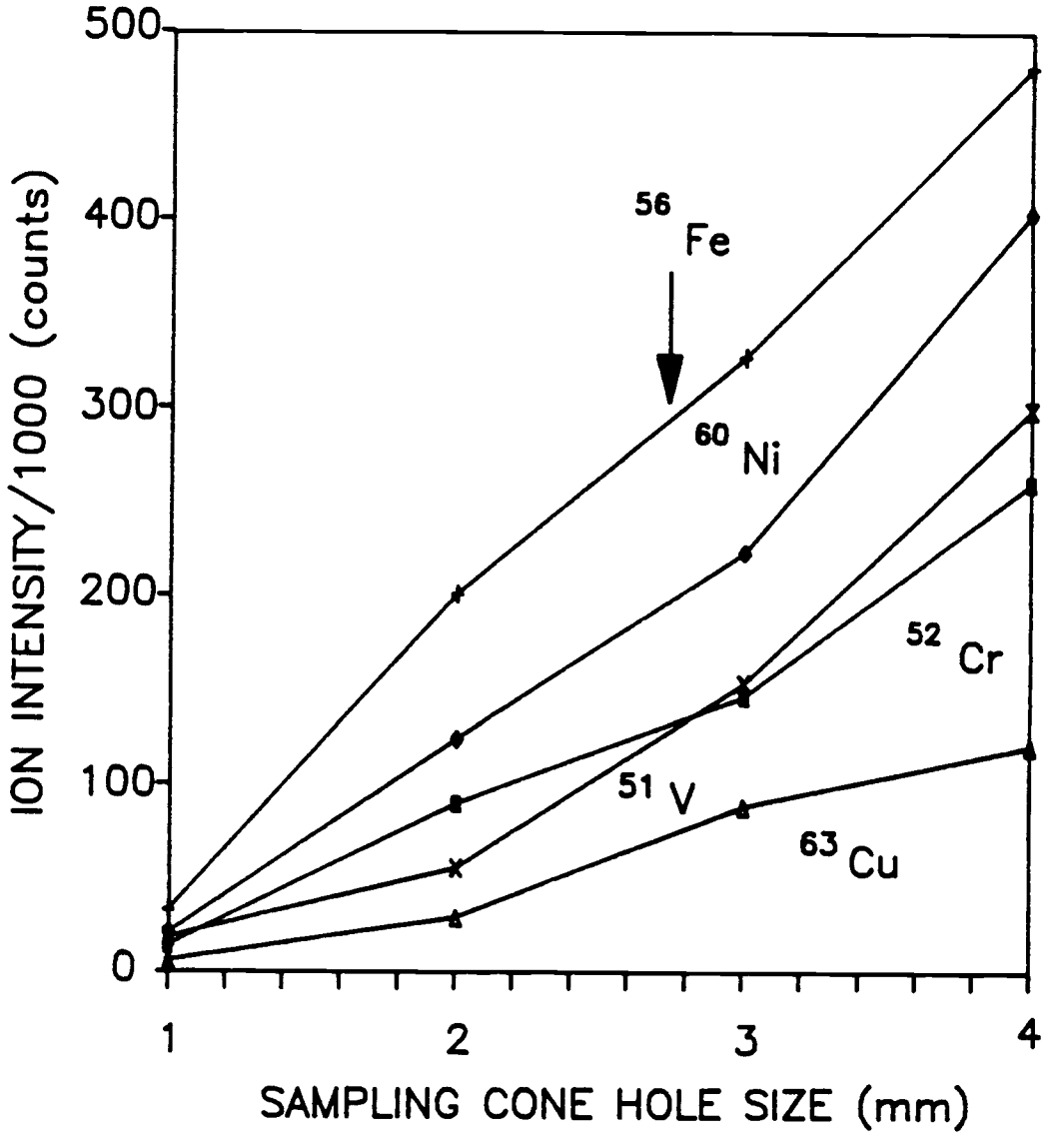

Figure V.5 Ion intensity vs. sampling cone hole size.

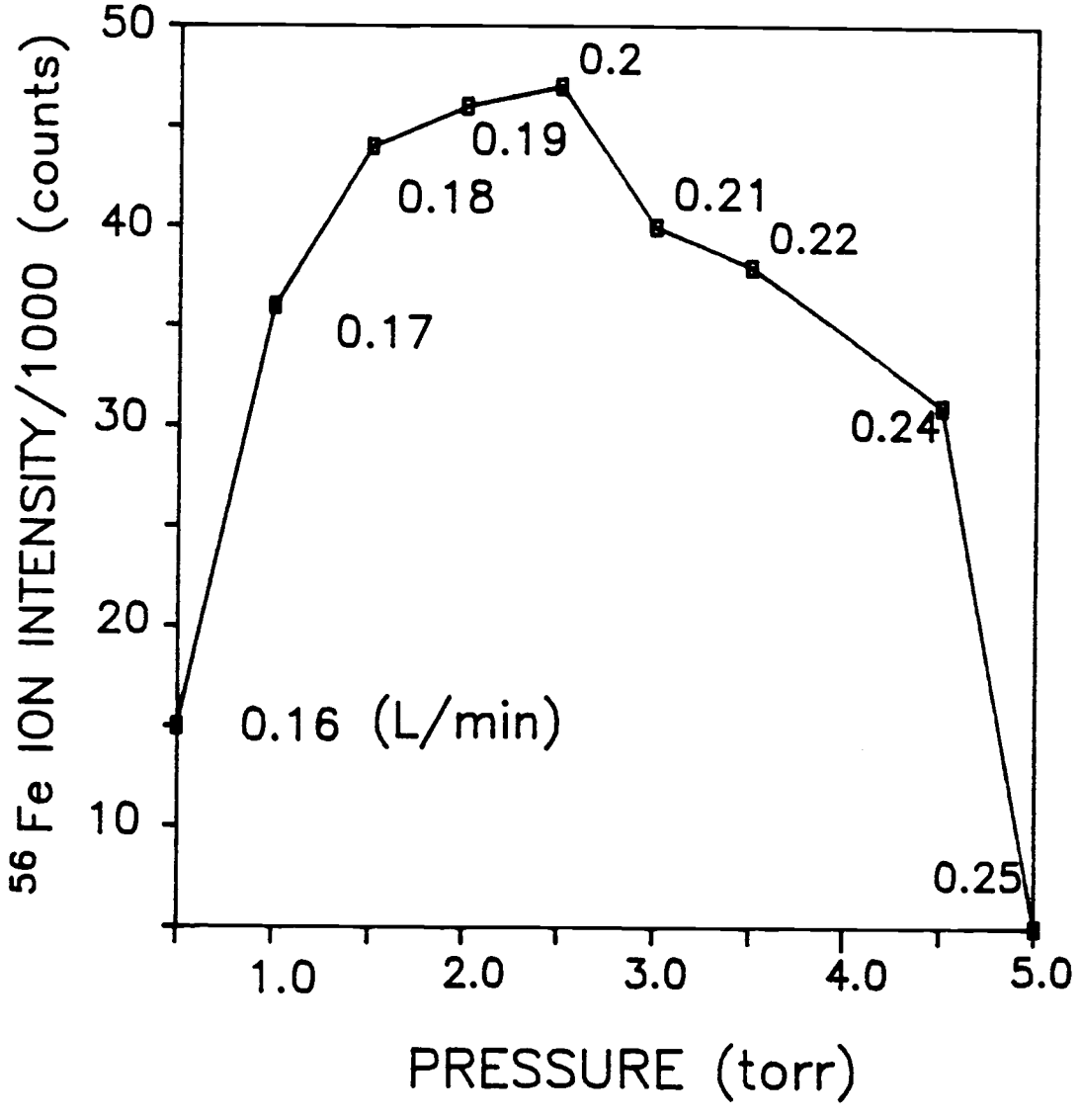

Figure V.6 Pressure effect on ion intensity.

greater pressure differential between the source and the inside of the mass spectrometer, moving the ions more quickly into the mass spectrometer. An increase in pressure is accomplished by an increase in jet gas flow rate, which may increase the efficiency with which atoms are swept away from the surface before they can diffuse back and redeposit. It is also possible that Penning ionization efficiency may be increased due to increases in argon metastable density at the higher pressure [193]. Analyte ions must be generated in the gaseous part of the discharge, because ions sputtered off of the sample surface are forced back to the surface by the electric field. Eventually the ion intensity decreases with further increases in pressure, because the sputtering rate decreases as ordinarily expected with increasing pressure. This curve shows a rather broad and flat maximum, a region which offers good signal stability during pressure variations.

The dependence of ion intensity on the discharge current is shown in Figure V.7. Ion intensity initially increases with increased discharge current, up to 27 mA. As the current increases, the number of bombarding ions increases, leading to an increase in sputtering. Above 28 mA, there is an unexpected decrease in ion signal. It may be that the increase in electrical power increases the gas temperature and thereby shifts the position of the slightly asymmetric flowing stream so that a different part of the plasma is sampled by the skimmer cone. A nonuniform distribution of ions in the cross section of the flowing plasma could then produce such a change in ion signal.

Another explanation is that the higher anode-to-cathode voltages associated with the higher currents attract more ions back towards the

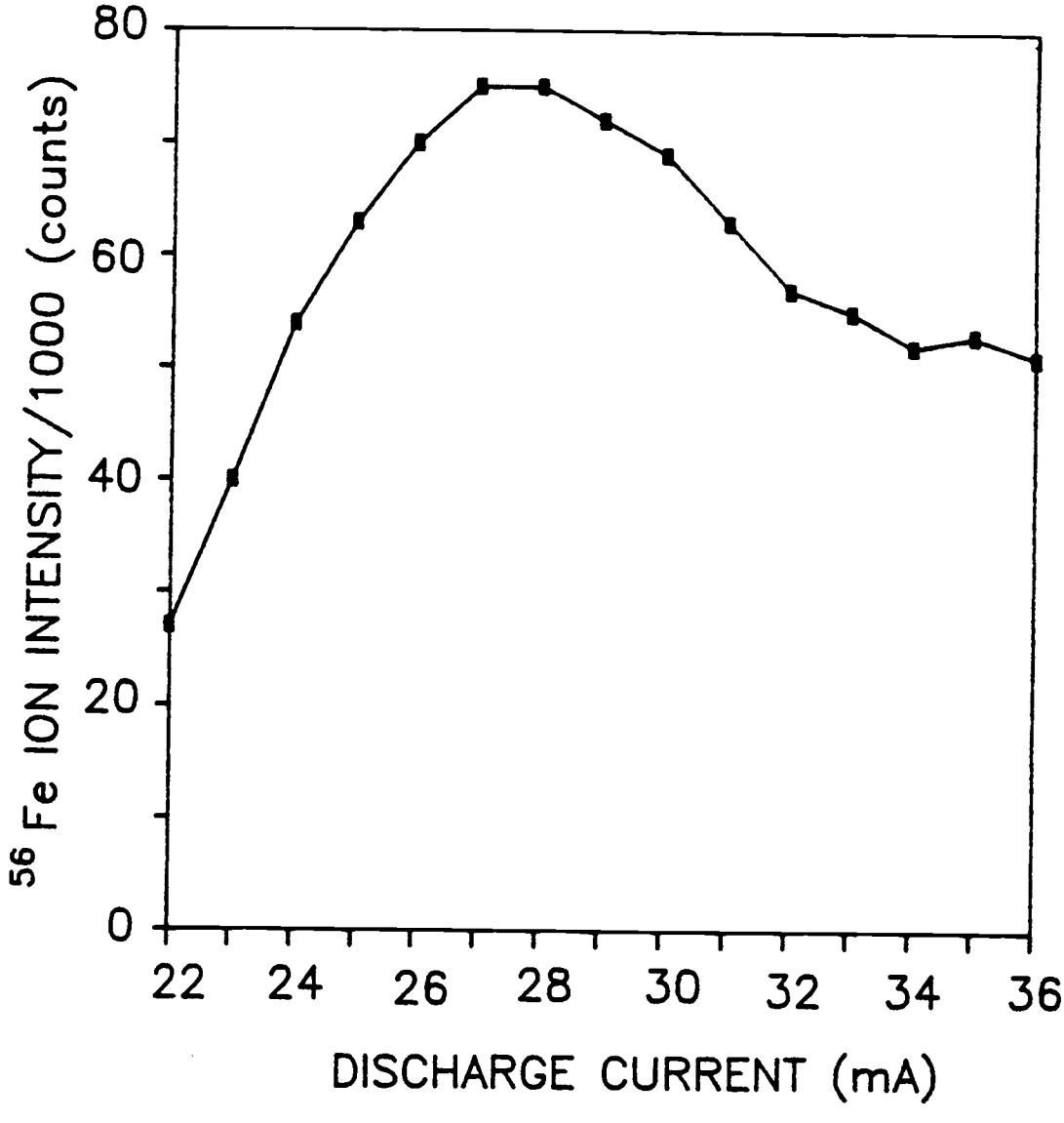

Figure V.7 Discharge current effect on ion intensity.

cathode. If this were the case, then it would mean that analyte ions were formed near the cathode fall region since this region is where most of the increase in voltage drop occurs.

Figure V.8 shows the effect of anode voltage (with respect to the grounded sampling cone) on ion intensity at a current of 27-mA and a pressure of 2-torr (the anode-to-cathode voltage remains constant). There is an optimum anode voltage for maximum ion intensity.

All of the maxima in the values of the operating variables help to improve signal stability. Although there is some interaction among the variables, a global maximum is readily obtained by adjusting the value of each variable in turn to reach a maximum and going through this cycle only a few times.

4.4 Auxiliary Discharge

A high-voltage secondary glow discharge, as proposed by Harrison and Bentz [194] was used to increase ion intensity. Figure V.9a shows the Zr-standard spectra without the secondary discharge. Figure V.9b illustrates the Zr-standard spectra with two radially introduced additional W electrodes for a secondary glow discharge located two-thirds the distance from the anode to the sampling cone. All of the ion intensities increased approximately 30 percent when the secondary discharge was used. However, unwanted W ion and W oxide molecule signals, resulting from sputtering of the secondary electrodes, were also obtained. After lengthy periods of operation, instability was another problem connected with the secondary discharge. The reason may be that sputtered sample material was

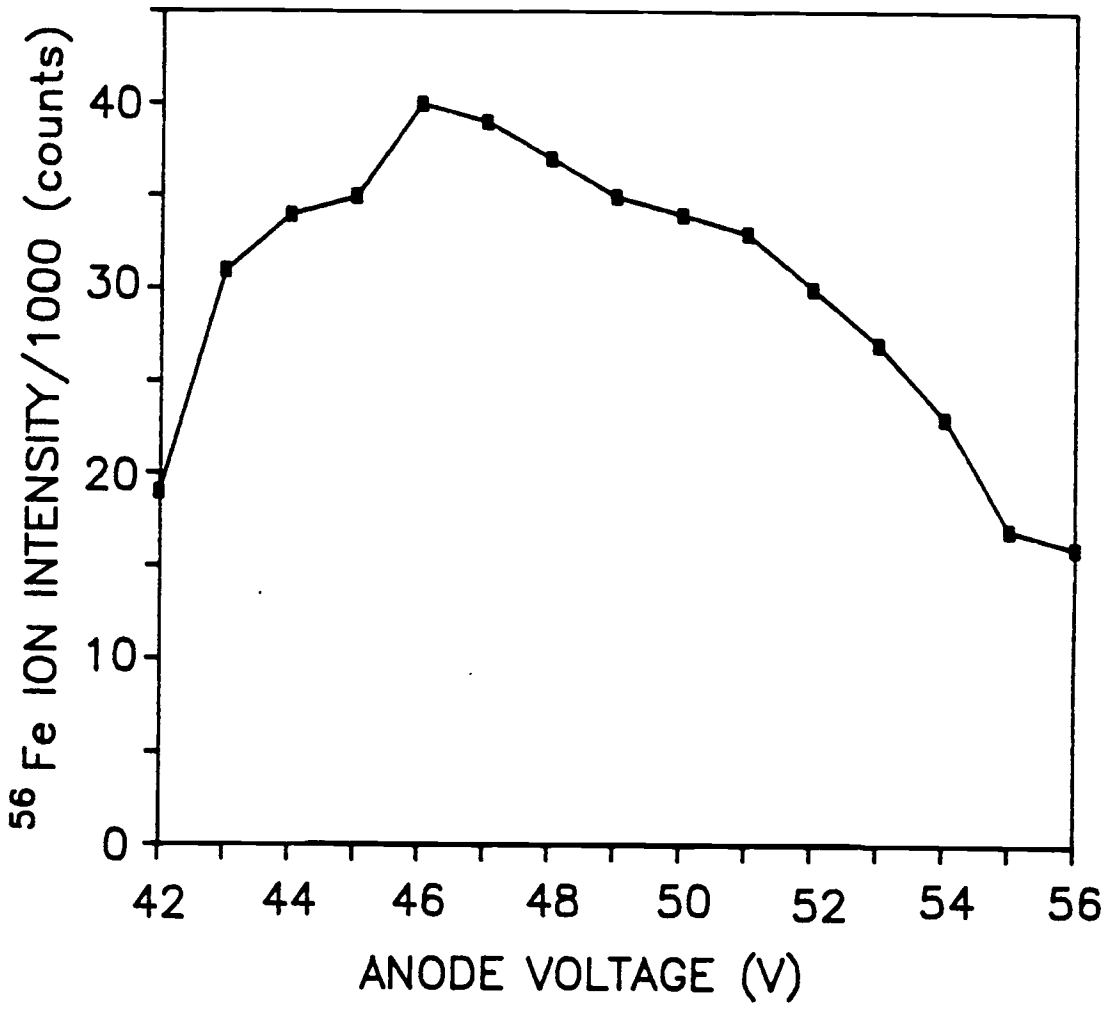

Figure V.8 Anode voltage affect on ion intensity.

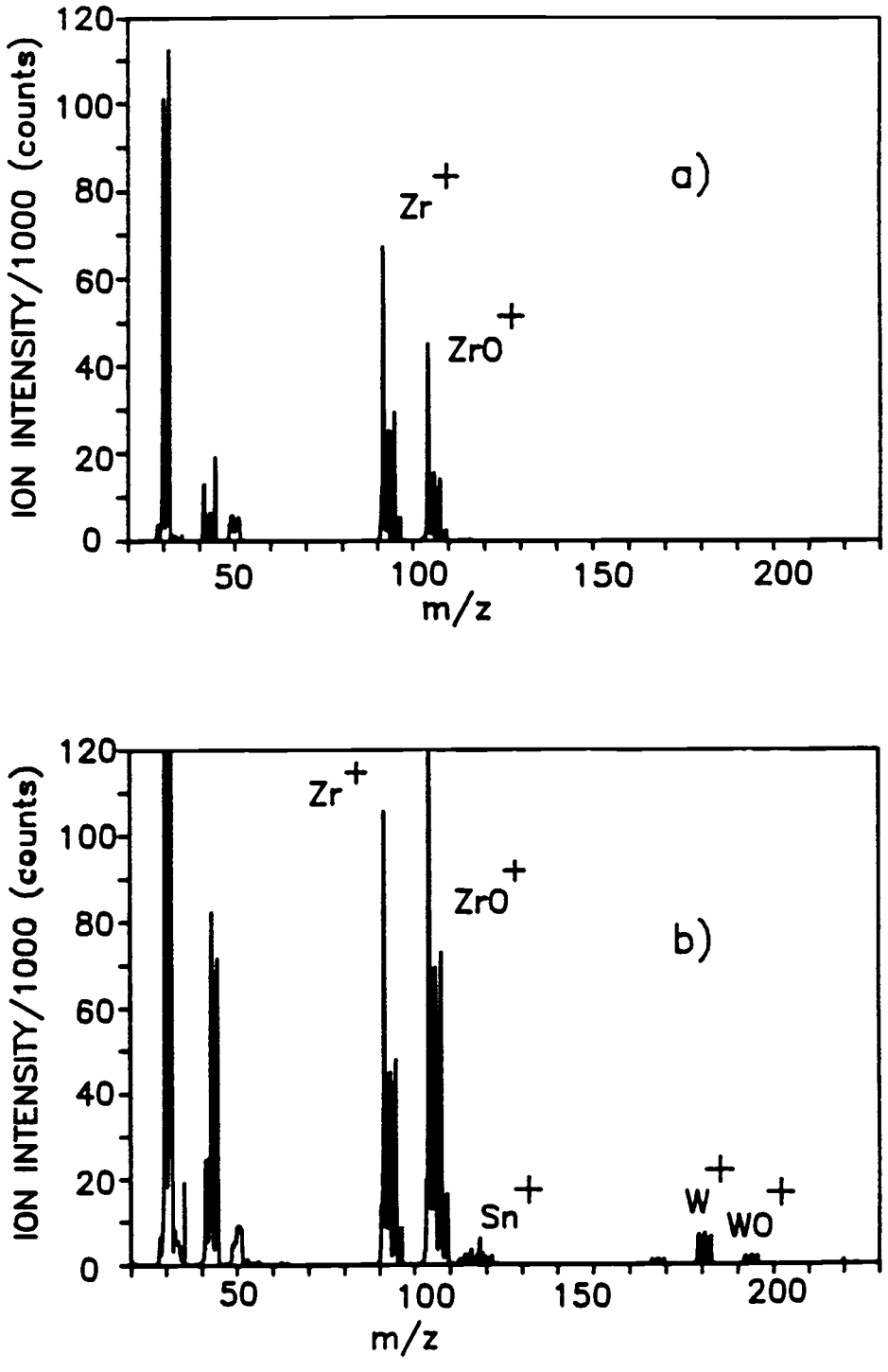

Figure V.9 a. Spectrum obtained without the auxiliary discharge,

b. Spectrum obtained with the auxiliary discharge.

deposited on the W secondary electrodes, causing a change in their electrical characteristics. Because of these problems and the relatively small increase in signal, further studies were not made using the auxiliary electrodes.

4.5 Multi-Element Determination

Figure V.10 shows the Zr alloy spectrum resulting when the optimum values for the operating parameters are used. This spectrum was obtained with a 700-V, 28-mA discharge at 2-torr pressure. The Zr alloy (X-868) contained 20 elements with certified values listed in Table 1. Identified are isotopic peaks for Cr, Fe, and Sn, at concentrations of 500 ppm, 2700 ppm and 1.23% respectively. To prevent detector saturation resulting from ion counts which are too high, mass ranges of 16 to 20 (O^+), 32 to 42 (Ar^+) and 89 to 97 (Zr^+) were skipped during the scan.

4.6 Select Group Determination

In order to obtain more accurate information for isotopes of particular interest, the scan range was reduced to the region near these isotopes. A 1024-channel data acquisition was set around each isotope region. The dwell time at each channel was 200 μs and 1000 sweeps were accumulated. The isotopes of interest for a Zr alloy analysis may be all of the elements which the Zr sample contains. However, one of the objectives of this project is to determine how the gas-jet enhanced sputtering ion source and the ICP ion source might

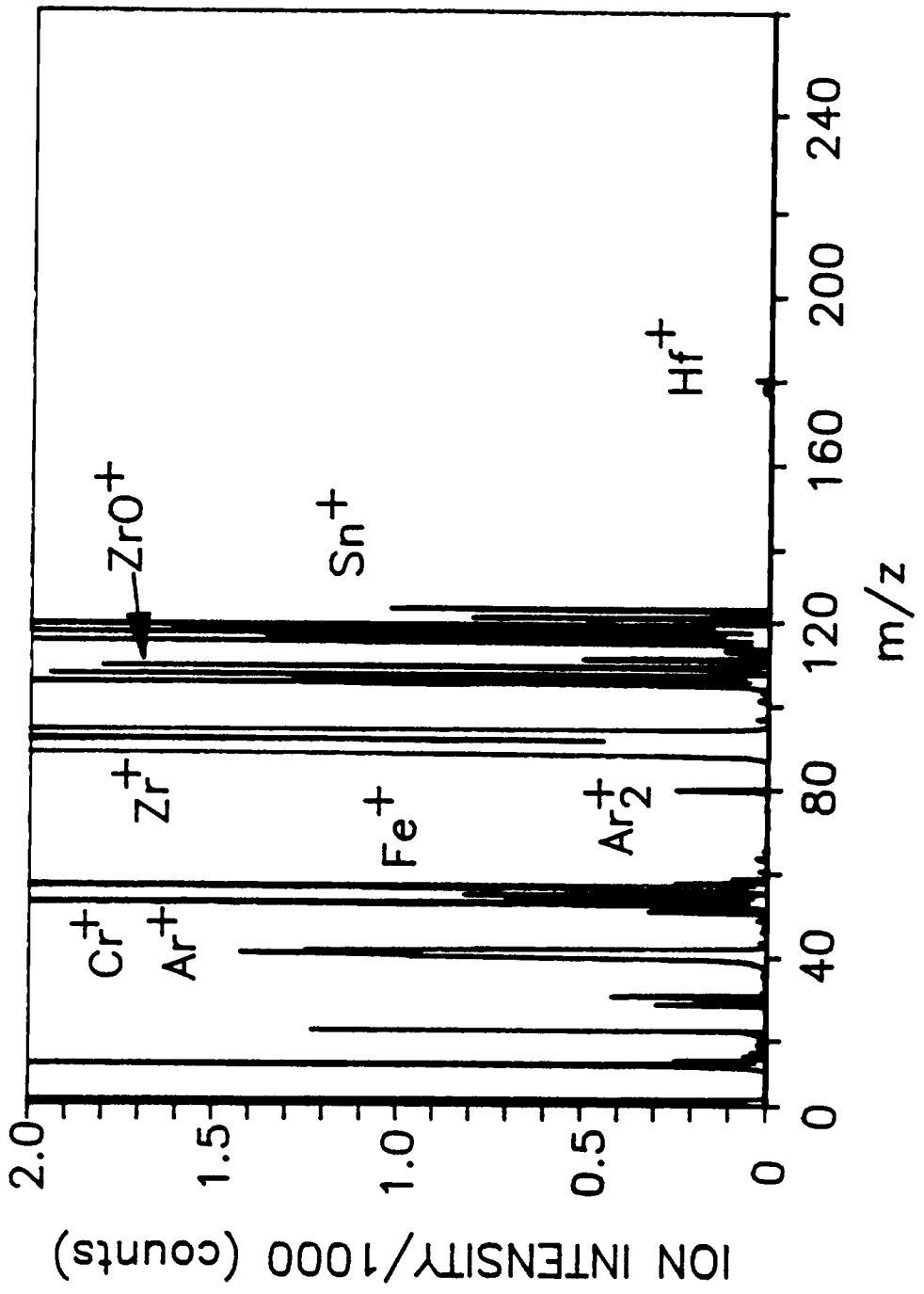

Figure V.10 Spectrum after optimization.

Table V.1 Concentrations in the zirconium standards and sample.

Elements	Concentration (μg/g)		
	X-866	X-868	Sample
Al	310	122	32.3
B	6.9	3.2	-
Nb	612	570	-
Co	42	42	<5
Cr	255	580	1130
Cu	240	83	3.8
Fe	1620	2790	2180
Hf	198	178	47.6
Mn	42	56	<5
Mo	123	128	<5
Ni	129	134	8.58
Pb	33	101	1.4
Si	215	179	106
Sn	14	1.23 %	1.54 %
Ta	709	716	5.8
Ti	122	191	7
V	71	93	<5
W	140	95	1.2
U	0.97	0.79	0.3

complement each other. Thus, elements of a select group were chosen which might pose problems for ICP-MS determinations due to spectral interference and/or contamination during the sample preparation. These elements include boron, some of the transition elements, and some of the rare earth elements. Boron is regarded as one of the more difficult elements to determine in Zircaloy with the ICP-MS because of contamination from boro-silicate glass in the ICP spray chamber and torch when dilute HF solutions are used.

The spectrum for a Zircaloy standard (X-868) containing 3 μg/g boron is shown in Figure V.11. This spectrum, covering the range m/z = 9 to m/z = 16 was taken in 3 min. The boron isotopes are found to be in the approximately correct natural isotopic abundance. Broadening of the ^{12}C peak, possibly due to an unresolved peak, was a problem. For the most part this occurred when a large carbon signal was present. The observed boron isotope abundance ratio between ^{10}B and ^{11}B is estimated as 0.26, which differs by only 4 % from the natural abundance ratio, well within the uncertainty caused by counting statistics. The integrated peak channel count for ^{11}B was 910. The background channels between m/z = 9 and m/z = 10 had an accumulated count of 30. The detection limit, determined in theory by dividing 3 times the standard deviation of the background count by the slope of a two-point standard curve (the first point being the background average, designated as zero concentration) for B in Zircaloy is estimated to be 0.05 μg/g. In ICP-MS the detection limit of boron (above its background interference mentioned earlier) is 10 ng/mL, or 10 μg/g in a solid dissolved in a 0.1% solution.

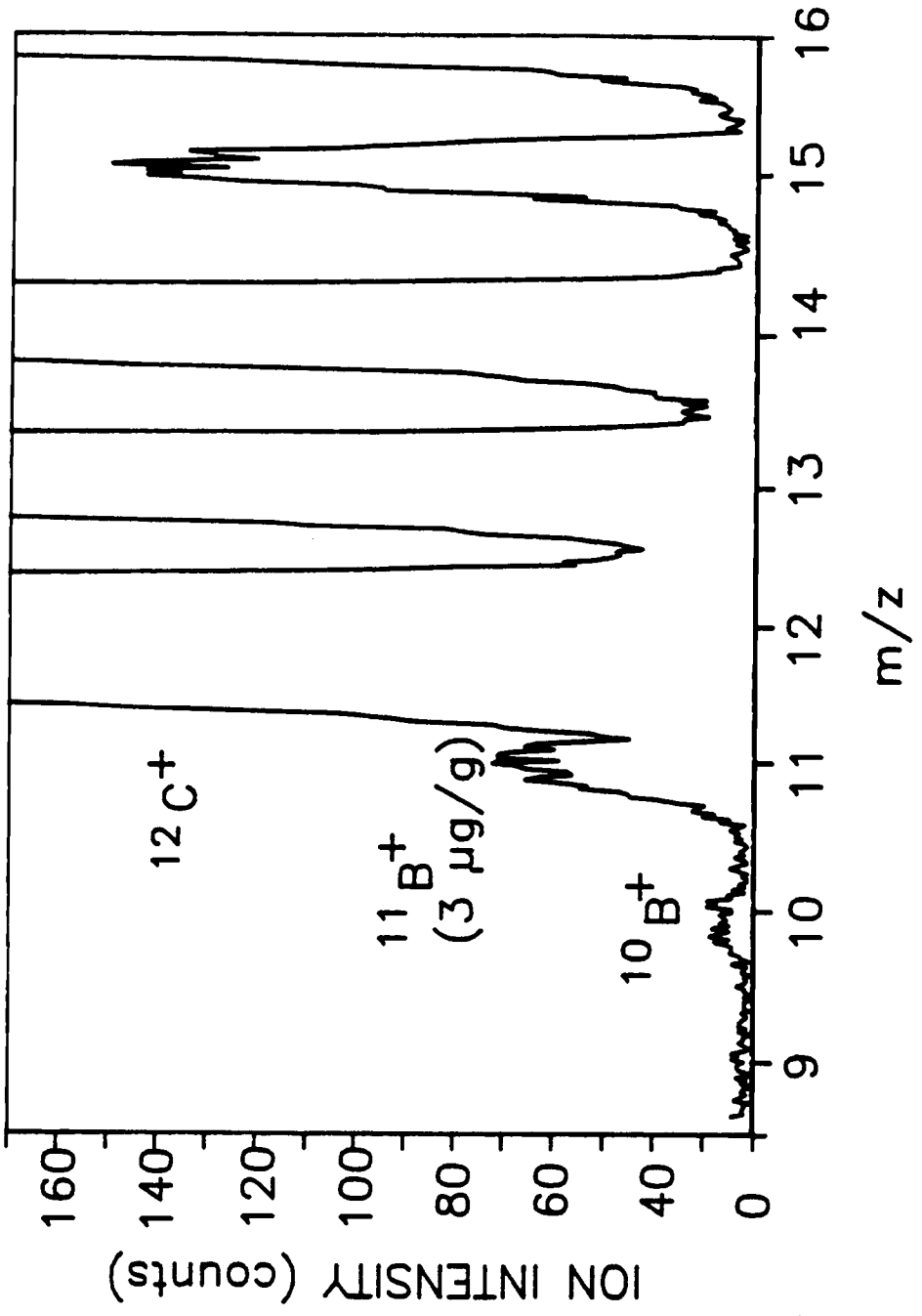

Figure V.11 Boron spectrum obtained in 3.4 min. (1024 channels, 200-μs dwell time per channel, 1000 scans).

Although rare earth elements are routinely determined in zirconium alloys by ICP-MS [199] there are occasional difficulties. Sources of interference found in earlier ICP-MS instruments are rare earth oxide and hydroxide ions [200]. Proper selection of isotopes can reduce these interferences. At higher concentrations of rare earths or other elements whose fluorides precipitate, precipitation or coprecipitation during acid digestion of the sample may cause problems.

Figure V.12 shows the spectrum obtained with the same settings used for boron, but covering the range m/z = 137 to 180. The spectrum is noisy but the rare earth peaks are obvious and well resolved (except for isotopes with essentially the same m/z). In the ICP-MS no peaks in this mass range are observed with the same sample dissolved in a 0.1 % solution (1000 dilution factor with respect to the solid). The peak channel count for the ^{140}Ce ion is 22. The lowest channels between between the ^{140}Ce ion and the ^{141}Pr ion have an accumulated count of 0 or 1. Although several peak superpositions occur, every element has at least one isotope free from such interference.

The zirconium alloy contains several transition elements, including Ti, V, Cr, Mn, Fe, Co, Ni, Cu, and Zn. However, Ti and Fe pose a number of problems to the ICP-MS method because of spectral interferences. Some of the Ti isotopes of 46 (8.0% natural abundance), 47 (7.5%), and 48 (73.7%), are interfered with by the doubly charged zirconium isotopes, 90 (51.4%), 91 (11.2%), 92 (17.1%), 94 (17.5%), and 96 (2.8%). The Fe isotopes are 54 (5.8%), 56 (91%), 57 (2.14%), and 58 (0.31%) and the major ^{56}Fe peak is interfered

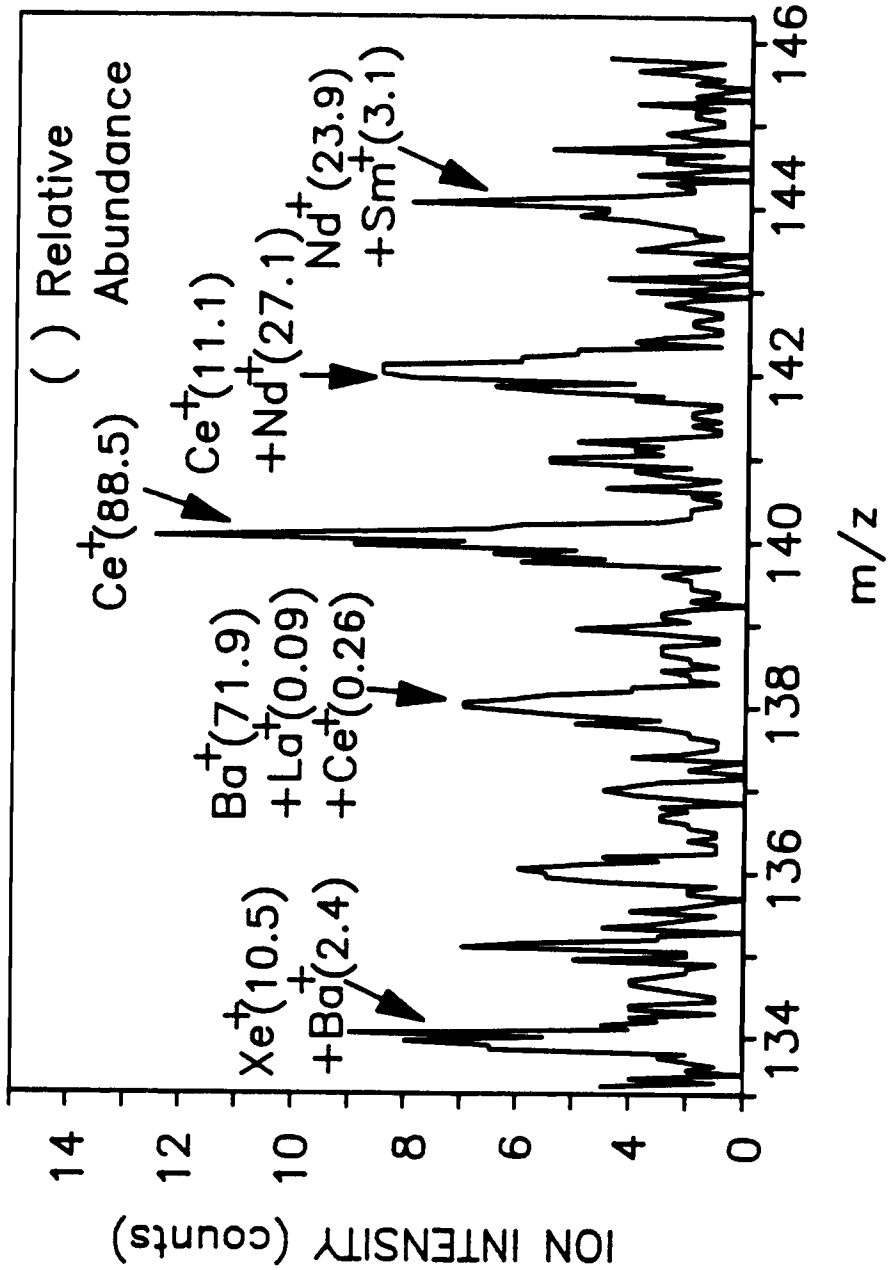

Figure V.12 Rare earth spectrum obtained in 3.4 min. (1024 channels, 200-μs dwell time per channel, 1000 scans).

with by ^{56}(ArO), and the next most abundant ^{54}Fe isotope is interfered with by ^{54}(ArN), both of which are derived from water and plasma gas. In ICP-MS, the assigned species for m/z 56 and 58 were confirmed by substitution of natural water with $H_2{}^{18}O$ [201]. Only ^{57}Fe reflects a good choice, free from spectral interference, but its 2 % natural abundance makes it difficult to determine the lowest Fe concentrations.

Figure V.13 shows the spectrum obtained with the same experimental settings as for boron, covering a range between m/z = 42 and m/z = 70, and showing excellent resolution between masses. Natural abundance isotope ratio calculations indicate that there is little if any spectral interference from ^{56}ArO and ^{54}ArN on ^{56}Fe and ^{54}Fe using the gas-jet enhanced sputtering ion source. For example, the Fe isotope abundance ratio between ^{56}Fe and ^{57}Fe (an isotope with no interference) is estimated as 0.024, which differs by only 9% from the natural abundance ratio of 0.022.

5. Conclusion

This investigation has shown that the Atomsource can be interchanged with the ICP on an ICP-MS to complement its analytical capabilities, especially for the direct analysis of metal alloys. The sample is conveniently mounted on an o-ring sealed hole outside the ion source. High and low concentrations can be observed with the gas-jet enhanced ion source mass spectrometer without the necessity of dissolving the alloy. Although a quadrupole mass spectrometer does

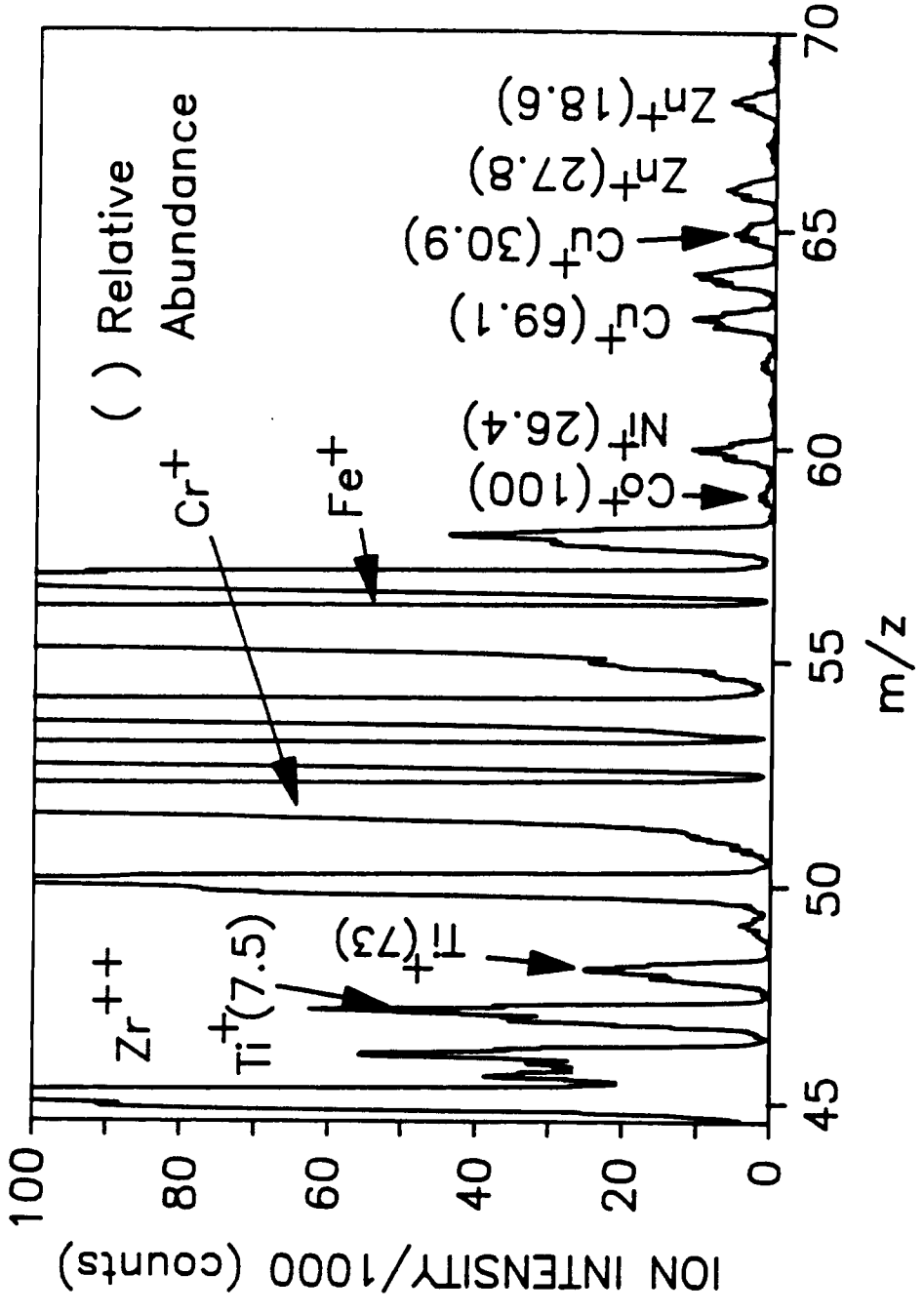

Figure V.13 Transition element spectrum obtained in 3.4 min. (1024 channels, 200-μs dwell time per channel, 1000 scans).

not have the mass resolution of a commercial GD-MS, the relatively low cost of adding an Atomsource to an ICP-MS makes this an attractive alternative when an ICP-MS is already available in the laboratory. Analytical performance and further comparisons to the ICP-MS will be discussed in more detail in a subsequent section of this study.

6. Acknowledgment

We gratefully acknowledge a grant from Teledyne Wah Chang Albany and the loan of the Atomsource by Analyte Corporation.

VI. DETERMINATION OF TRACE ELEMENTS IN ZIRCONIUM SAMPLES BY A GAS-JET ENHANCED SPUTTERING SOURCE MASS SPECTROMETRY

by

Hyo J. Kim and Edward H. Piepmeier

Department of Chemistry

Gilbert Hall 153

Oregon State University

Corvallis, OR 97331-4003

for submission to Analytical Chemistry

1. Brief

The analysis of Zircaloy was studied by a gas-jet enhanced sputtering source mass spectrometer made by replacing the ICP in a commercial VG PlasmaQuad ICP-MS with an Atomsource.

2. Abstract

Zircaloy was directly analyzed for 15 elements by a gas-jet enhanced sputtering source mass spectrometer made by replacing the ICP in an ICP-MS with an Atomsource. Three zirconium standards, one Zircaloy standard, and one Zircaloy sample were studied. Background, memory effects and spectral interferences were investigated. Results, including mass discrimination studies, showed that there is less spectral interference and no memory effect in the Atomsource-MS. The average relative precision of measurement for 10 elements was better than 4 %. In a multielement analysis the detection limits for 13 elements were lower than 0.5 ppm, while single-element determination improved the detection limits by an order of magnitude. For example, the detection limit for U was less than 10 ng/g for the single-element determination. Concentrations determined with an internal standard were in agreement within 10 % of the certified values for most of the elements in the Zircaloy sample.

Inductively coupled plasma mass spectrometry (ICP-MS) as developed initially by Gray and Date [202] is an extremely sensitive method for the analysis of dissolved samples. The inductively coupled plasma (ICP) atomizes and ionizes the sample solutions, and the sample ions are directed into a mass spectrometer through a submillimeter hole in a water-cooled cone at the entrance of the mass spectrometer. The mass spectrometer separates the ions according to their mass to charge

ratio and measures the ion currents. This information is then related back to the concentrations in the original sample by the use of standards.

The use of an electrical glow discharge in place of the ICP has several advantages for alloy analysis. In a glow discharge the sample is one of the electrodes, and sample material is atomized by sputtering when ions strike the sample surface. Therefore, there is no need to dissolve the sample, and potential contamination by solvents is avoided. This direct sampling method also avoids water, which forms oxides that interfere with the mass spectra of some elements.

Glow discharge mass spectrometry (GDMS) was recently comprehensively reviewed by Harrison and Bentz [203], who noted that with more extensive investigation this method has the potential to develop into a major analytical method. For instance, zirconium alloys (e.g., Zircaloy) are used as a fuel element cladding material in the nuclear power industry [204]. For this application, it is necessary to determine the concentrations of a range of elements, including boron, cadmium, and rare earth elements, which influence the quality of the materials. The concentration of uranium and its isotopic ratios are used as a means to ascertain if the Zircaloy is a "virgin material" or is recycled. A fast, accurate Zircaloy analysis is desirable. In order to conduct a complete analysis, a combination of several analytical procedures has been used such as XRF, OES, combustion IR analyzers and SSMS. On the other hand the GDMS, based on a double focusing mass spectrometer, can alone provide a complete analysis, but is very expensive [204].

Following a systematic study of jet-enhanced sputtering in an Atomsource cell [205], a modified Atomsource has been successfully interfaced with a commercial VG PlasmaQuad quadrupole mass spectrometer [206]. In this study, the analytical performance and interferences for the analysis of Zircaloy using this new instrument are investigated and a comparison with an ICP-MS is described.

3. Experimental Section

3.1 Ion Source and MS System

The modified Atomsource and its interface with a commercial VG PlasmaQuad ICP-MS, replacing the ICP, has been described in a previous paper [206]. The quadrupole mass spectrometer transmits ions of the selected mass to charge ratio. The ion detection system consists of a channel electron multiplier (CEM) operated in an ion counting mode and followed by a suitable amplifier and discriminator. Pulses from the detection system are then fed to a microprocessor controlled data acquisition unit (a multichannel analyzer). Data acquisition is completely controlled by a microcomputer, which also controls most other aspects of the instrument via an IEEE-488 interface.

3.2 Samples

Three zirconium standards (X-863, X-865, X-866), one Zircaloy standard (X-868), and one Zircaloy sample were certified by ICP-MS or

other suitable methods (OES, DCP) for this study. Samples were analyzed directly without major preparation other than machining and polishing one side of the sample surface to obtain a flat surface. The analytical samples were then surface cleaned by rinses in ethanol, dilute HNO_3, and deionized-distilled water. A preburning time in the Atomsource prior to the analysis provides a clean sample surface and a stable signal.

3.3 Analysis Procedure

In the ICP-MS experiment, 0.25 g of Zircaloy sample were dissolved in 25 mL of acid (2:1:40, $HF:HNO_3:H_2O$). A calibration standard solution containing several 0.1 μg/ml mono-isotopic elements (^{27}Al, ^{45}Sc, ^{55}Mn, ^{59}Co, ^{89}Y, ^{103}Rh, ^{139}La, ^{141}Pr, ^{169}Tm, ^{209}Bi) was also prepared for mass discrimination correction. The 1% sample solutions, the calibration solution, and the blank solution were mixed with 0.5 μg/mL of artificial ^{233}U for the internal standard. Each of the solutions was then mixed with 9 mL of deionized-distilled water, making a total dilution factor of 1,000.

4. Results and Discussion

4.1 Discharge Parameters

It is well known that a GDMS system is quite complex and a large number of variables can affect the measured ion signal. Therefore it

is first necessary to optimize the Atomsource parameters as was done in [206], and to set the MS parameters as recommended by the manufacturer. The discharge parameters were optimized to obtain the highest ion signal on ^{56}Fe for the low and middle mass ranges (4 to 130 m/z), and on ^{208}Pb for the high mass range (150 to 245 m/z).

Figure VI.1 shows the effect of sputtering time on five ion intensities. Ion intensities were obtained in 1.7 min (1024 channels, 200-μs dwell time per channel, 500 scans). It took 3 to 18 min to reach stable ion signals for 4 elements and 9 min for ^{40}Ar. This compares to a GDMS system developed by Jakubowski et al. [207] which requires a preburning time of 30 min to reach stable conditions for all elements.

The effects of pressure and current on ion intensities of six elements are shown in Figures VI.2 and VI.3. The general trend, in which both the current and pressure have an optimum region, is in agreement with results obtained in a previous paper [206]. One interesting result is that all elements (except ^{51}V) show an obvious maximum ion intensity around 26-28 mA (Figure VI.3) followed by a dip, a rise, and finally at 36 mA another dip.

Differences in the general shapes of the curves may be caused by changes in ionization mechanisms or efficiencies for the different isotopes as current changes. However, some of the points on the curves in Figures VI.1-3 show unusually large deviations from smooth lines; for example, in Figure VI.1 the point at 12 min for the Sn line and in Figure VI.3 the point at 28 mA for the V line. These deviations are much larger than instrumental noise. Since they occur in the time plot, Figure VI.1, and are not the same for all ions, they

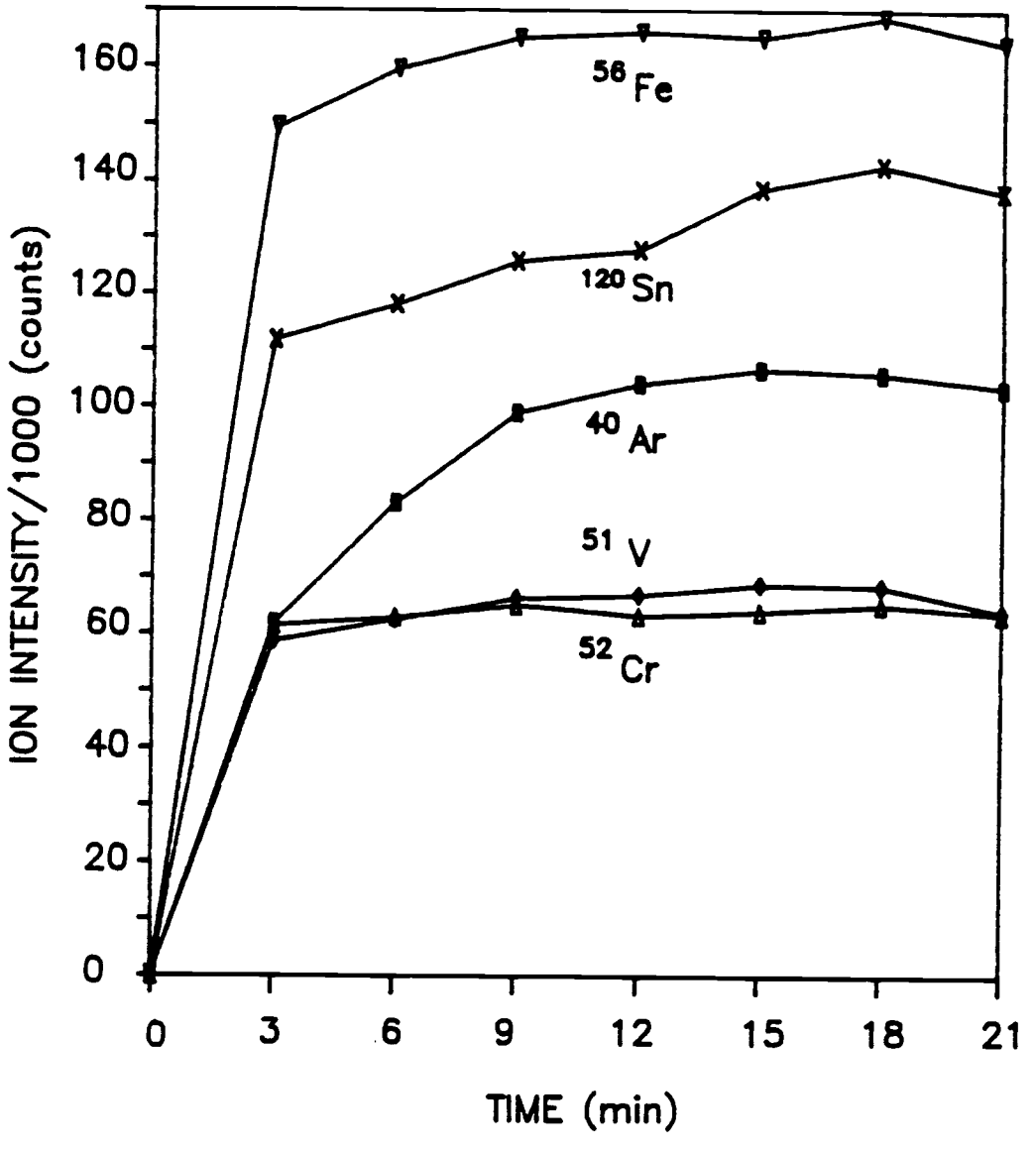

Figure VI.1 Effect of sputtering time on five ion intensities. Ion intensities were obtained in 1.7 min (1024 channels, 200-μs dwell time per channel, 500 scans). Operating conditions for the Atomsource were listed in Table VI.6.

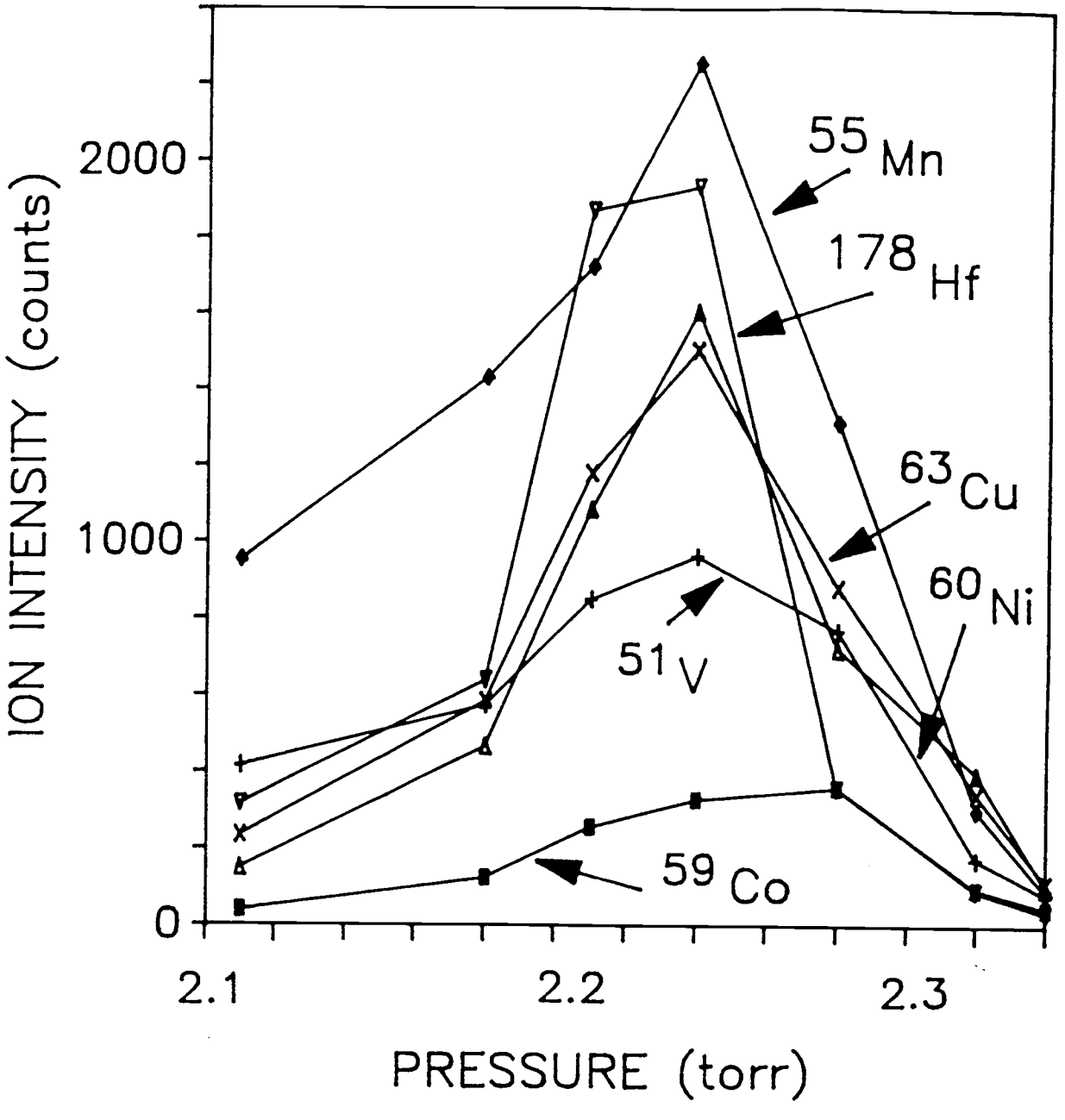

Figure VI.2 Effect of pressure on ion intensities of six elements. Ion intensities were obtained in 1.7 min (1024 channels, 200-μs dwell time per channel, 500 scans). Operating conditions for the Atomsource were listed in Table VI.7.

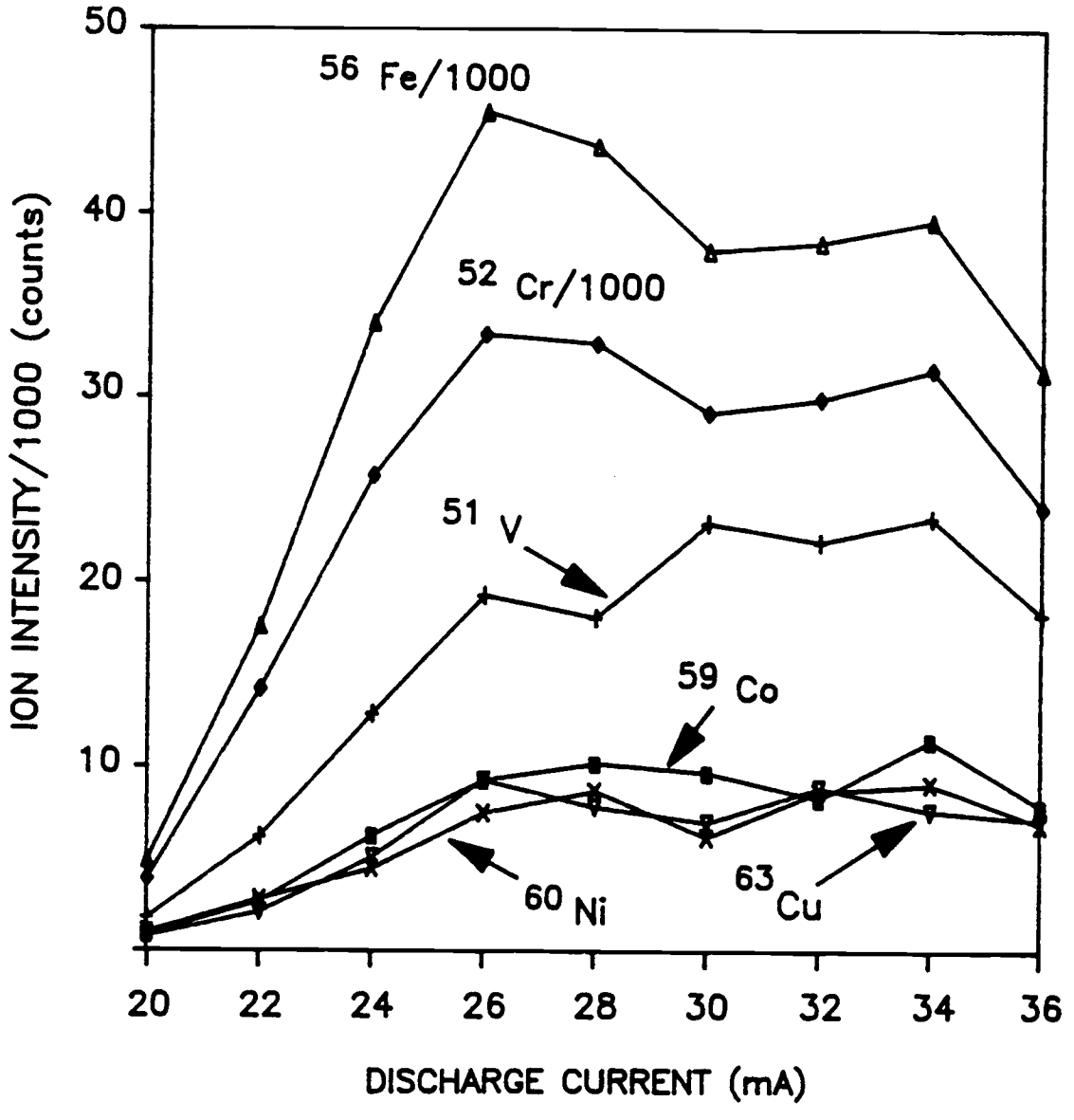

Figure VI.3 Effect of current on ion intensities of six elements. Ion intensities were obtained in 1.7 min (1024 channels, 200-μs dwell time per channel, 500 scans). Operating conditions for the Atomsource were listed in Table VI.8. Notice that the Fe and Cr intensities have been divided by 1000 to put them on scale.

are most likely due to heterogeneities (e.g., with depth) in the sample, rather than to discontinuities in ionization mechanisms caused by changes in pressure or current. Sample heterogeneities of this magnitude indicate the desirability of spatial integration when determining concentrations. The faster sampling rate of the Atomsource [205] relative to ordinary glow discharges is therefore an advantage.

4.2 Background and Memory Effect

The ICP-MS shows two different types of background: (1) a mass independent background above 80 m/z, due to photons in the uv and low energy X-ray region of the electromagnetic spectrum [208], and (2) minor molecular peaks and contamination at the sub-ppb level, which often exceed the instrumental background at lower mass ranges. Similar backgrounds are observed for the Atomsource-MS, at low mass ranges when operating the Atomsource with low current to avoid sputtering.

The Atomsource-MS used in this study exhibits mass-indepenendent background levels from a range of 1 to 50 apparent ions/s per channel, depending on the experimental parameters. This background level is comparable to a range of 1 to 20 apparent ions/s obtained with the ICP-MS [208]. In addition, molecular species from argon gas and from the sample form molecular ions at specific masses. This will be discussed in more detail later.

One of the questions regarding the Atomsource-MS is whether this system has a memory effect. Memory effects have been reported in the

ICP-MS due to residual ions trapped in the boundary layer around the sampling cone or on the walls of the glass introduction system [8,9]. It was suspected that the sputtered material deposited on the inside of the glow discharge cell might cause a memory effect.

To investigate the memory effect, a low alloy steel was run after one hour of running with a Zircaloy sample. Although zirconium deposits were observed inside the Atomsource, especially on the quartz tube insert, no zirconium isotope peaks were observed. It is therefore concluded that memory effects are negligible for this type of sample for the Atomsource.

4.3 Spectral Interferences

For the ICP-MS there are three types of spectral interference which must be considered. These are ions from the argon plasma and common background gases (e.g., N_2, O_2, H_2O, CO_2), ions from chemical reagents (e.g., acids), and true isobaric interferences [210]. When a typical solid sample is used there is no interference from chemical reagents in a GDMS since the sample is directly introduced without dissolution in chemical reagents. Surface contamination caused by surface preparation is eliminated during the preburn.

Polyatomic interference is the most common in both ICP-MS and GDMS. This consists of background gases and molecular combinations of sample constituents with matrix elements and/or the discharge gases.

Isobaric interferences are few and seldom troublesome in the GDMS as well as the ICP-MS. For instance, there are three isotopes of Ti,

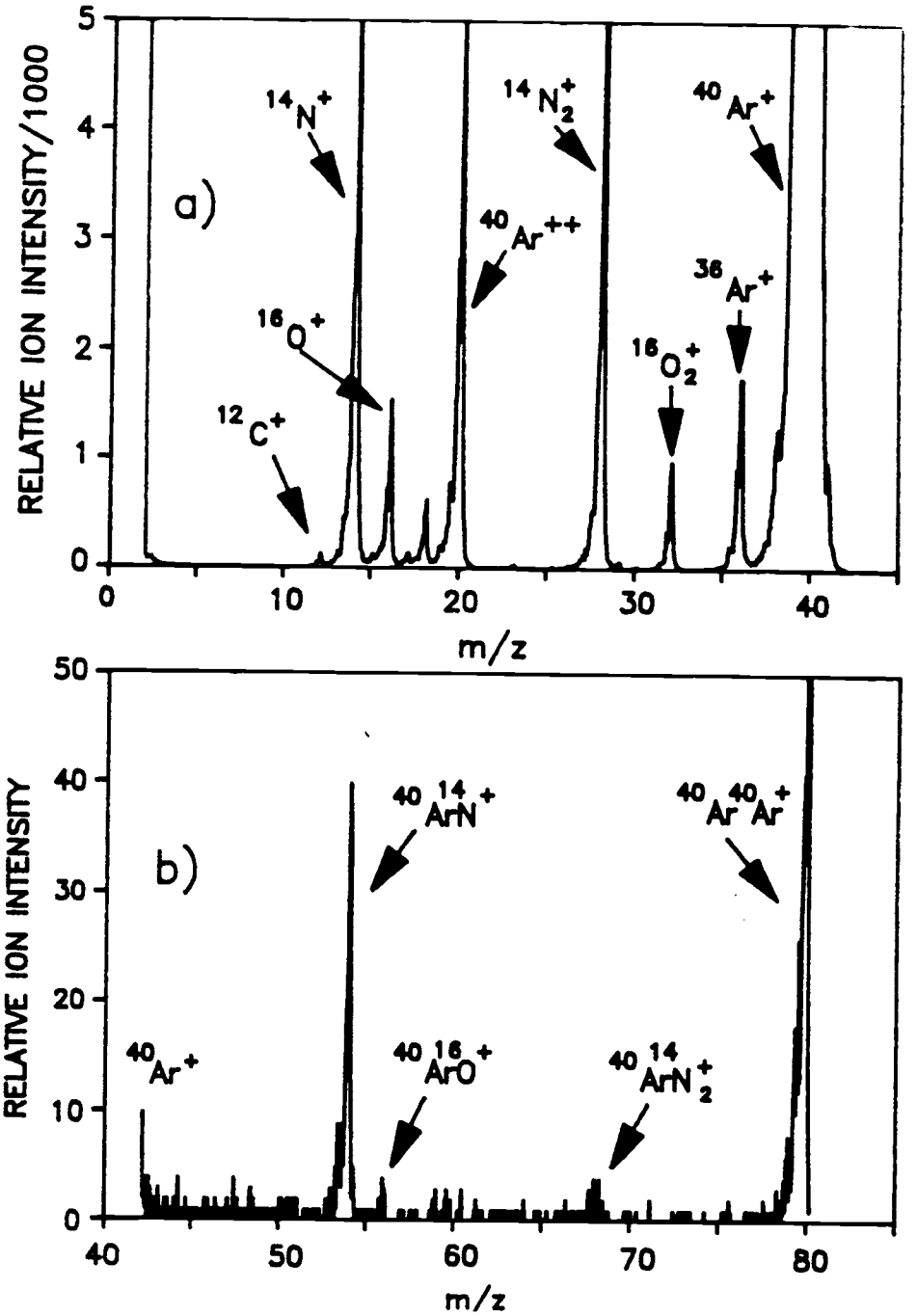

Figure VI.4 Spectra obtained at 1.4-mA discharge current, 669-V discharge voltage, 0.6 L/min gas flow rate, 1-torr pressure in the Atomsource cell, and 0.29-torr pressure in the first stage of the mass spectrometer. Ion intensities were obtained in 1.7 min (1024 channels, 200-μs dwell time per channel, 500 scans).

V, and Cr at mass 50, but each of these elements has other isotopes free of isobaric interference [203].

To investigate spectral interferences originating from common background and plasma gases, the discharge was operated at a current low enough to avoid sputtering. Figure VI.4 shows the spectra obtained at 1.4-mA discharge current, 669-V discharge voltage, 0.6 L/min gas flow rate, 1-torr pressure in the Atomsource cell, and 0.29-torr pressure in the first stage of the mass spectrometer. Figure VI.4a shows the spectrum covering the mass range between 2 and 40 m/z, and Figure VI.4b is scale expanded by a factor of 100 and covers the mass range between 40 and 80 m/z. A detailed tabulation of the background species is presented in Table VI.1. As expected, the $^{40}Ar^{+}$ major peak is obvious and an $^{36}Ar^{+}$ (0.34% natural abundance) minor peak is also observed. The doubly charged $^{40}Ar^{++}$ ion is also present. The background spectra for the Atomsource-MS are relatively simple in comparison to the ICP-MS background spectra obtained from distilled water [211]. Possible sources of $^{14}N^{+}$ and $^{16}O^{+}$ (observed in the same ratio as in air) in the Atomsource-MS are air leakage, gas desorption from the surfaces, or contamination of the argon. The argon was checked by an oxygen meter and found to contain less than 1 ppm oxygen. No significant background ion peaks are observed in the mass range between 40 and 80 m/z except $^{40}ArN^{+}$ and $^{40}Ar^{40}Ar^{+}$ as shown in Figure 4b. $^{40}ArO^{+}$ and $^{40}ArN_2^{+}$ peaks are barely seen and less than 10 counts/s. Thus the potential interference from $^{40}ArO^{+}$ for $^{56}Fe^{+}$ is negligible in the Atomsource-MS. When acid is used for dissolving the sample in the ICP-MS, a more complex background spectrum is obtained. For

Table VI.1 Background ions observed from the plasma gas and other background gases in a low-current discharge.

Mass(m/z)	Identification	Intensity(counts/for 1-s integration time)
12	$^{12}C^+$	998
14	$^{14}N^+$	22988
16	$^{16}O^+$	6479
17	$^{16}OH^+$	1940
18	$^{16}OH_2^+$, $^{18}O^+$	3570
20	$^{40}Ar^{++}$	19315
23	^{23}Na	125
28	$^{14}N_2^+$, $^{12}C^{16}O^+$	31270
29	$^{14}N^{15}N^+$, $^{14}N^{14}NH^+$	355
30	$^{14}N^{16}O^+$	147
32	$^{16}O_2^+$	4821
36	$^{36}Ar^+$, $^{18}O_2^+$	8282
38	$^{38}Ar^+$	610
40	$^{40}Ar^+$	898160
41	$^{40}ArH^+$	5451
44	$^{12}C^{16}O_2^+$	17
54	$^{40}Ar^{14}N^+$	157
56	$^{40}Ar^{16}O^+$	13
68	$^{40}Ar^{14}N_2^+$	17
80	$^{40}Ar_2^+$	393

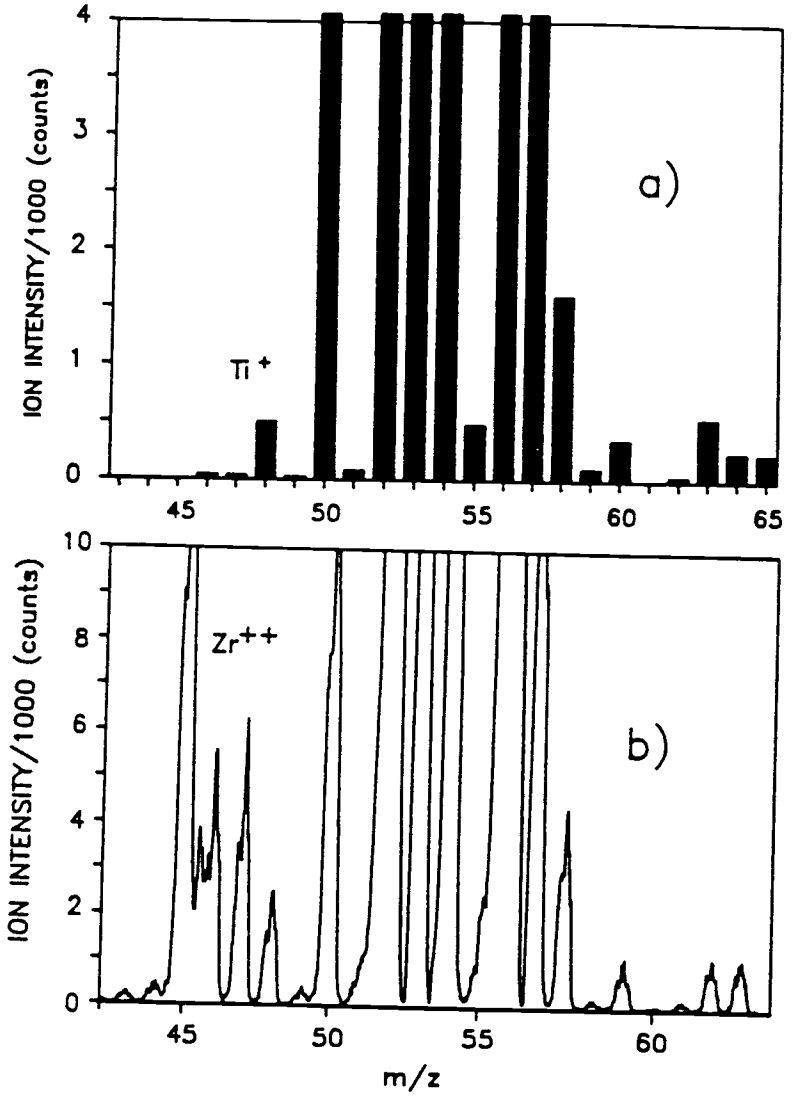

Figure VI.5a A computer simulated spectrum of this Zircaloy sample that omits doubly charged ions.

Figure VI.5b Spectra obtained from a Zircaloy sample between 45 and 65 m/z intended for determination of transition elements. Ion intensities were obtained in 1.7 min (1024 channels, 200-μs dwell time per channel, 500 scans). Operating conditions for the Atomsource were listed in Table VI.9.

example, background spectra for 5 % hydrochloric acid show species such as Cl^+, ClO^+, ClN^+, Cl_2^+, and $ArCl^+$. These species significantly increase the complexity of the background, particularly when all isotopic combinations are considered. Also, contamination of the acid cause problems in the ICP-MS.

Metal oxide ions and doubly charged ions are also major interferences in a Zircaloy analysis. Figure VI.5b shows the spectra obtained from a Zircaloy sample between 45 and 65 m/z intended for determination of transition elements. All adjacent peaks with intensities in the same order of magnitude are well resolved with the exception of those between 45 and 46 m/z. The lack of baseline resolution is evidence that a peak exists at 45.5 m/z, most likely originating from doubly charged ^{91}Zr. Figure VI.5a shows a computer simulated spectrum of this Zircaloy sample that omits doubly charged ions. The peaks in Figure VI.5b at 45, 45.5, 46 47 and 48 are most likely doubly charged Zr ions of mass 90 (51.4%), 91 (11.2%), 92 (17.1%), 94 (17.5%), and 96 (2.8% natural abundance) with some contribution from the Ti isotopes of mass 46 (8.0%), 47 (7.5%), 48 (73.7).

In the ICP-MS, metal oxide formation results from reactions between metal ions and atomic oxygen [208]. Figure VI.6 shows the spectra obtained from the Zircaloy sample during the early parts of this project when an air leak was present. This spectrum shows the major peaks of zirconium from 90 to 96 m/z. A series of zirconium oxide peaks, which could cause serious interference in the high mass range, were observed from 106 to 112 m/z (ZrO), 122 to 128 m/z (ZrO_2) and (barely visible in the figure) 138 to 142 m/z (ZrO_3).

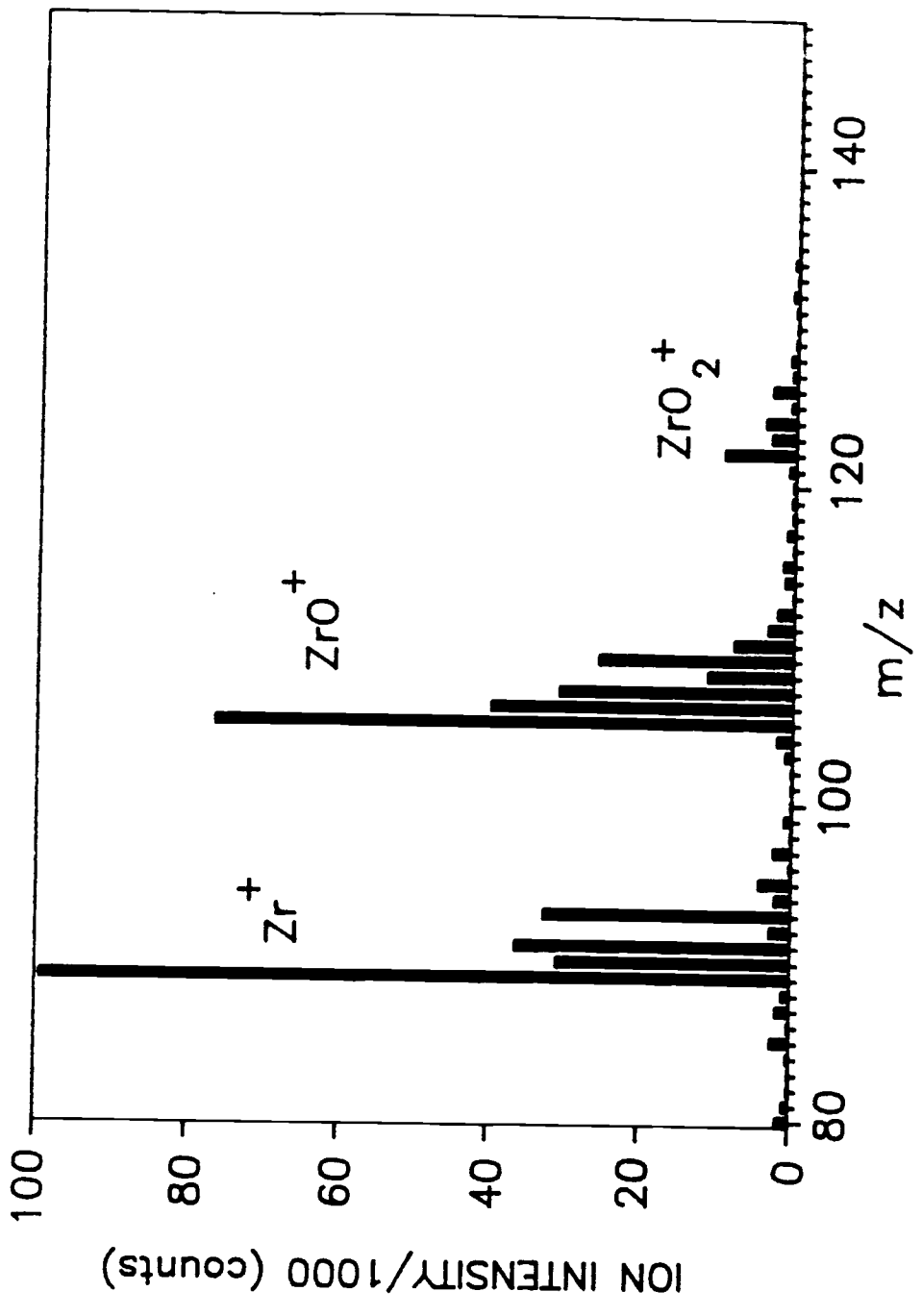

Figure VI.6 Spectra obtained from the Zircaloy sample during the early parts of this project when an air leak was present. Ion intensities were obtained in 1.7 min (1024 channels, 200-μs dwell time per channel, 1000 scans). Operating conditions for the Atomsource were listed in Table VI.9.

The series of zirconium oxide peaks of ZrO_2 and ZrO_3 disappeared, and the ZrO peaks became much lower when the leak was fixed.

4.4 Reproducibility

Table VI.2 is a comparison of the different relative standard deviations (RSD's) obtained for Zircaloy. Column "R-A" indicates the ion intensity repeatability without changing the sample, and values range from 1 % to 6 %. The average RSD for 10 isotopes was 4 %. Column "R-C" was obtained by changing the sample position between the measurements. Some of the values are higher than "R-A", but most of values are comparable except ^{120}Sn. In SSMS, this deviation is often greater due to sample inhomogeneities [207], whereas for the GDMS the effect is expected to be reduced because a larger volume is sampled.

An attempt to improve precision was made by using the ^{56}Fe ion as an internal standard, that is, the dependent variable was calculated by dividing the analyte intensity by the ^{56}Fe intensity in each sample position. Columns "R-B" and "R-D" show the relative precision when this internal standard method was used. The averages for column "R-B" and "R-D" were 2 % and 5 %, respectively.

Column "R-E" shows the RSD calculated from counting statistics, that is, the inverse of the square root of the total counts. These numbers estimate the best precision obtainable.

To compare the RSD's the statistical F-test procedure outlined in NBS Handbook 91 was performed [212] using the assumption that the

Table VI.2 Comparison of different relative standard deviations (%) obtained for a Zircaloy sample.

Element	R-A Sample Stationary	R-B	R-C Sample Moved	R-D	R-E Counting Limit
^{27}Al	1 %	2 %	4 %	8 %	2 %
^{30}Si	2	1	5	12	1
^{48}Ti	4	6	7	5	5
^{51}V	2	2	9	4	4
^{52}Cr	6	1	9	4	0.2
^{56}Fe	4	-	12	-	0.2
^{60}Ni	9	5	9	6	6
^{63}Cu	5	2	7	7	6
^{120}Sn	4	1	12	5	0.2
^{180}Hf	6	5	12	6	5
AVG %RSD :	4	3	9	6	3

Note: Each entry represents a RSD calculated from 3 measurements.

Key: R-A, %RSD of ion intensities obtained without moving the sample, and R-C when the sample was moved between measurements; R-B and R-D correspond to R-A and R-C respectively, but ion intensities were first divided by the ^{56}Fe ion intensity for each sample position; R-E = 100 × counts$^{-½}$

RSD's are statistically distributed in [approximately] the same manner as the standard deviations. (This assumption should cause little error since the scatter of the standard deviation is much greater than the scatter of the mean used to calculate the RSD; the mean is simply a scaling factor that normalizes the standard deviations so that they can be compared.) First, the level of significance of the test, α, was chosen as 0.05. Then $F_{1-\alpha/2}$ for (2,2) degrees of freedom was obtained from Table A-5 of NBS Handbook 91. This value from the handbook table and its inverse were compared to the square of the ratios, F, of the two RSD's being compared. If $F > F_{1-\alpha/2}(2,2) = 39$ or $F < 1/(F_{1-\alpha/2}(2,2)) = 0.025$, it is decided that the two methods for which the RSD's were calculated differ with regard to their RSD's.

Table VI.3 lists the F values for each of the values in the other columns in table VI.2 standard compared to the corresponding values in column (R-A). Since most of the F values lie within the limits of standard method, $39 > F > 0.025$, it is concluded that the numbers in each row in columns R-B through R-D could come from methods that have the same standard deviation as the method in column R-A. That is, these numbers do not prove that using the internal standard method, or moving the sample produces any changes in the precision (although a more detailed study may show a difference). Later we will see that the internal standard method does improve the accuracy, however.

4.5 Mass Discrimination

When a multielement scan is run, the mass spectrometer is optimized by maximizing the intensity with one ion. However, the ion

Table VI.3 Calculated $F = (s^2_A/s^2_B)$ values for the RSD's in columns R-B through R-D relative to column R-A in Table 2.

Elements	F_B	F_C	F_D
^{27}Al	0.25	0.063	0.02
^{30}Si	4.0	0.16	0.03
^{48}Ti	0.44	0.32	0.64
^{51}V	1.0	0.05	0.25
^{52}Cr	36	0.44	2.25
^{56}Fe	-	0.11	-
^{60}Ni	3.24	1.0	2.25
^{63}Cu	6.25	0.51	0.51
^{120}Sn	16	0.11	0.64
^{180}Hf	1.44	0.25	1.0

intensities of all ions vary in accordance with the ion selected for optimization. Different sensitivities for different masses are due to differences in ion transmission and detection efficiencies that vary when the ion focusing lenses are adjusted during the optimization procedure. In the ICP-MS, mass discrimination has been observed to be significant [213-217]. To obtain accurate multielement determinations, it is helpful to adjust the mass discrimination factor so that the mass spectrometer sensitivity is relatively constant over the mass range of interest.

To study mass discrimination, the mass spectrometer was adjusted for maximum intensity for ^{12}C, and subsequently for ^{27}Al and ^{56}Fe. After each optimization the ion intensities of ^{27}Al, ^{52}Cr and ^{56}Fe were obtained. All ion intensities were then adjusted for concentration and natural abundances. Thus all adjusted ion intensities should be the same if there is no mass discrimination. Figure VI.7 shows the mass discrimination results for the Zircaloy sample for the multielement scan mass range between 26 and 56 m/z. Notice that the adjusted ion intensities change significantly over the mass range when ^{12}C and ^{27}Al are used as optimizing elements, but they do not change as much when ^{56}Fe is used as the optimizing element. Therefore, for this mass range ^{56}Fe may be a good choice for the optimizing element.

4.6 Detection Limit

Table VI.4 is a comparison of Atomsource-MS and ICP-MS detection limits in single ion monitoring and multielement monitoring

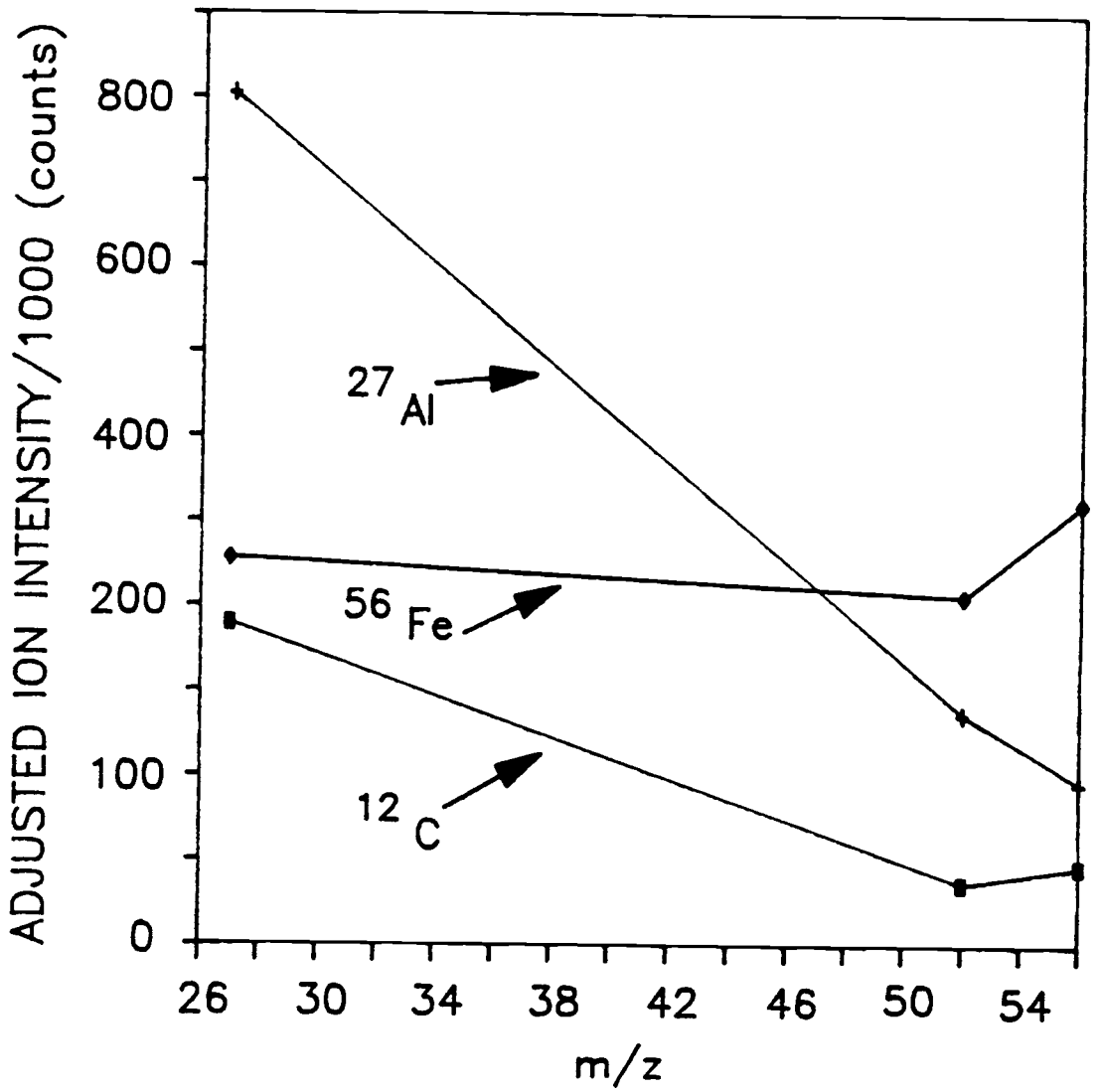

Figure VI.7 Mass discrimination results for the Zircaloy sample for the multielement scan mass range between 26 and 56 m/z. (1024 channels, 200 μs dwell time per channel, 1000 scans). Operating conditions for the Atomsource were listed in Table VI.9.

Table VI.4 Comparison of detection limits (3 σ).

Element	Atomsource-MS(μg/g)		ICP-MS(ng/ml)		ICP-MS(ng/ml)
	Single-element[a]	Multi-element[b]	Single-ion	Multi-element	Single-ion[f]
Al(27)	-	0.03	0.3[c]	-	0.1
Fe(56)	-	0.008	0.5[c]	-	0.2
Ti(49)	-	0.006	-	0.5[d]	0.06
V(51)	-	0.007	-	0.3[d]	0.03
Cr(52)	-	0.01	0.06[d]	0.7[d]	0.02
Mn(55)	-	0.02	0.1[d]	1.1[d]	0.04
Ni(60)	-	0.01	0.1[e]	-	0.03
Cu(63)	-	0.009	0.3[c]	-	0.03
Zn(66)	-	0.008	0.2[e]	1.0[e]	0.08
Hf(178)	-	0.03	-	-	0.03
Sn(120)	-	0.05	0.06[d]	1.2[d]	0.03
W(184)	0.02	0.4	0.05[d]	0.3[d]	0.06
Pb(208)	0.01	0.4	0.05[d]	1.5[d]	0.05
U(238)	0.008	0.04	0.03[d]	0.1[d]	0.02

[a]; 20-s integrations

[b]; 1.6-s integrations

[c]; from reference 213, 10-s integrations

[d]; from reference 218, single ion values from 10-s integrations, multielement values from 0.12-s integrations

[e]; from reference 214, 10-s integrations

[f]; VG PlasmaQuad ICP-MS, single ion values from 10-s integrations

determinations. Theoretical detection limits in both methods are calculated by dividing 3 x standard deviation of the background by the slope of a two-point calibration curve (the first point being the background average, designated as zero concentration).

In single-element monitoring, a range of only a few mass numbers is scanned that includes all isotopes of the element. Typically a range of 10 mass units is scanned in 3.4 min (1024 channels, 200-μs dwell time per channel, 1000 scans). Figures VI.8 through VI.10 show the spectra obtained for Pb, W, and U with the single-element monitoring method using the Atomsource-MS. Detection limits for three elements (^{184}W, ^{208}Pb, and ^{238}U) were determined with 102 channels for the analyte ion isotope and another 102 channels for the background, 20-s total integration time. The standard deviation of the background was obtained by taking the square root of the total counts on the background 102 channels. Detection limits of those three elements are 0.02, 0.01 and 0.008 μg/g, respectively.

In ICP-MS the detection limits by Gray [214,218] were determined with single ion monitoring by setting the analyser to the relevant mass and making 10 or more integrations of the blank level for 10-s each, followed by a 10-s integration on a 100 ng/ml or 1 μg/ml solution of the element. For the multielement determination [218] the system was tuned up on $^{115}In^{+}$, and the scan set from 4 to 250 m/z using 2000 channels (200 μs dwell time per channel, 1000 scans).

To determine the detection limits of the transition elements with a multielement scan, the Atomsource-MS was optimized with ^{56}Fe, and the scan run from 4 to 130 m/z using 1024 channels (200-μs dwell time per channel, 1000 scans). Background ion intensities were obtained

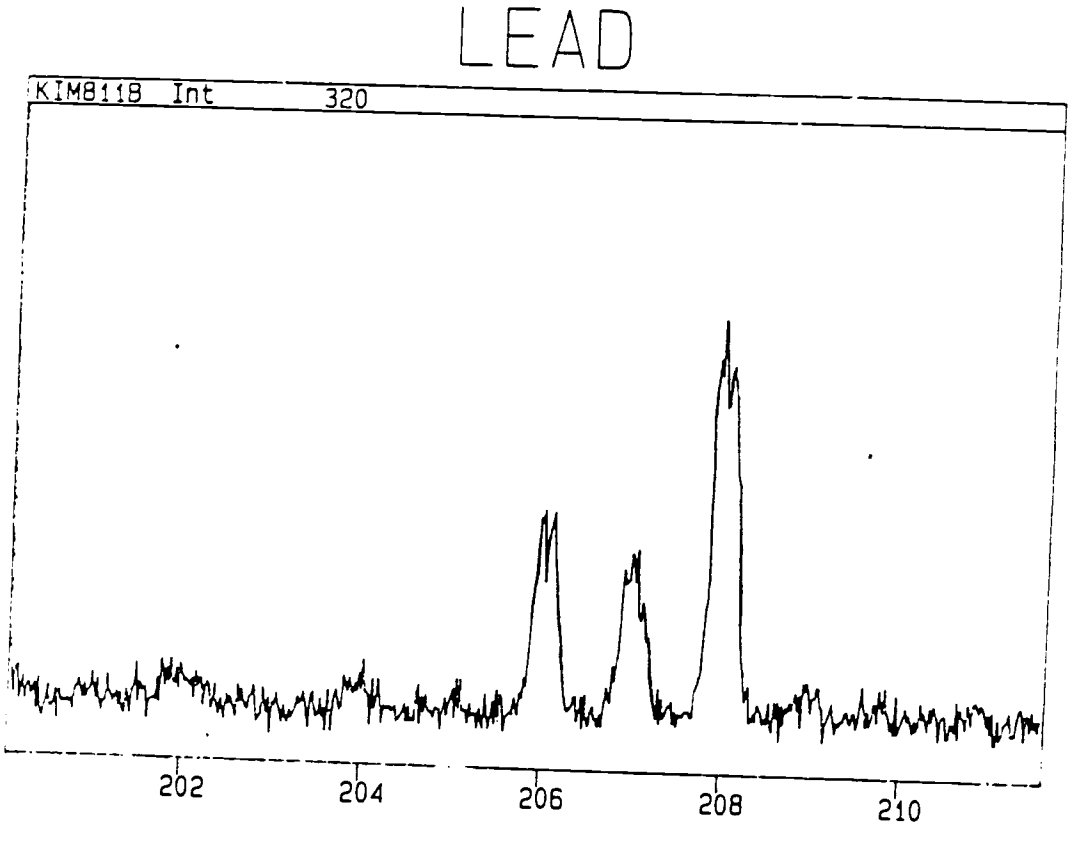

Figure VI.8 Spectra obtained for Pb with the single ion monitoring (1024 channels, 200 μs dwell time per channel, 1000 scans). Operating conditions for the Atomsource were listed in Table VI.9.

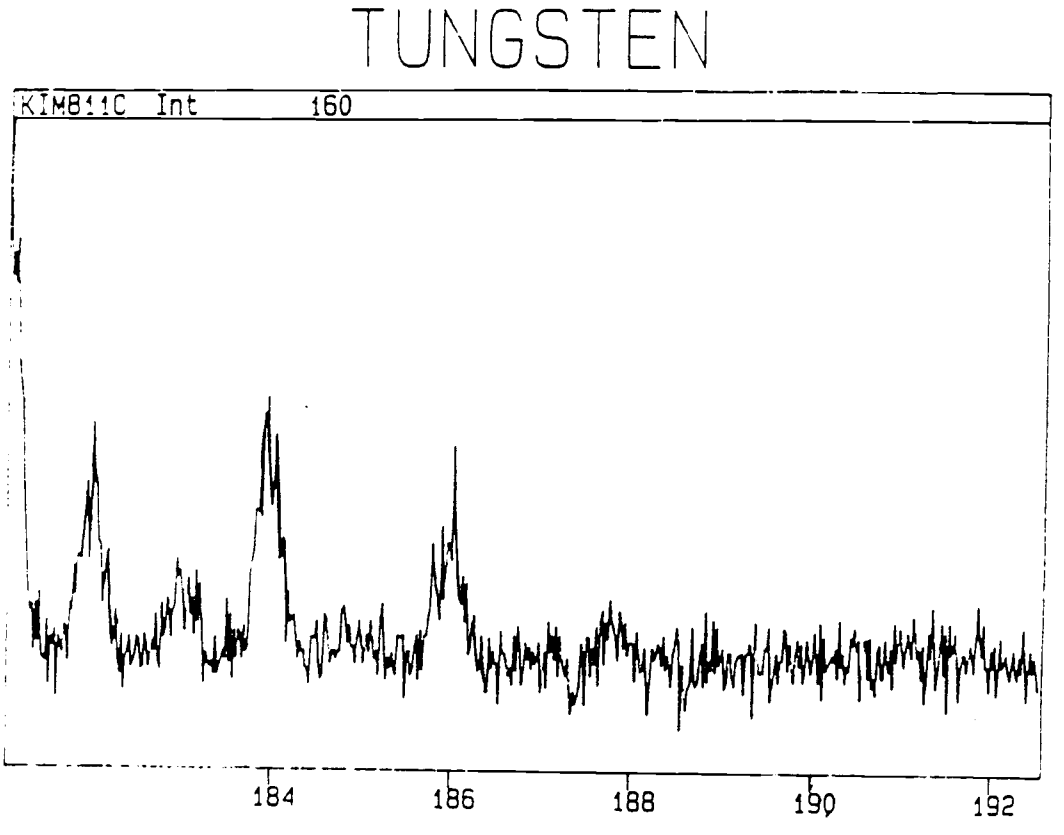

Figure VI.9 Spectra obtained for W with the single ion monitoring (1024 channels, 200 μs dwell time per channel, 1000 scans). Operating conditions for the Atomsource were listed in Table VI.9.

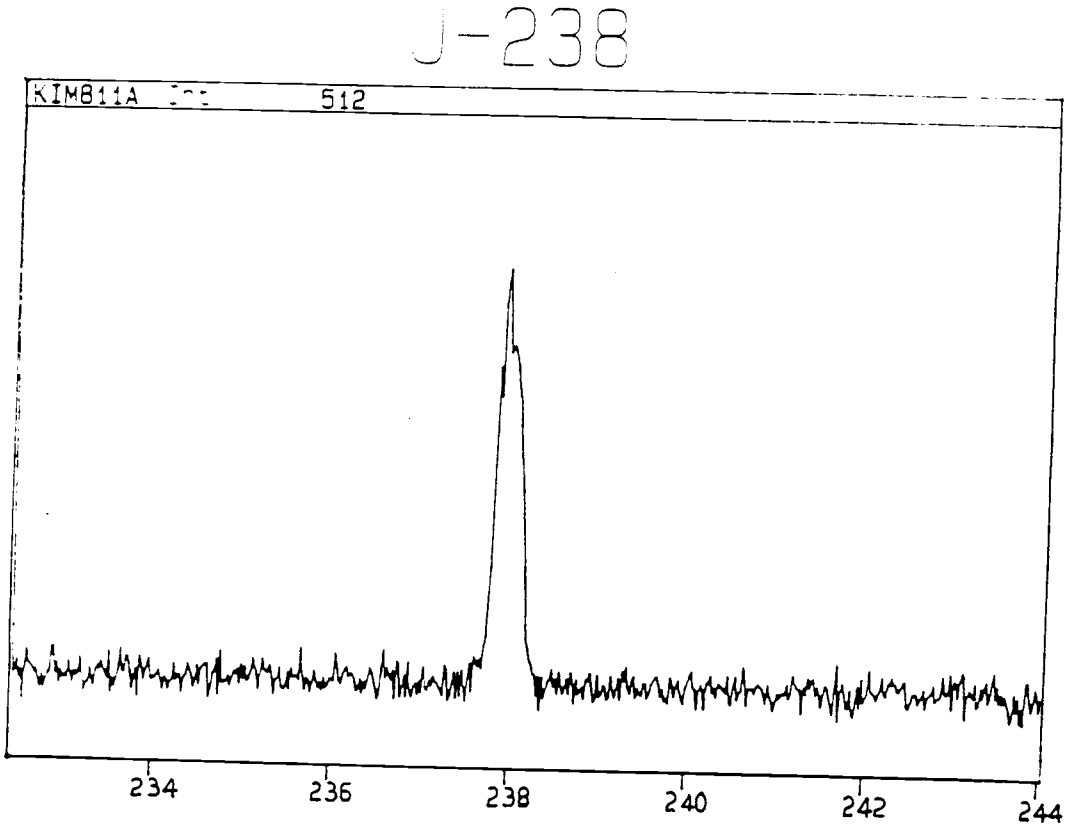

Figure VI.10 Spectra obtained for U with the single ion monitoring (1024 channels, 200 μs dwell time per channel, 1000 scans). Operating conditions for the Atomsource were listed in Table VI.9.

from the scan range 69 to 73 m/z and from 81 to 84 m/z where there were no interfering ions. Ga (69 and 71) and Ge (70, 72 and 73) and Kr (82, 83 and 84) ions were not detectable (i.e., Ga, Ge and Kr are certified as < 10 ppb). The standard deviation of the background was calculated as the square root of an integration on 8 channels. The detection limits for the transition elements are between 0.006 and 0.01 μg/g.

A similar set of runs was made with the system optimized on ^{208}Pb for a high mass range (173 to 245 m/z) for comparison with single ion monitoring. In this mass range the blank ion intensities were relatively easy to choose compared to the mass range between 4 and 160 since there was no molecular interference and, for some of the mass range, no natural isotopes are present (210 to 231 m/z).

For the most part, the multielement detection limits were about an order of magnitude worse than the single element values. The detection limits for the elements in Table VI.4 are between 0.006 to 0.4 μg/g, which are better than the ICP-MS when its detection limits are based on the original solid sample (the solid D.L. is calculated by dividing the solution D.L. by the dilution factor 1 x 10^{-3}[219]).

4.7 Analysis of Zircaloy

For the determination of Zircaloy samples with the internal and external standard methods, the calibration curves were obtained by using the three zirconium standards (X-863, X-865, X-866), one Zircaloy standard (X-868), and one Zircaloy sample. Each of the samples was run at three different mass ranges with multielement

monitoring. In the low mass range, the spectrum was obtained in 1.7 min (1024 channels, 200-μs dwell time per channel, 500 scans), covering the 5 to 61 m/z range. In the middle masses the spectrum covered the 39 to 123 m/z range, and for the high masses the spectrum covered the range between 150 and 245 m/z. To minimize mass discrimination the ^{56}Fe ion was chosen for the optimizing element at the low and mid mass ranges, and ^{208}Pb was chosen for the high mass range.

For the external standard method, the calibration curves were obtained by plotting the ion intensity of each element vs. the concentration of that element, the crosses in Part B of Figures VI.11 to VI.22.

For the internal standard method, the ^{57}Fe ion was chosen for the internal standard element mass range from 5 to 123 m/z, and ^{181}Ta was chosen for the mass range from 150 to 245 m/z. The calibration curves for the internal standard method were prepared in which the ratio of the analyte signal to internal standard signal ($S_a/S_{int.}$) is plotted vs. the analyte concentration to internal standard concentration ($C_a/C_{int.}$). Part A of Figures VI.11 to VI.22 shows the internal standard calibration plot.

The other calibration curves for the internal standard method were prepared in which the ratio of the analyte signal to internal standard signal times the internal standard concentration (Sa x $C_{int.}/S_{int.}$) is plotted vs. the analyte concentration. The filled squares in Part B of each figure show these curves scaled up so they can be plotted on the same scale as the plot of relative intensity vs. concentration of the element.

Figures VI.11 and VI.12 show the calibration curves for ^{27}Al and ^{30}Si. There is no apparent relationship between the ion intensity and the concentration. Minor sputtering of the Al sampling cone may interfer with the Al results. For the determination of Si ion, the major peak of ^{28}Si (92.2 % isotope abundance) is not used because of the interference from $^{14}N_2$, and with the minor peak of ^{30}Si (3.1 % isotope abundance) may also be interfered with by $^{14}N^{16}O$. However, the reasons for those results are not clear and further studies are needed.

Figures VI.13 through VI.22 show the calibration plots for ^{49}Ti, ^{51}V, ^{52}Cr, ^{55}Mn, ^{59}Co, ^{60}Ni, Hf_{178}, ^{184}W, ^{208}Pb, and ^{238}U. In general, the internal standard method, which plots the ratio of analyte signal to internal standard signal multiplied by the concentration of the internal standard vs. the concentration of analyte, improves the linearity. Thus, this method was used for an analysis of the Zircaloy sample. With the availability of an ion detector with a larger dynamic range, a Zr ion would be used as an internal standard since the concentration of Zr is usually known in a Zr sample. In this study the Zr ions were skipped so as not to overload the detector.

To simulate the analysis of a real sample, the Zircaloy sample was analyzed as an "unknown" while using the other standards for calibration. The calibration was performed with a linear regression forced through the origin because most concentrations in the sample were closer to the origin than the standards. Corresponding confidence limits were obtained from the standard error of the fit using the procedure outlined on page 5-25 of NBS Handbook 91. The

results are summarized in Table VI.5. The results indicated that with this internal standard method an analysis of Zircaloy sample for some elements is possible within an accuracy of 10 %. The successful determination of 10 Zircaloy trace elements demonstrates that a gas-jet enhanced sputtering system such as the Atomsource is a useful ion source for mass spectrometry.

5. Acknowledgment

We gratefully acknowledge a grant from Teledyne Wah Chang Albany and the loan of the Atomsource by Analyte Corporation.

Table VI.5 Comparison of certified analysis and Atomsource-MS analysis by internal standard method of Zircaloy samples

Element	Certified (μg/g)	Determined (μg/g)
Co[b]	(< 5.0)[d]	0.8 ± 0.3
Cr[b]	1126 ± 32	1330 ± 140
Hf[c]	47 ± 2	38 ± 0.6
Mn[b]	(< 5.0)[d]	7.4 ± 0.2
Ni[b]	8.6± 1	11 ± 1
Pb[c]	1.4 ± 0.1	1.4 ± 0.1
Ti[b]	7.0 ± 2	10 ± 2
V[b]	(< 5.0)[d]	6.6 ± 0.6
W[c]	1.2 ± 0.1	2.0 ± 0.4
U[c]	0.38 ± 0.04	0.4 ± 0.1

a; Low mass scan (5 to 61 m/z), ^{57}Fe for internal standard

b; Mid mass scan (39 to 123 m/z), ^{57}Fe for internal standard

c; High mass scan (150 to 245 m/z), ^{181}Ta for internal standard

d; Value not certified

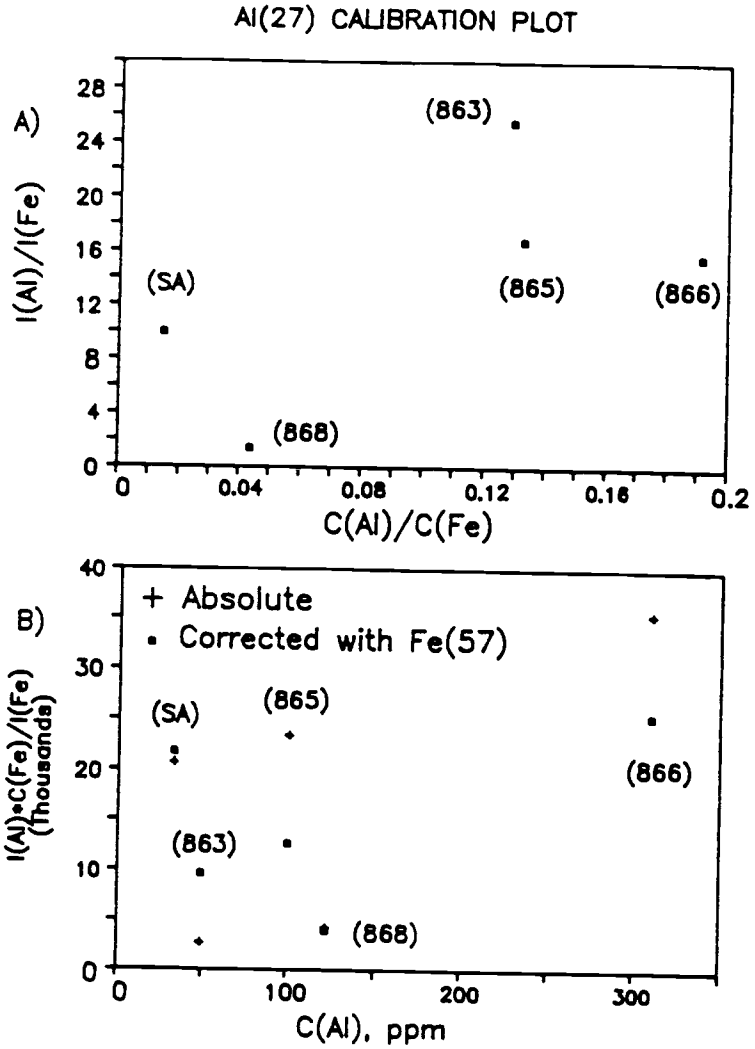

Figure VI.11 Calibration plots for ^{27}Al; A) calibration plot using internal standard ratio method.; B) filled squares, ion intensity vs. concentration, B) crosses, calibration plot with intensity scaled by the internal standard concentration/intensity ratio. Operating conditions for the Atomsource were listed in Table VI.10.

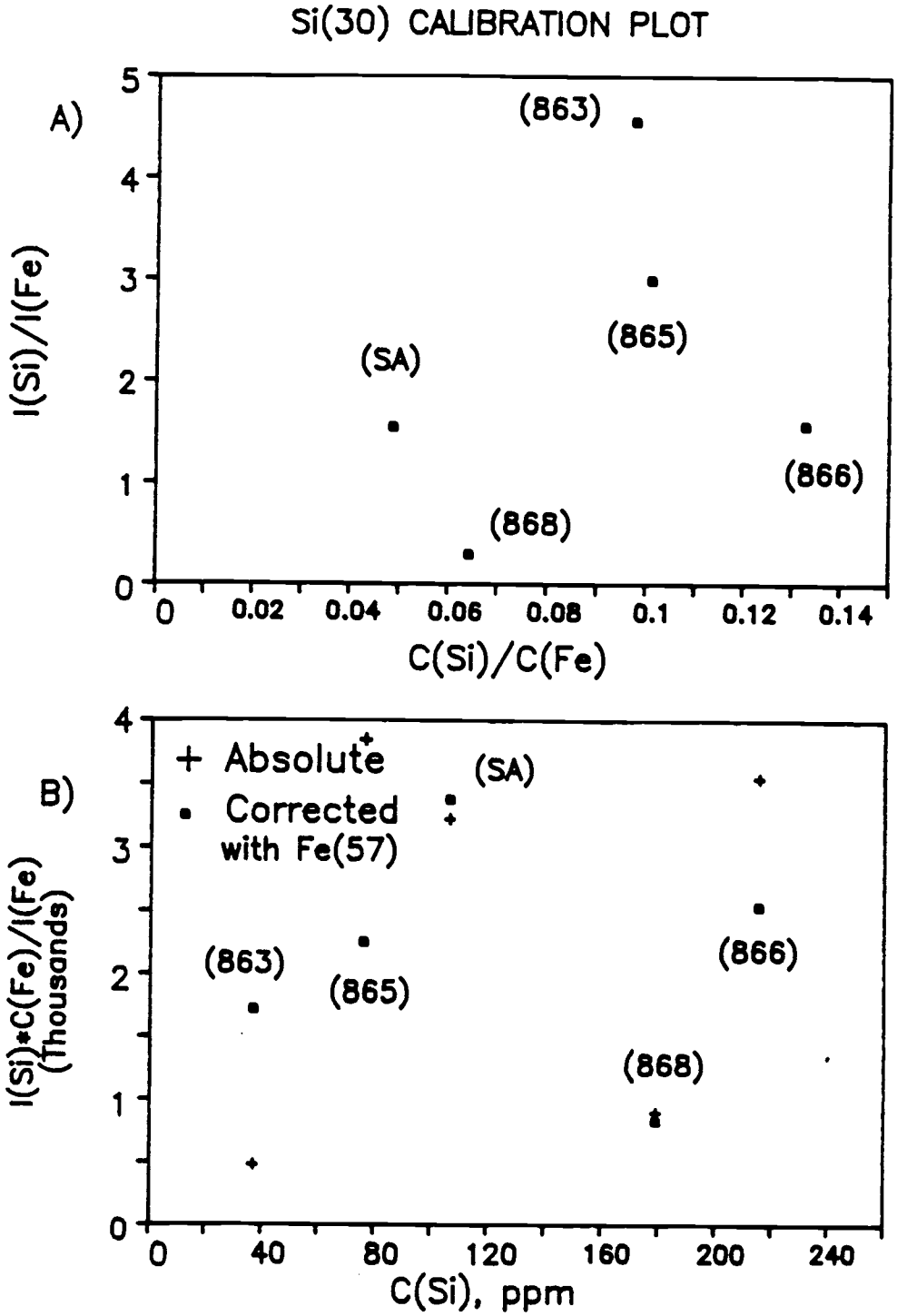

Figure VI.12 Calibration plot for ^{30}Si, see Figure VI.11 for explanation. Operating conditions for the Atomsource were listed in Table VI.10.

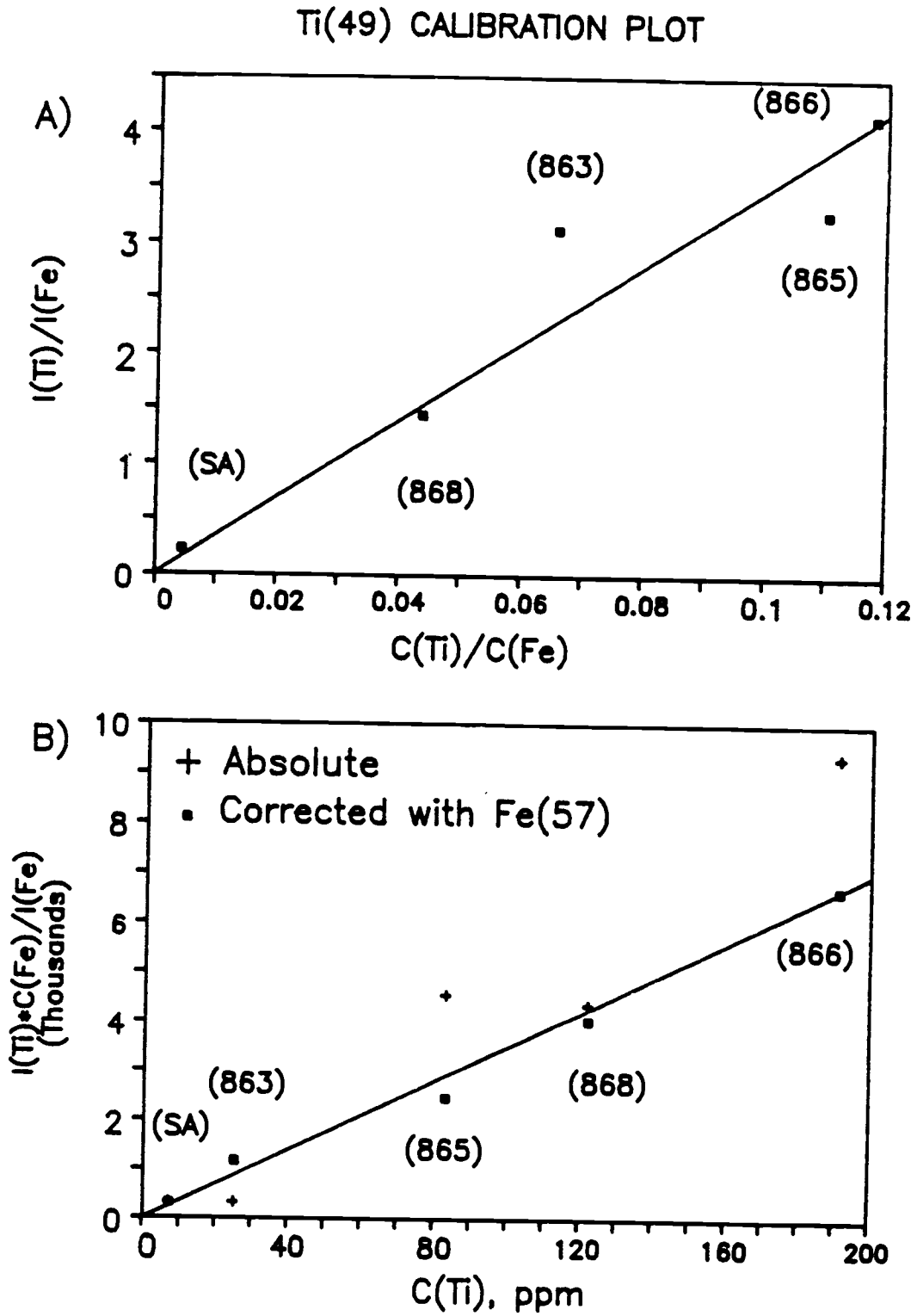

Figure VI.13 Calibration plot for ^{49}Ti, see Figure VI.11 for explanation. Operating conditions for the Atomsource were listed in Table VI.10.

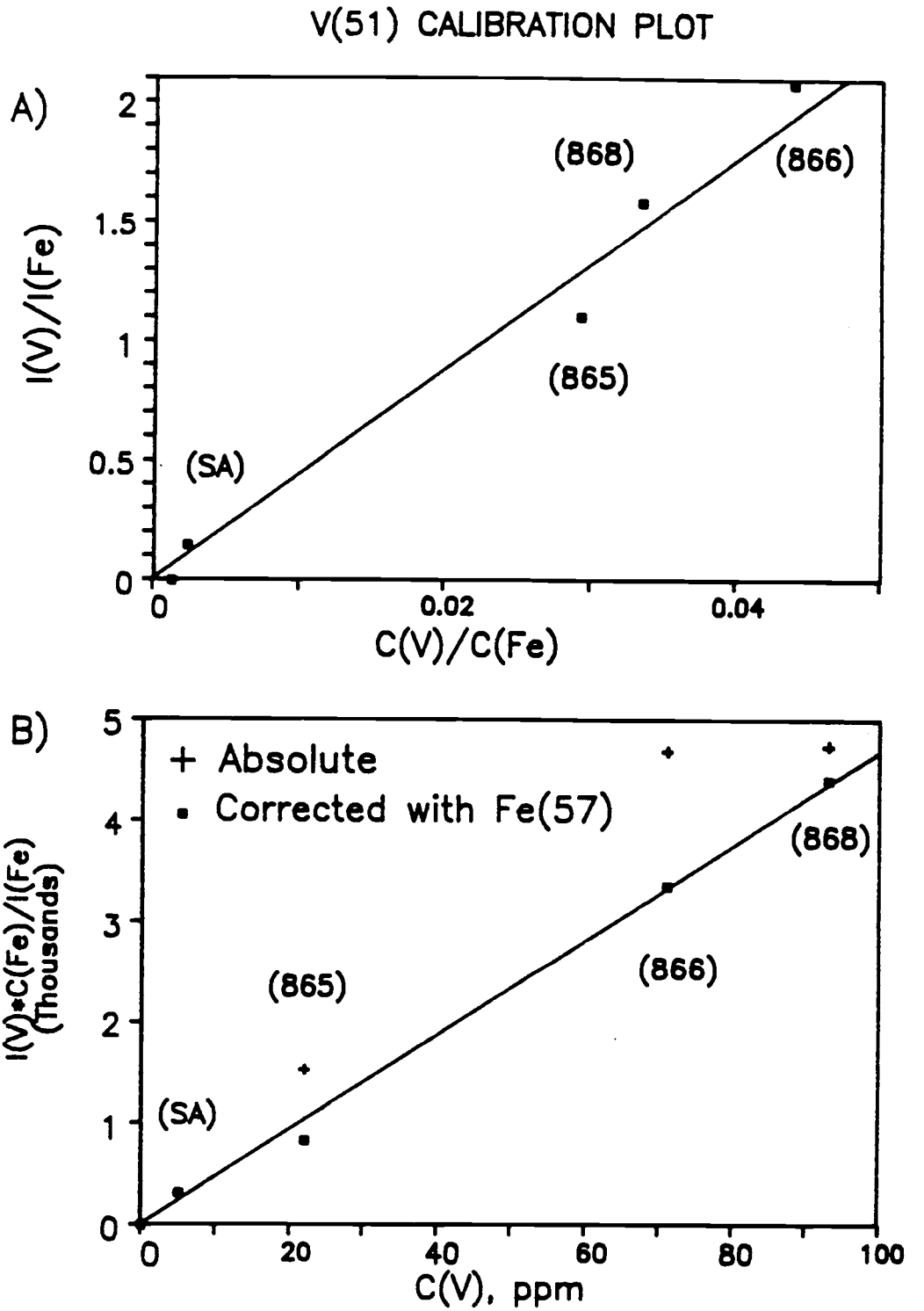

Figure VI.14 Calibration plot for ^{51}V, see Figure VI.11 for explanation. Operating conditions for the Atomsource were listed in Table VI.10.

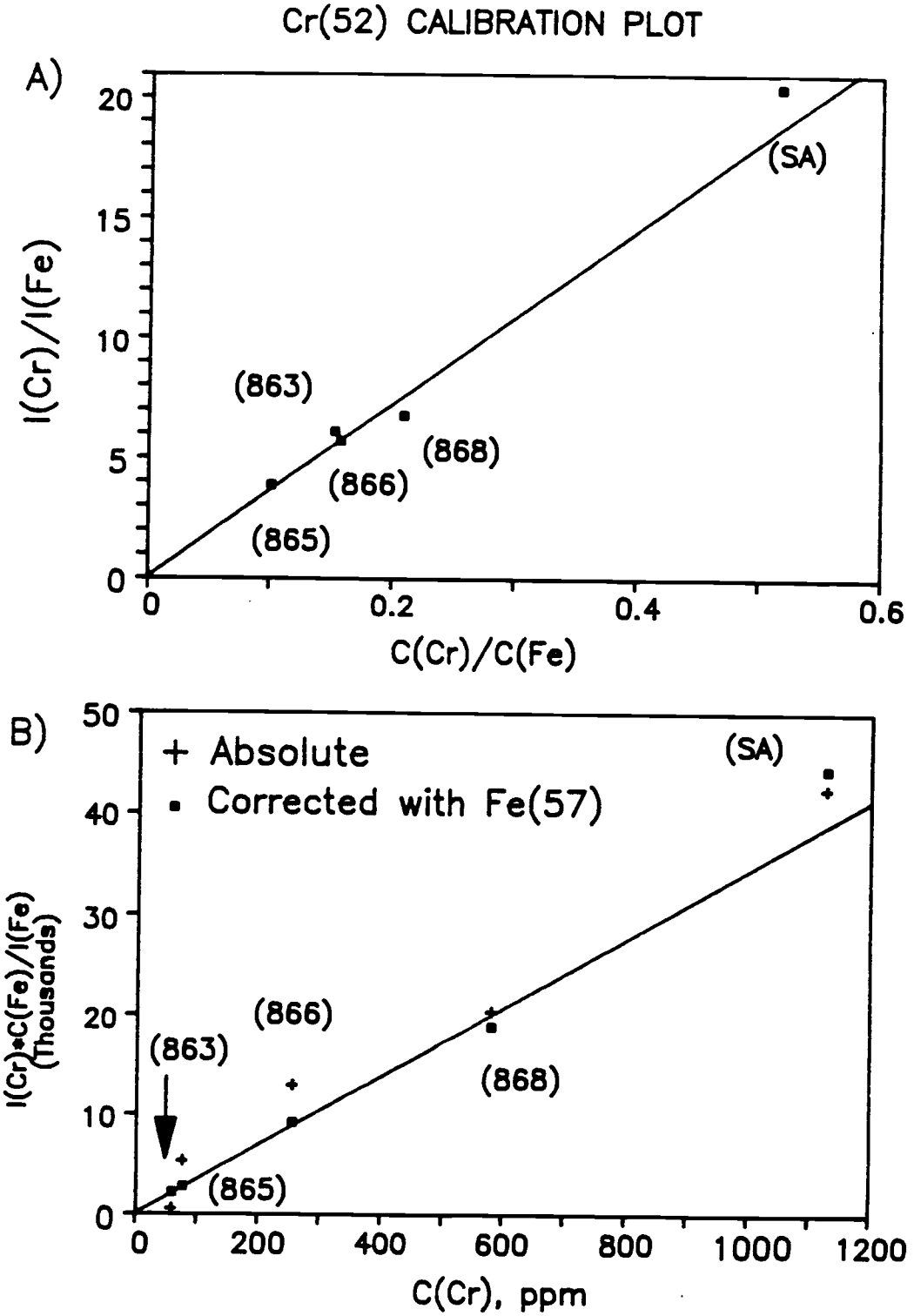

Figure VI.15 Calibration plot for ^{52}Cr, see Figure VI.11 for explanation. Operating conditions for the Atomsource were listed in Table VI.10.

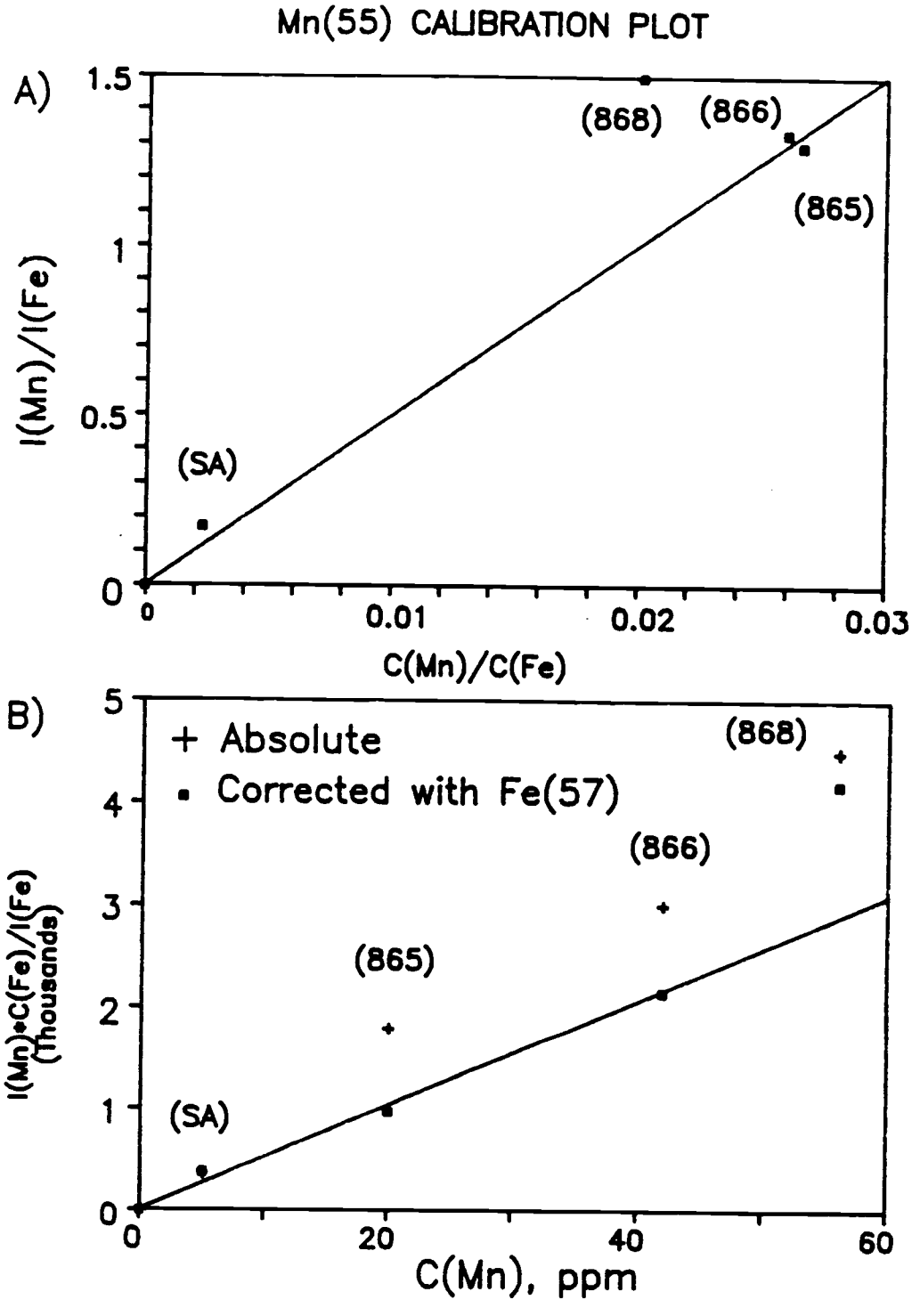

Figure VI.16 Calibration plot for ^{55}Mn, see Figure VI.11 for explanation. Operating conditions for the Atomsource were listed in Table VI.10.

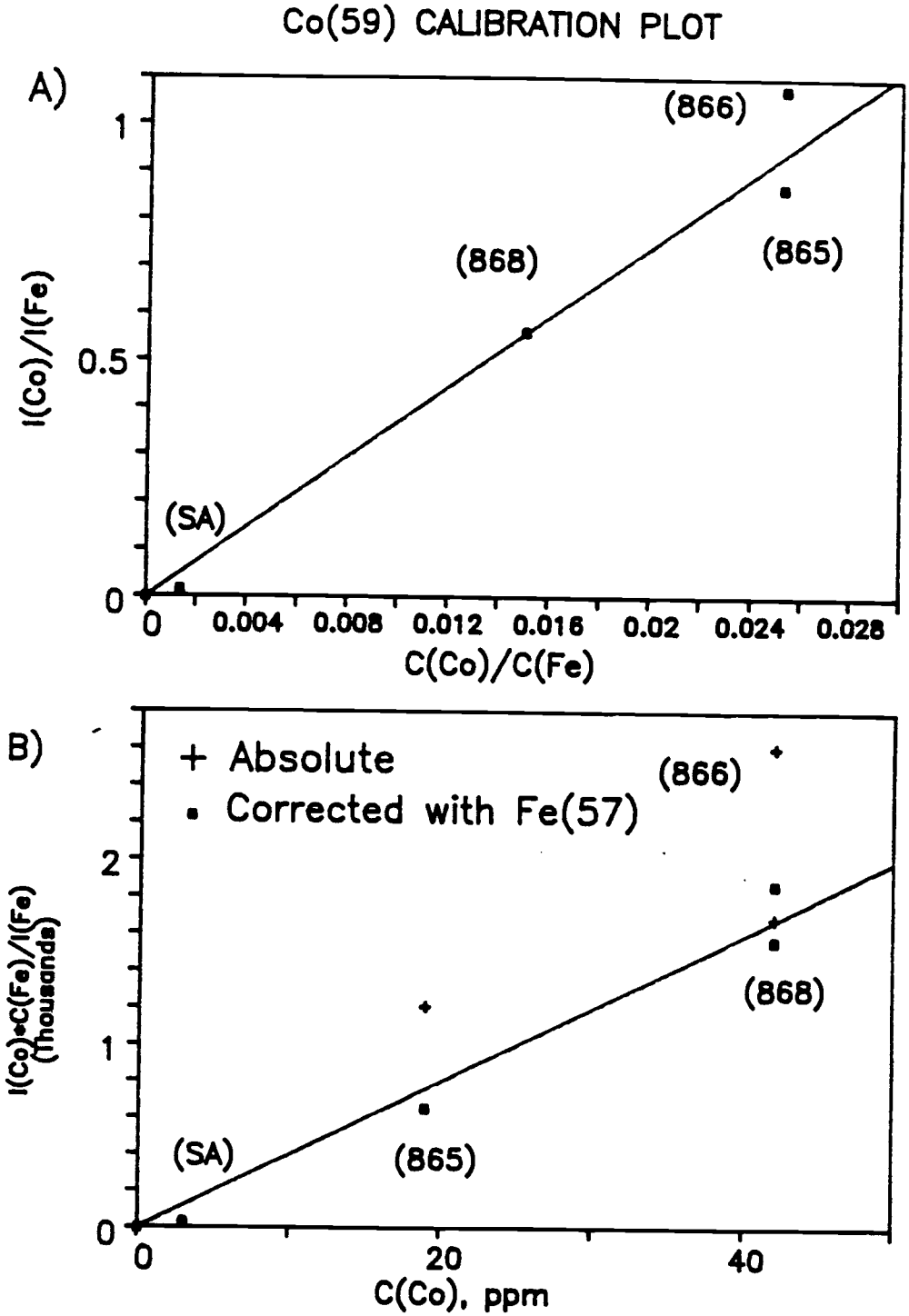

Figure VI.17 Calibration plot for ^{59}Co, see Figure VI.11 for explanation. Operating conditions for the Atomsource were listed in Table VI.10.

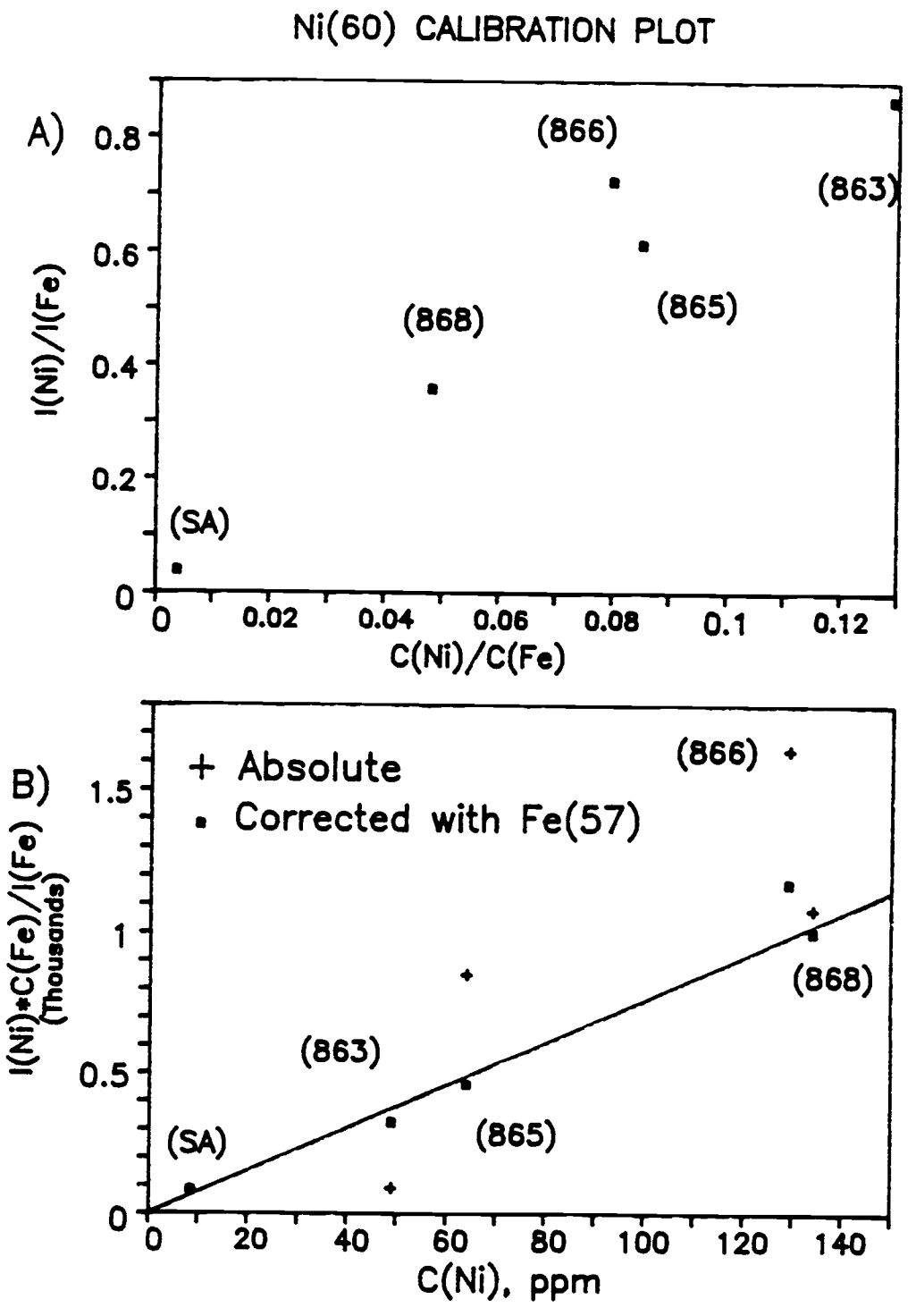

Figure VI.18 Calibration plot for ^{60}Ni, see Figure VI.11 for explanation. Operating conditions for the Atomsource were listed in Table VI.10.

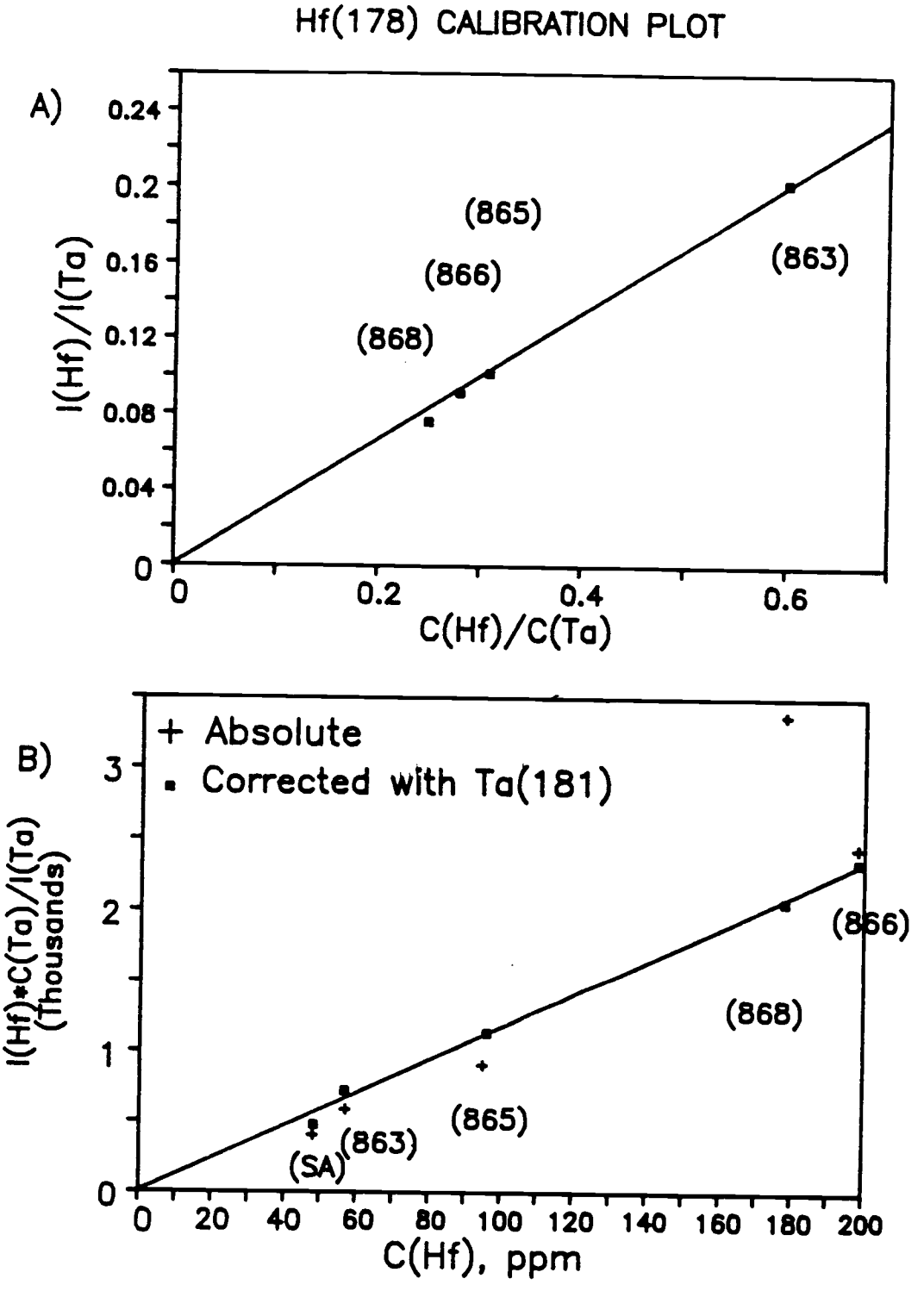

Figure VI.19 Calibration plot for ^{178}Hf, see Figure VI.11 for explanation. Operating conditions for the Atomsource were listed in Table VI.11.

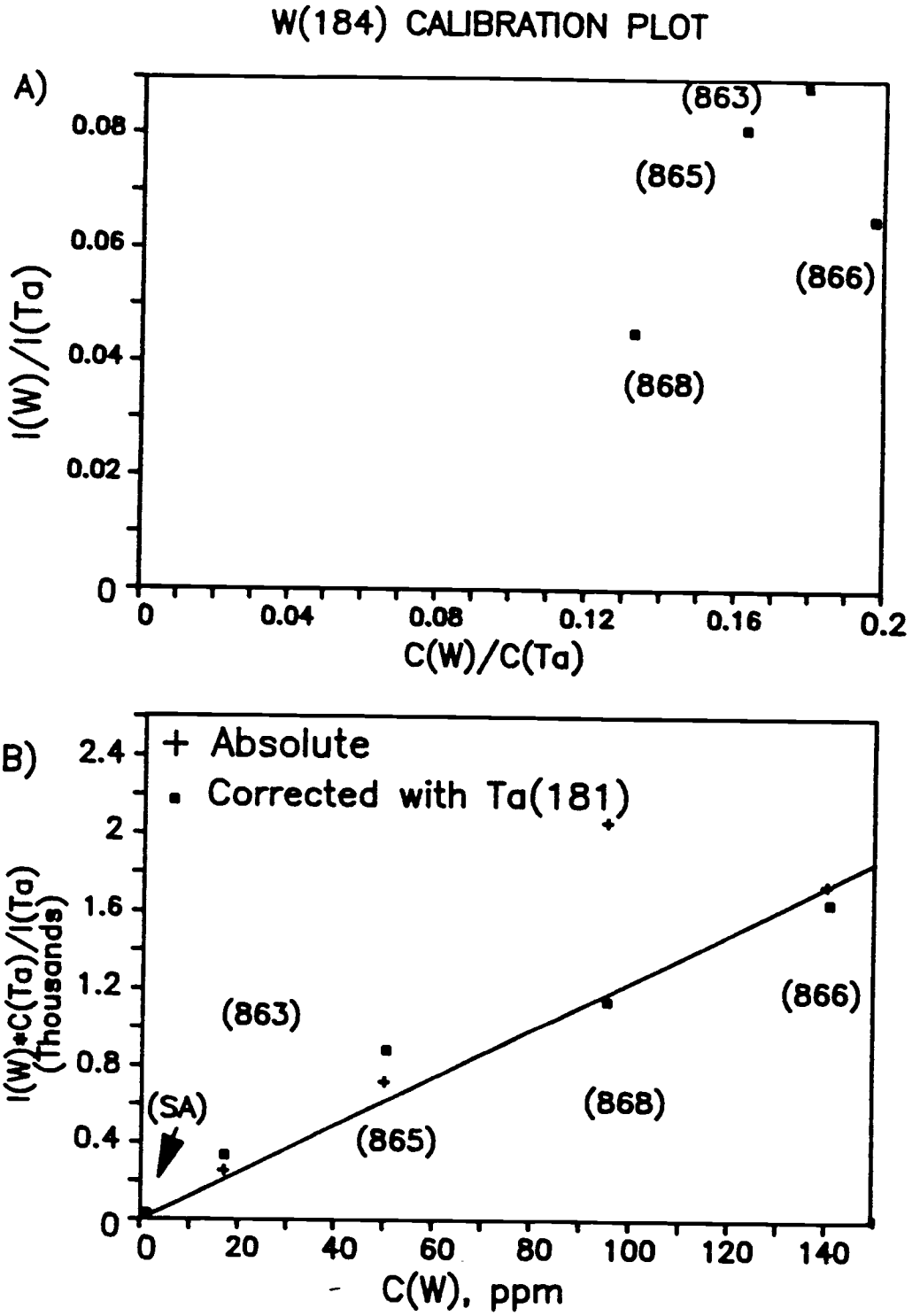

Figure VI.20 Calibration plot for ^{184}W, see Figure VI.11 for explanation. Operating conditions for the Atomsource were listed in Table VI.11.

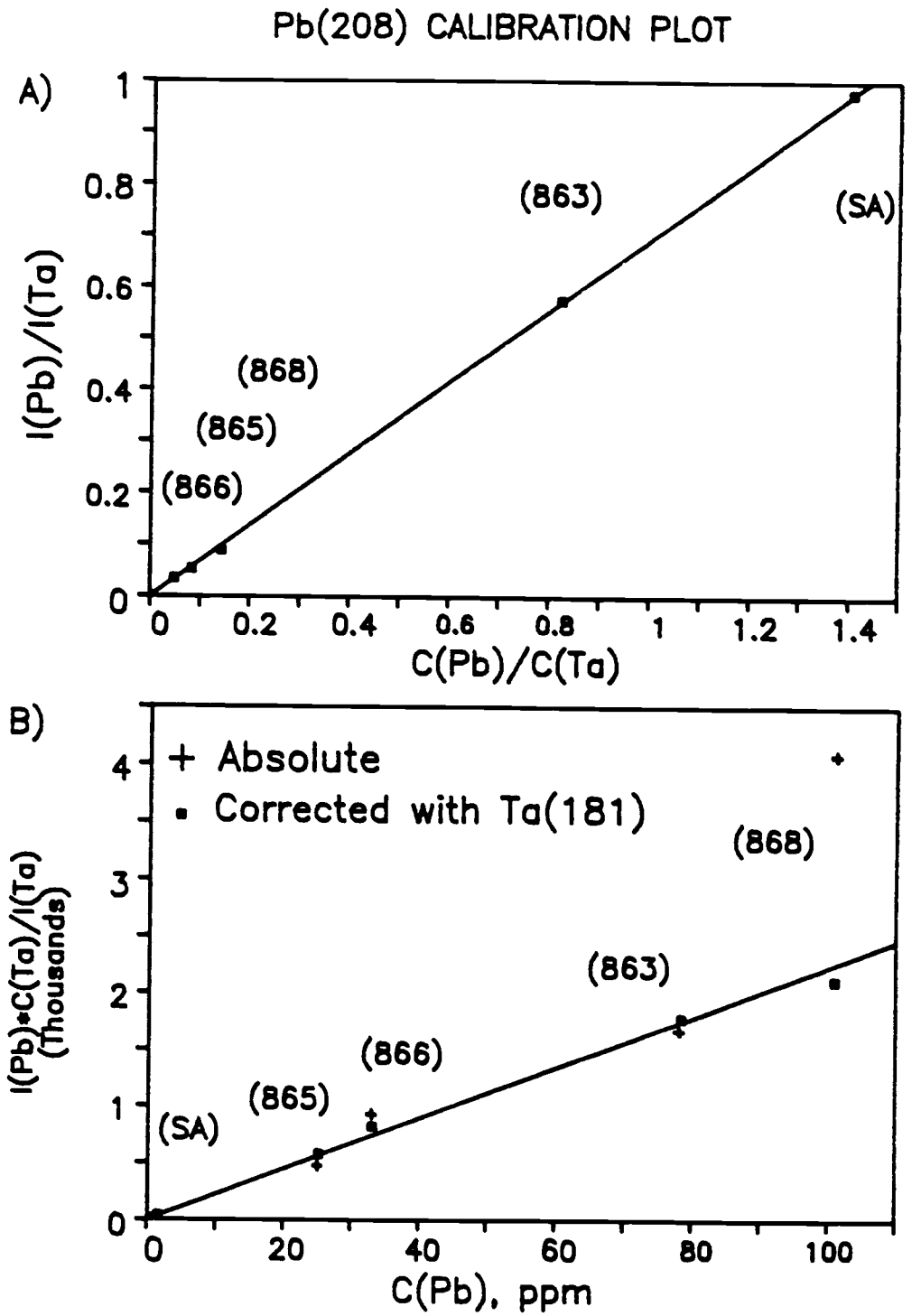

Figure VI.21 Calibration plot for ^{208}Pb, see Figure VI.11 for explanation. Operating conditions for the Atomsource were listed in Table VI.11.

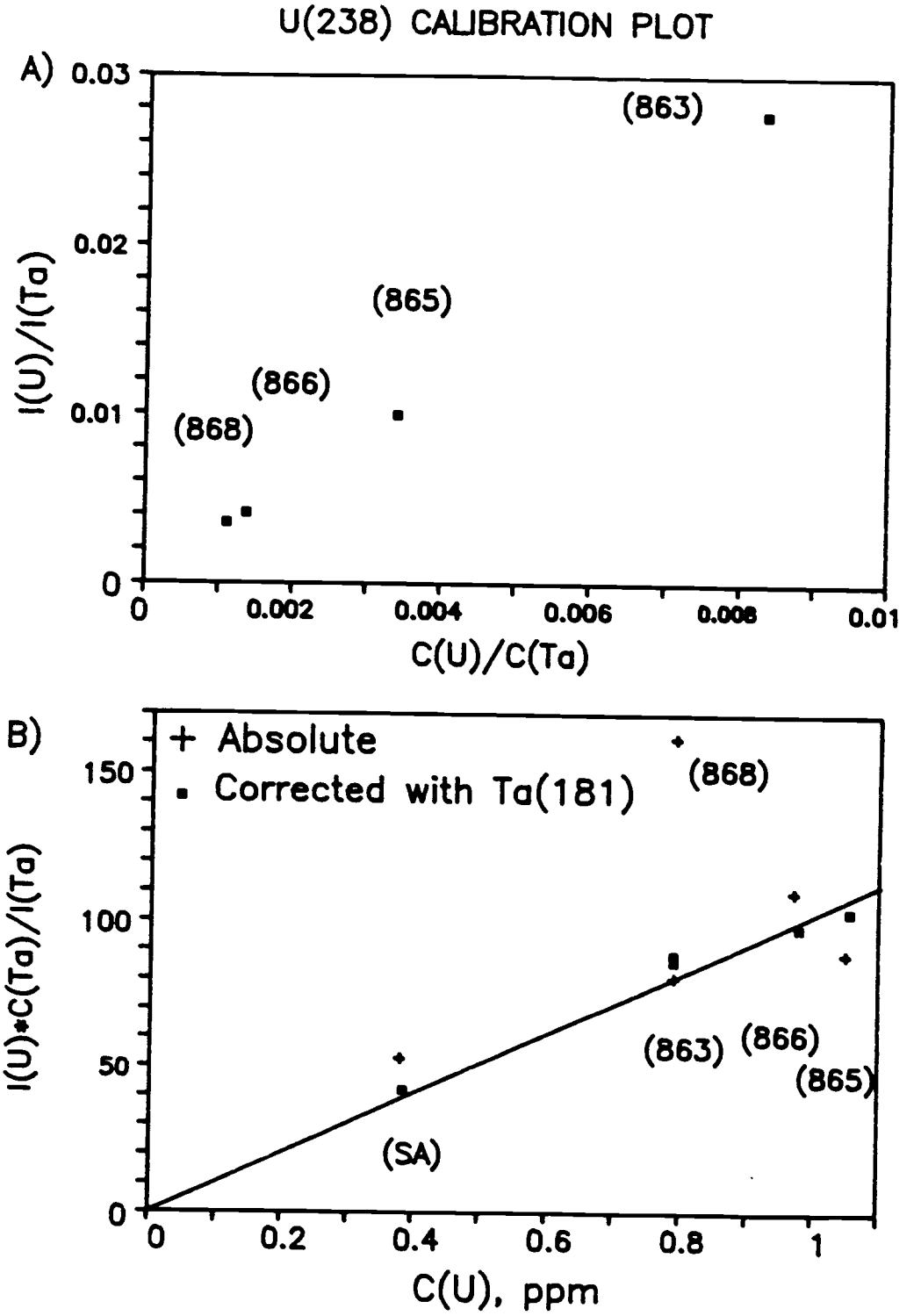

Figure VI.22 Calibration plot for ^{238}U, see Figure VI.11 for explanation. Operating conditions for the Atomsource were listed in Table VI.11.

Table VI.6 Operating conditions for the Atomsource for Figure VI.1.

Sputter time (min)	Discharge current (mA)	Discharge voltage (V)	Anode current (mA)	Anode voltage (V)	Pressure (Torr)	Gas flow rate (L/min)
3	31.1	1028	0.38	34.6	2.50	0.200
6	31.6	1027	0.44	34.3	2.48	0.200
9	32.0	1025	0.48	34.2	2.48	0.200
12	32.3	1025	0.52	34.1	2.47	0.200
15	32.9	1023	0.55	33.9	2.47	0.200
18	33.3	1022	0.58	33.8	2.47	0.200
21	31.1	971	0.56	34.7	2.42	0.200

Table VI.7 Operating conditions for the Atomsource for Figure VI.2.

Pressure (Torr)	Discharge current (mA)	Discharge voltage (V)	Anode current (mA)	Anode voltage (V)	Gas flow rate (L/min)
2.11	24.1	912	0.364	39.0	0.1680
2.18	25.0	910	0.392	38.9	0.1704
2.21	26.2	907	0.451	38.7	0.1716
2.24	24.3	912	0.309	39.3	0.1726
2.28	27.2	905	0.488	38.5	0.1740
2.32	25.3	909	0.322	39.2	0.1752
2.34	25.6	908	0.343	39.1	0.1760

Table VI.8 Operating conditions for the Atomsource for Figure VI.3.

Discharge current (mA)	Discharge voltage (V)	Anode current (mA)	Anode voltage (V)	Pressure (Torr)	Gas flow rate (L/min)
20	862	0.118	34.7	3.23	0.192
22	927	0.242	34.2	3.23	0.192
24	977	0.316	33.9	3.23	0.192
26	1032	0.382	33.7	3.23	0.192
28	1009	0.293	34.0	3.23	0.192
30	1099	0.260	34.1	3.23	0.192
32	1168	0.275	34.1	3.23	0.192
34	1222	0.367	33.7	3.23	0.192
36	1245	0.534	33.1	3.23	0.192

Table VI.9 Operating conditions for the Atomsource for Figures VI.5 to VI.9.

Figure	Discharge current (mA)	Discharge voltage (V)	Anode current (mA)	Anode voltage (V)	Pressure (Torr)	Gas flow rate (L/min)
5	32	1109	0.100	50.0	3.16	0.200
6	30	519	-	-	3.00	0.200
7	24	989	0.003	31.1	3.25	0.170
8	138	312	-	-	3.00	1.000
9	138	312	-	-	3.00	1.000
10	138	312	-	-	3.00	1.000

Table VI.10 Operating conditions for the Atomsource for low and mid mass range calibration plots.

SA #	Discharge current (mA)	Discharge voltage (V)	Anode current (mA)	Anode voltage (V)	Pressure (Torr)	Gas flow rate (L/min)
x-863	32	1067	2.850	54.7	4.40	0.196
x-865	30	1070	1.600	55.0	4.49	0.196
x-866	30	1070	1.800	55.5	4.49	0.196
x-868	31	1068	2.920	54.2	4.47	0.196
Sa	30	1071	2.460	55.1	4.32	0.196

Table VI.11 Operating conditions for the Atomsource for high mass range calibration plots.

SA #	Discharge current (mA)	Discharge voltage (V)	Anode current (mA)	Anode voltage (V)	Pressure (Torr)	Gas flow rate (L/min)
x-863	31	1169	0.130	39.3	2.87	0.193
x-865	31	1168	0.200	41.3	2.98	0.193
x-866	30	1171	0.160	41.4	3.19	0.193
x-868	31	1170	0.150	41.7	3.05	0.193
Sa	31	1169	0.100	39.5	2.66	0.193

VII. CONCLUSION

Most new analytical instruments (and the gas-jet enhanced sputtering system has been no exception) must pass through a series of steps to be widely accepted by the analytical community. First, the measurement method is "discovered" and developed by a few researchers who find it interesting. As these researchers show its promising capabilities, this technique gains wider acceptance. Next, an important step is for an instrument company to find that the method has possibilities of developing into a commercially avaible instrument. With advanced engineering, marketing strategies, and general publicity this instrument is developed and refined. However, this step does not guarantee extended success, it must show itself in the market place and in competition with the many other analytical techniques.

When a gas-jet enhanced sputtering system was discovered and first introduced by the Analyte Corporation under the trade name Atomsource, only a few research groups studied the glow discharge device for analytical applications in this country, and a few commercial glow discharges were available. However, a glow discharge device has several advantages in solids analysis that cannot be achieved with other methods. Metals, alloys, and even nonconducting sample can be rapidly analyzed to the low sub-ppb levels for elemental constituents. The advantages of this technique include wide dynamic range, low matrix effect, and relatively low price. As

a result of these positive factors, glow discharge devices have been widely studied in the analytical community. In recent years, the number of studies for glow discharge devices including a gas-jet enhanced sputtering system have increased. The gas-jet enhanced sputtering source has shown great promise for the direct analysis of solids as a rapid method.

In this research, this unique jet-enhanced sputtering method has been extensively studied to investigate its fundamental characteristics as well as applications to various analytical techniques, including atomic absorption, emission, and mass spectrometry. These studies show that the sample loss rate for a glow discharge significantly increase when gas jets impinge directly on the surface of the sample. With a single-jet glow discharge source, the gas jet increases absorbance by a factor of 40. An additional increase in absorbance by a factor of 5 is obtained with time-resolved observations when the jet flow is suddenly turned on. With a six-jet Atomsource, the sample loss rate for a Cu sample is 400 μg/min with a 0.2 L/min gas flow rate and 0.14 μg/min with no gas flow. The scanning electron micrographs show that the gas jets cause a more uniform surface than that which is formed during sputtering when no gas flows. Therefore gas-jet enhanced sputtering should decrease preferential sputtering and matrix effects and present a highly representative fraction of the sample to the spectrometer for analysis.

The Atomsource is interfaced to the mass spectrometer of a VG PlasmaQuad ICP-MS, replacing the ICP. This research shows that the Atomsource can be interchanged with the ICP on an ICP-MS to

complement its analytical capabilities, especially for the direct analysis of metal alloys. The sample is conveniently mounted on an o-ring sealed hole outside the ion source. High and low concentrations can be observed with the gas-jet enhanced ion source mass spectrometer without the necessity of dissolving the alloy. Although a quadrupole mass spectrometer does not have the mass resolution of a commercial GDMS, the relatively low cost of adding an Atomsource to an ICP-MS makes this an attractive alternative when an ICP-MS is already available in the laboratory.

Zircaloy was directly analyzed for 15 elements by an Atomsource-MS. Results, including mass discrimination studies, showed that there are fewer spectral interferences and no memory effect in the GDMS. The average relative precision of measurement for 10 elements was better than 4 %. In a multielement analysis the detection limits for 13 elements were lower than 0.5 ppm, while single-element determinations improved the detection limits by an order of magnitude. For example, the detection limit obtained for U was less than 10 ng/g for the single element determination. Concentrations determined with an internal standard were in agreement within 10 % of the certified values for most of the elements in the Zircaloy sample .

VIII. REFERENCES

(1) B. Chapman, "Glow Discharge Processes", John Wiley & Sons, New York, N. Y., 1980.

(2) J. S. Townsend, "Electricity in Gases", Oxford University Press, 1915.

(3) S. Caroli, J. of Anal. Atom. Spec., Oct. Vol. 2, 661 (1987).

(4) F. Paschen, Ann. Phys., 50, 901 (1916).

(5) H. Schüler and H. Gollnow, Z. Phys., 93, 611 (1935).

(6) W. Grimm, Z. Naturwissensch., 54, 586 (1967).

(7) A. E. Bernhard, Spectroscopy, 2, 24 (1987).

(8) O. E. Fresenius', Z Anal. Chem., 327, 111 (1987).

(9) E. Nasser, "Fundamentals of Gaseous Ionization and Plasma Electronics", Wiely, New York, (1971).

(10) D. F. Hunt, C. N. McEwen, and T. M. Harvey, Anal. Chem., 47, 1730 (1975).

(11) J. D. Cobbine, "Gaseous Conductors", Theory and Engineering Applications, Diver, New York, N. Y., 1941.

(12) G. K. Wehner, in "Methods and Phenomena: Their Applications in Science and Technology", Vol. 1, S. P. Wolsky and A. W. Czanderna, eds., Elsevier Scientific, New York, N. Y., 1975, Chapter 1.

(13) A. von Hippel, Ann. Phys., 80, 672 (1926).

(14) W. R. Grover, Phil. trans. Roy. Soc. London, 142, 87 (1852).

(15) A. E. Bernhard and H. L. Kahn, Ameri. Lab. June, 126 (1988).

(16) B. M. Gatehouse and A. Walsh, Spectrochim. Acta, 16, 602 (1960).

(17) A. J. Stirling and W. D. Westwood, J. Appl. Phys., 41, 742 (1970).

(18) B. W. Gandrud and R. K. Skogerboe, Appl. Spectrosc., 25, 243 (1971).

(19) A. J. Stirling and W. D. Westwood, J. Phys. D, 4, 246 (1971).

(20) A. Walsh, Appl. Spectrosc., 27, 335 (1973).

(21) D. S. Gough, Anal. Chem. 48, 1926 (1976).

(22) D. C. McDonald, Anal. Chem. 49, 1336 (1977).

(23) D. C. McDonald, Anal. Chem., 54, 1052 (1982).

(24) K. R. Hess and R. K. Marcus, Spectroscopy, Vol 2, 24 (1987).

(25) W. Grimm, Naturwissenschaften, 54, 586 (1967).

(26) P. W. J. M. Boumans, Anal. Chem., 44, 1219 (1972).

(27) C. J. Belle and J. D. Johnson, Appl. Spectrosc., 27, 118 (1973).

(28) H. W. Radmacher and M. C. De Swardt, Spectrochim. Acta, Part B, 30B, 353 (1975).

(29) R. A Kruger, L. R. P. Butler, C. J. Liebenberg and R. G. Bohmer, Analyst, Dec., Vol. 102, 949 (1977).

(30) N. P. Ferreira and L. R. P. Butler, Analyst, June, Vol. 103, 607 (1978).

(31) M. Fujita, J. Kashima and K. Naganuma, Anal. Chim. Acta, 124, 267 (1981).

(32) T. Yamada, J. Kashima and K. Naganuma, Anal. Chim. Acta, 124, 275 (1981).

(33) C. J. Belle and J. D. Johnson, Appl. Spectroscopy, 27, 118 (1973).

(34) M. E. WaWaitlevertch and J. K. Hurwitz, Appl. Spectroscopy, 30, 510 (1976).

(35) A. Bengtson, Spectrochim. Acta, Part B, 40B, 631 (1985).

(36) J. Pons-Corbeau, J. P. Cazet, J. P. Moreau, R. Berneron and J. C. Charbonnier, Surface and Interface Analysis, Vol. 9, 21 (1980).

(37) J. Pons-Corbeau, Surface and Interface Analysis, Vol. 4, 169 (1985).

(38) M. R. Winchester and R. K. Marcus, Applied Spectroscopy, Vol 42, 941 (1988).

(39) M. Dogan, K. Laqua and H. Massmann, Spectrochim. Acta, Part B, 26B, 631 (1971).

(40) M. Dogan, K. Laqua and H. Massmann, Spectrochim. Acta, Part B, 27B, 65 (1972).

(41) S. Caroli, A. Alimonti and K. Zimmer, Spectrochim. Acta, Part B, 38B, 625 (1983).

(42) D. C. McDonald, Spectrochim. Acta, Part B, 37B, 747 (1982).

(43) R. K. Marcus and W. W. Harrison, Spectrochim. Acta, Part B, 40B, 933 (1983).

(44) R. K. Marcus and W. W. Harrison, Anal. Chem., 59, 2369 (1987).

(45) H. Mai and H. Scholze, Spectrochim. Acta, Part B, 41B, 797 (1986).

(46) E. H. Daughtrey, W. W. Harrison, Anal. Chim. Acta, 67, 253 (1973).

(47) W. W. Harrison, N. J. Prakash, Anal. Chim. Acta, 49, 151 (1970).

(48) J. M. Brackett and T. J. Vickers, Spectrochim. Acta, Part B, 37B, 841 (1982).

(49) J. M. Brackett and T. J. Vickers, Spectrochim. Acta, Part B, 38B, 979 (1983).

(50) H. Jager and F. Blum, Spectrochim. Acta, Part B, 29B, 73 (1974).

(51) E. H. Daughtrey, Jr., D. L. Donahue, D. J. Slevin and W. W. Harrison, Anal. Chem., 47, 683 (1975).

(52) C. G. Bruhn and W. W. Harrison, Anal. Chem., 50, 16 (1978).

(53) J. S. Dobrosavljevic and M. Marinkovic, Spectrochim. Acta, 29B, 87 (1974).

(54) C. D. West and H. G. C. Human, Spectrochim. Acta, 31B, 81 (1976).

(55) N. P. Ferreira, J. A. Strauss and H. G. C. Human, Spectrochim. Acta, Part B, 35B, 287 (1980).

(56) N. M. Gagne, P. Pianarosa, G. Larin, J. P. Saint-Dizier, and P. Bouchard, Appl. Optics, 20, No. 21, 3770 (1981).

(57) D. M. Mehs and T. M. Niemczyk, Spectrochim. Acta, Part B, 36B, 965 (1981).

(58) N. P. Ferreira, J. A. Strauss and H. G. C. Human, Spectrochim. Acta, Part B, 37B, 947 (1982).

(59) N. P. Ferreira, J. A. Strauss and H. G. C. Human, Spectrochim. Acta, Part B, 38B, 899 (1983).

(60) S. L. Tong and W. W. Harrison, Anal. Chem., 56, 2028 (1984).

(61) K. R. Hess and W. W. Harrison, Anal. Chem., 60, 691 (1988).

(62) E. B. M. Steers and R. J. Fielding, J. Anal. Atom. Spectrosc. 2, 239 (1987).

(63) K. Wagatsuma and K. Hirokawa, Anal. Chem., 56, 412 (1984).

(64) K. Wagatsuma and K. Hirokawa, Anal. Chem., 56, 908 (1984).

(65) K. Wagatsuma and K. Hirokawa, Anal. Chem., 56, 2024 (1984).

(66) K. Wagatsuma and K. Hirokawa, Anal. Chem., 57, 2901 (1985).

(67) K. Wagatsuma and K. Hirokawa, Anal. Chem., 58, 1112 (1986).

(68) K. Wagatsuma and K. Hirokawa, Spectrochim. Acta, Part B, 42B, 523 (1987).

(69) K. Wagatsuma and K. Hirokawa, Anal. Chem., 60, 702 (1988).

(70) N. P. Ferreira and H. G. C. Human, Spectrochim. Acta, Part B, 25B, 647 (1970).

(71) B. L. Bentz and W. W. Harrison, Anal. Chem., 51, 1853 (1979).

(72) P. E. Walters and H. G. C. Human, Spectrochim. Acta, Part B, 36B, 585, (1981).

(73) R. A. Kruger, R. M. Bombelka and K. Laqua, Spectrochim. Acta, Part B, 35B, 581 (1980).

(74) R. A. Kruger, R. M. Bombelka and K. Laqua, Spectrochim. Acta, Part B, 35B, 589 (1980).

(75) D. C. McDonald, Spectrochim. Acta, 37 B, 747 (1982).

(76) P. B. Farnsworth and J. P. Walters, Spectrochim. Acta, 37B, 773 (1982).

(77) J. B. Ko, Spectrochim. Acta, Part B, 39B, 1405 (1984).

(78) J. A. Strauss, N. P. Ferreira and H. G. C. Human, Spectrochim. Acta, Part B, 37B, 947 (1982).

(79) F. W. Aston, "Mass Spectra and Isotopes", Edward Arnold & Co., London, England, 1933.

(80) F. A. White, "Mass Spectrometry in Science and Technology", Wiley, New York, 1968.

(81) F. W. Aston, "Mass Spectra and Isotopes", 2nd Ed., Longmans, Green, and Co., New York, 1942.

(82) J. A. McHugh, in "Methods for Surface Analysis", Elsevier, Amsterdam, 1975.

(83) F. Paschen, Ann. Phys., 50, 901 (1916).

(84) H. Schuler, Z. Phys., 72, 423 (1931).

(85) A. Walsh, Spectrochim. Acta, 7, 108 (1955).

(86) G. D. Christian and F. J. Felhman, "Atomic Absorption Spectroscopy", Wiley, New York, 1970.

(87) W. Grimm, Spectrochim. Acta, B23, 443 (1968).

(88) P. W. J. M. Boumans, Anal. Chem., 44, 1219 (1972).

(89) M. Dogan, K. Lacqua, and H. Massonan, Spectrochim. Acta, B26, 631 (1971).

(90) J. W. Coburn, Rev. Sci. Instrum., 41, 1219 (1970).

(91) H. Oechsner and W. Gerhard, Phys. Lett., 40A, 211 (1972).

(92) H. Oechsner and W. Gerhard, Surf. Sci., 44, 480 (1974).

(93) W. W. Harrison, C. W. Magee, Anal. Chem., 46, 461 (1974).

(94) Colby, B. N.; Evans, C. A. Anal. Chem., 46, 1236 (1974).

(95) Daughtrey, E. H. Jr.; Harrison, W. W. Anal. Chem., 47, 1024 (1975).

(96) Wallace, J. R. ; Natusch, D. F. S. ; Colby, B. W. ; Evans, C. A. Jr. Anal. Chem. 48, 118 (1976).

(97) C. W. Magee, D. L. Donahue, and W. W. Harrison, Anal. Chem., 44, 2413 (1972).

(98) C. W. Magee and W. W. Harrison, Anal. Chem., 45, 220 (1973).

(99) E. H. Daughtrey, D. L. Donohue, D. J. Slevin, and W. W. Harrison, Anal. Chem. 47,683 (1975).

(100) Mattson, W. A.; Bentz, B. L. ; Harrison, W. W. Anal. Chem. 48, 489 (1976).

(101) W. W. Harrison and B. L. Bentz, Anal. Chem. (1979), 51 (1853).

(102) J. W. Coburn, and W. W. Harrison, Appl. Spec. Rev, 17, 95 (1981).

(103) D. L. Hall and P. K. Robinson, American Lab., Aug., 74 (1987).

(104) P. J. Savickas, K. R. Hess, R. K. Marcus, W. W. Harrison, Anal. Chem., 56, 819 (1984).

(105) N. Jakubowski, D. Stuewer, and W. Vieth, Int. J. Mass Spectrom. Ion Processes, 71, 183 (1986).

(106) N. Jakubowski, D. Stuewer, and W. Vieth, Anal. Chem., 59, 1825 (1987).

(107) B. L. Bentz and W. W. Harrison, Prog. Analyst. Spectrosc., Vol. 11, 53 (1988)

(108) G. J. Beenen, Ph.D. Thesis, Oregon State University, Corvallis, OR 97331 (1981).

(109) J. W. Hosch, Present Address: Texas Instruments, Inc., P.O. Box 5012, Dallas, TX 75222.

(110) A. L. Lewis, Ph.D. Thesis, Oregon State University, Corvallis, OR 97331 (1976).

(111) Handbook of Chemistry and Physics, Vol. 55, the Chemical Rubber Co., Cleveland, OH, 1974.

(112) B. J. Russell, A. Walsh Spectrochim. Acta, 15, 883-885 (1959).

(113) B. M. Gatehouse, A. Walsh, Spectrochim. Acta, 16, 602-604 (1960).

(114) J. A. Goleb, J. K. Brody, Anal. Chim. Acta, 28, 457 (1963).

(115) A. J. Stirling, W. D. Westwood, J. Appl. Phys., 41, 742-748, (1970).

(116) Stirling A. J.; Westwood W. D. J. Phys. D 1971, 4, 246-252.

(117) Gandrud B. W.; Skogerboe R. K. Appl. Spectrosc. 1971, 25, 243-246.

(118) Walsh A. Appl. Spectrosc. 1973, 27, 335-341.

(119) Gough D. S. Anal. Chem. 1976, 48, 1926-1931.

(120) McDonald D. C. Anal. Chem. 1977, 49, 1336-1343.

(121) Ferreira N. P.; Human H. G. C. Spectrochim. Acta, Part B 1981 36B, 215-229.

(122) McDonald D. C. Anal. Chem. 1982, 54, 1052-1056.

(123) Grimm W. Naturwissenschaften 1967, 54, 586.

(124) Grimm W. Spectrochim. Acta, Part B 1968, 23B, 443-454.

(125) Dogan M.; Laqua K.; Massmann H. Spectrochim. Acta, Part B 1971 26B, 631-649.

(126) Dogan M.; Laqua K.; Massmann H. Spectrochim. Acta, Part B 1972 27B, 65-88.

(127) Boumans P. W. J. M. Anal. Chem. 1972, 44, 1219-1228.

(128) Belle C. J.; Johnson J. D. Appl. Spectrosc. 1973, 27, 118-124.

(129) Radmacher H. W.; De Swardt M. C. Spectrochim. Acta, Part B 1975 30B, 353-360.

(130) Lowe R. M. Spectrochim. Acta, Part B 1976, 31B, 257-263.

(131) Waitlevertch M. E.; Hurwitz J. K. Appl. Spectrosc. 1976, 30, 510-515.

(132) Kruger R. A.; Butler L. R. P.; Liebenberg C. J.; Bohmer R. G. Analyst 1977, 102, 949-954.

(133) Ferreira N. P.; Butler L. P. R. Analyst, 1978, 103, 607-612.

(134) Fujita M.; Kashima J.; Naganuma K. Anal. Chim. Acta 1981, 124, 267-274.

(135) Yamada T.; Kashima J.; Naganuma K. Anal. Chim. Acta 1981, 124, 275-280

(136) Brackett J. M.; Vickers T. J. Spectrochim. Acta, Part B 1982 37B, 841.

(137) Ferreira N. P.; Strauss J. A.; Human H. G. C. Spectrochim. Acta, Part B 1983, 38B, 899-911.

(138) Brackett J. M.; Vickers T. J. Spectrochim. Acta, Part B 1983, 38B, 979.

(139) Lomdahl G. S.; Sullivan J. V. Spectrochim. Acta, Part B 1984 39B, 1395-1403.

(140) Ko J. B. Spectrochim. Acta, Part B 1984, 39B, 1405-1423.

(141) Bengtson A. Spectrochim. Acta, Part B 1985, 40B, 631-639.

(142) Gough D. S.; Hannaford P.; Walsh A. Spectrochim. Acta, Part B 1973, 28B, 197-210.

(143) Gough D. S.; Meldrum J. R. Anal. Chem. 1980, 52, 642-646.

(144) Dijk V. C.; Smith B. W.; Winefordner J. D. Spectrochim. Acta, Part B 1982, 37B, 759-768.

(145) Bubert H. Spectrochim. Acta, Part B 1984, 39B, 1377-1387.

(146) Patel B. M.; Winefordner J. D. Appl. Spectrosc. 1986, 40, 667-672.

(147) Patel B. M.; Winefordner J. D. Spectrochim. Acta, Part B 1986, 41B, 469-474.

(148) Bentz B. L.; Harrison W. W. Anal. Chem. 1979, 51, 1853-1855.

(149) Loving T. J.; Harrison W. W. Anal. Chem. 1983, 55, 1523-1526.

(150) Loving T. J.; Harrison W. W. Anal. Chem. 1983, 55, 1526-1530.

(151) Savickas P. J.; Hess K. R.; Marcus R. K.; Harrison W. W. Anal. Chem. 1984, 56, 817-819.

(152) Hess K. R.; Marcus R. K.; King F. L.; Harrison W. W. Anal. Chem. 1986, 58, 341A-356A.

(153) Jakubowski N.; Stuewer D.; Vieth W. Anal. Chem. 1987, 59, 1825.

(154) Ferreira N. P.; Strauss J. A.; Human H. G. C. Spectrochim. Acta, Part B 1982, 37B, 272-279.

(155) Strauss J. A.; Ferreira N. P.; Human H. G. C. Spectrochim. Acta, Part B 1982, 37B, 947-954.

(156) Wagatsuma K.; Hirokawa K. Anal. Chem. 1984, 56, 412-416.

(157) Wagatsuma K.; Hirokawa K. Anal. Chem. 1984, 56, 908-913.

(158) Wagatsuma K.; Hirokawa K. Anal. Chem. 1984, 56, 2024-2028.

(159) Wagatsuma K.; Hirokawa K. Anal. Chem. 1985, 57, 2901-2907.

(160) Wagatsuma K.; Hirokawa K. Anal. Chem. 1986, 58, 1112-1115.

(161) Wagatsuma K.; Hirokawa K. Spectrochim. Acta, Part B 1987, 42B, 523-531.

(162) Steers E. B. M.; Fielding R. J. J. Anal. Atom. Spectrosc. 1987, 2, 239-244.

(163) Kruger R. A.; Bombelka R. M.; Laqua K. Spectrochim. Acta, Part B, 1980, 35B, 581.

(164) Larkins P. L. Anal. Chim. Acta 1981, 132, 119.

(165) Mehs D. M.; Niemczyk T. M. Spectrochim. Acta, Part B 1981, 36B, 965-971.

(166) Tong S. L; Harrison W. W. Anal. Chem. 1984, 56, 2028.

(167) Mai H.; Scholze H. Spectrochim. Acta, Part B 1986, 41B, 797.

(168) Jager H.; Blum F. Spectrochim. Acta, Part B 1974, 29B, 73-77.

(169) Daughtrey E. H., Jr.; Donohue D. L.; Slevin D. J.; Harrison W. W. Anal. Chem. 1975, 47, 683-688.

(170) Bruhn C. G.; Harrison W. W. Anal. Chem. 1978, 50, 16-21.

(171) Bernhard A. E. Spectroscopy 1987, 2, 24-27.

(172) Hippel A. V. Ann. Phys. 1926, 81, 1043.

(173) Gunterschulze A.; Tollmien W. Z. Phys. 1942, 119, 685.

(174) Magnuson G. D.; Meckel B. B.; Harkins P. A. J. Appl. Phys. 1961, 32, 369.

(175) Kaminsky M. Atomic and Ionic Impact Phenomena on Metal Surfaces, Academic Press, New york, N. Y., 1965.

(176) Carter G.; Colligon J. S. Ion Bombardment of Solids, American Elsevier, New York, N. Y., 1968.

(177) Witcomb M. J. J. Mater. Sci. 1974, 9, 551.

(178) Navinsek B. Prog. Surf. Sci. 1976, 7, 49.

(179) Aston, F. W. Mass spectra and Isotopes, Edward Arnold & Co., London, England, 1933.

(180) Bainbridge, K. T., Phys. Rev., 1932, 39, 847.

(181) Beske, H. E., Hurrle, A. and Jochum, K. P. Z. Anal. Chem., 1981, 309, 257.

(182) Bacon, J. R. and Ure, A. M. Analyst, 1984, 109, 1229.

(183) McHugh, J. A. In Methods for Surface Analysis (Wolsky, S. P. and Czanderna, A. W., eds.). Elsevier, Amsterdam, 1975.

(184) Coburn, J. W. Rev. Sci. Instrum., 1970, 41, 1219.

(185) Oechsner, H. and Gerhard, W. Phys. Lett., 1972, 40A, 211.

(186) Bentz, B. L., Bruhn, C. G., Harrison, W. W. Int. J. Mass Spectrom. Ion Phys. 1976 28, 409.

(187) Mattson, W. A., Bentz, B. L., and Harrison, W. W. Anal. Chem., 1976, 48, 489.

(188) Harrison, W. W., Hess, K. R., Marcus, R. K., and King, F. L. Anal. Chem., 1986, 58, 341A.

(189) Bruhn, C. G., Bentz, B. L., and Harrison, W. W. Anal. Chem., 1979, 51, 673.

(190) Cantle, J. E., Hall, E. F., Shaw, C. J., and Turner, P. J. Int. J. Mass Spectrom. Ion Phys., 1983, 46, 11.

(191) Robinson, P. K., and Hall, E. F. American Lab., 1987, August, 74-85.

(192) Colby, B. N., and Evans, C. A. Jr. Anal. Chem., 1974, 46, 1236.

(193) Loving, T. J., and Harrison, W. W. Anal. Chem., 1983, 55, 1526.

(194) Harrison, W. W., and Bentz, B, L. Anal. Chem., 1979, 51, 1853.

(195) Jakubowski, N., Stuewer, D., Toelg, G. Int. J. Mass Spectrom. Ion Proc. 1986, 71, 183.

(196) Jakubowski, N., Stuewer, D., Toelg, G. Anal. Chem., 1987, 59, 1825-1830.

(197) Kim, H. J., and Piepmeier, E. H. Anal. Chem., 1988, 60, 2040-2046.

(198) Bernhard, A. E., Spectroscopy (Eugene, Oreg.), 1987, 2, 24-27.

(199) Beck, G. L., and Farmer, III, O. T., J. Anal. Atom. Spectrom., 1988, 3, 771-773.

(200) Longerich, H. P., Fryer, B. T., Strong D. F., and Kantipuly, C. J. Spectrochim. Acta, 1987, Vol. 42B, 75-92.

(201) Gregoire, D. C. Spectrochim. Acta, Part B, 1987, 42B, 895.

(202) Gray, A. L., Date, A. R. Analyst 1983, 108, 103.

(203) Bentz, B. L. and Harrison, W. W. Prog. analyst. Spectrosc., 1988, Vol.11, 53-113.

(204) Robinson, K., and Hall, F. H. J. of Metals, 1987, April, 14-16.

(205) Kim, H. J. and Piepmeier, E. H. Anal. Chem., 1988, 60, 2040-2046.

(206) Kim, H. J. and Piepmeier, E. H. Anal. Chem., submitted for publication.

(207) Jakubowski, N.; Stuewer, D.; Toelg, G. Int. J. Mass Spectrom. Ion Proc. 1986, 71, 183.

(208) Houk, R. S. Anal. Chem. 1986, 58, 197A.

(209) Boomer, D. W. and Powell, M. J. Anal. Chem 1987, 59, 2810-2813.

(210) Gray, A. L. "Inorganic mass spectrometry" John Wiley & Sons, New York, 1988, pp. 257-299.

(211) Tan S. H. and Horlick G. Applied Spectrosc. 1986, 40, 445-460.

(212) NBS Handbook 91, 1963, 4-9.

(213) Date, A. R. and Gray, A. L. Spectrochim. Acta, 1983, 38B, 29-37.

(214) Gray, A. L. Spectrochim. Acta, 1985, 40B, 1525-1537.

(215) Date, A. R. and Gray, A. L. Int. J. Mass Spectrom. Ion Phys. 1983, 48, 357.

(216) Smith, R. G., Brooker, E. J., Douglas, D. J., Quan, E. S. K. and Rosenblatt, G. J. Geochem. Expl., 1984, 21, 385.

(217) Strong, D. F. and Longerich, H. P. Geosci. Can. 1985, 12, 72.

(218) Gray, A. L., Spectrochim. Acta, 1986, Vol 41B, 151-167.

(219) Longerich, H. P., Fryer, B. J. and Strong, D. F. Spectrochim. Acta, 1987, 42B, 101-109.